

2017

# Thermal and Catalytic Cracking of Athabasca VR and Bitumen

Eshraghian, Afrooz

---

Eshraghian, A. (2017). Thermal and Catalytic Cracking of Athabasca VR and Bitumen (Master's thesis, University of Calgary, Calgary, Canada). Retrieved from <https://prism.ucalgary.ca>. doi:10.11575/PRISM/28305  
<http://hdl.handle.net/11023/3786>

*Downloaded from PRISM Repository, University of Calgary*

UNIVERSITY OF CALGARY

Thermal and Catalytic Cracking of Athabasca VR and Bitumen

by

Afrooz Eshraghian

A THESIS

SUBMITTED TO THE FACULTY OF GRADUATE STUDIES  
IN PARTIAL FULFILMENT OF THE REQUIREMENTS FOR THE  
DEGREE OF MASTER OF SCIENCE

GRADUATE PROGRAM IN CHEMICAL AND PETROLEUM ENGINEERING

CALGARY, ALBERTA

APRIL, 2017

© Afrooz Eshraghian 2017

## Abstract

There is a keen interest in upgrading heavy oil in order to meet current and future demand for liquid hydrocarbon fuels coupled with a need to enhance transportability of heavy crudes. In this study, thermal cracking of Athabasca vacuum residue (AVR) was conducted at different operating conditions such as residence time, pressure of the reactor unit, stirring rate, and temperature and different asphaltenes content in presence and absence of alumina nanoparticles (NP) and drill cuttings (DC). A closed reactor system, an autoclave, was employed. Despite the abundance of literature on thermal cracking of heavy crude, very few reports have in fact employed a closed system arrangement. Alumina NP was formulated *in situ* by thermal decomposition of dispersed aqueous solution of the aluminium nitrate in the heavy oil medium. Its performance was compared with its *commercial* counterpart. Drill cuttings, a by-product of drilling fluid reconditioning, was also evaluated as a thermal cracking catalyst. The yield of the different fractions, the total energy consumption, the pressure buildup in the reactor, and the °API gravity and viscosity of the liquid product were used to evaluate the impact of each parameter. Thermogravimetry analysis (TG/DTA) of the produced asphaltenes and toluene insolubles (TI), high-temperature simulated distillation (HTSD) analysis of the liquid product and gas chromatography (GC) of gaseous product were performed to characterize the different fractions. Results show that the effect of given parameter depends on the asphaltenes content of the feedstock. Removing asphaltenes from the feedstock shifted the reactions to produce more overall asphaltenes. The high surface area provided by dispersed NP and high content of DC in the heavy oil, increased the TI yield, while improved the viscosity of the maltene product. On the other hand, the mechanism of coke inhibition in presence of a specific concentration of DC could be elucidated from scanning electron microscopy (SEM) photographs analysis of the toluene insoluble (TI) fraction.

## **Acknowledgements**

I would like to express my deepest gratitude to my supervisor, Dr. Maen Husein, who gave me the opportunity to be a member of his team. I am grateful for his continuous encouragement and support throughout the different aspect of this research with his expertise and patience. I would like to thank my committee members, Dr. Harvey Yarranton and Dr. Kunal Karan.

I would like to express my profound gratitude to family members. Special thanks go to my father, Kiamars, and my mother, Shahrbanoo, for their love and unfailing support for whatever I pursue. I am also thankful for my supportive brother, Arash, and his lovely family, and my dearest sister Atoosa and her wonderful family, and my lovely sister, Armaghan, who were always there for me with love and support.

Thanks also to Ms. Tong Xu and Mr. Thomas Kaminski for helping in running part of the experiments and Dr. Mohsen Zirrahi for helping in gas chromatography analysis.

My thanks are extended to my colleagues and friends in the NTEE (Nano Technology for Energy and Environment) research group.

The financial support was obtained from Natural Sciences and Engineering Research Council of Canada (NSERC). In addition, the drilling cuttings used in this study, were donated by Executive Mat Service (Calgary, AB).

Finally, I would like to show my warmest gratitude to all those who helped me in the completion of this research.

## **Dedication**

To my family

## Table of Contents

Abstract.....	ii
Acknowledgements.....	iii
Dedication.....	iv
Table of Contents.....	v
List of Tables.....	vii
List of Figures and Illustrations.....	viii
List of Symbols, Abbreviations and Nomenclature.....	xiii
CHAPTER ONE: INTRODUCTION.....	14
1.1 Motivation.....	14
1.2 Objectives.....	17
1.3 Outline of the thesis.....	17
CHAPTER TWO: LITERATURE REVIEW.....	19
2.1.1 Unconventional oil.....	19
2.1.2 Asphaltenes.....	20
2.1.3 The upgrading process.....	21
2.1.4 Non-catalytic thermal cracking.....	22
2.1.5 The chemistry of thermal cracking.....	23
2.1.6 Catalytic cracking.....	24
2.1.7 In situ prepared nanoparticles.....	25
2.1.8 Role of fine solid in cracking.....	26
CHAPTER THREE: THERMAL CRACKING OF ATHABASCA VR AND BITUMEN AND THEIR MALTENE FRACTION IN A CLOSED REACTOR SYSTEM*.....	27
3.1 Abstract.....	27
3.2 Introduction.....	28
3.3 Experimental procedures.....	31
3.3.1 Materials.....	31
3.3.2 Feedstock preparation.....	32
3.3.3 Thermal cracking.....	33
3.4 Results and discussion.....	37
3.4.1 Effect of reaction time.....	37
3.4.2 Effect of pressure.....	42
3.4.3 Effect of stirring.....	44
3.4.4 Effect of temperature.....	46
3.4.5 Effect of asphaltenes content.....	47
3.4.6 SimDist and GC test results.....	53
3.4.7 DSC/DTG test results.....	55
3.5 Conclusions.....	57
3.6 Acknowledgment.....	58
3.7 Supporting material.....	59
3.7.1 Supporting material A: Estimating heat losses from the reactor unit.....	59
3.7.1.1 Introduction.....	60
3.7.1.2 Heat loss estimation.....	62

3.7.2 Supporting material B.....	69
CHAPTER FOUR: CATALYTIC THERMAL CRACKING OF ATHABASCA VR IN A CLOSED REACTOR SYSTEM.....	73
4.1 Abstract.....	73
4.2 Introduction.....	74
4.3 Experimental procedure.....	79
4.3.1 Materials.....	79
4.3.2 Thermal cracking.....	79
4.3.3 Characterization.....	81
4.4 Results and discussions.....	83
4.4.1 Catalyst Characterization.....	84
4.4.1.1 Alumina characterization.....	84
4.4.1.2 DC characterization.....	90
4.4.1.3 TI characterization from control sample.....	92
4.4.2 Effect of Al <sub>2</sub> O <sub>3</sub> NPs on the yield and product quality.....	95
4.4.3 Effect of Drill Cuttings (DC) on the yield and product quality.....	99
4.4.4 H/C and STA analysis of TI and asphaltenes.....	107
4.4.5 HTSD and GC Test Result.....	110
4.5 Conclusions.....	112
4.6 Acknowledgment.....	113
4.7 Supporting material.....	114
4.7.1 Scherrer's equation.....	114
4.7.2 Catalyst Characterization.....	114
4.7.3 Sample calculations for pressure build up from Al(NO <sub>3</sub> ) <sub>3</sub> decomposition ...	119
4.7.4 Energy consumption and pressure build up.....	120
4.7.5 Reaction rate constant calculations.....	122
CHAPTER FIVE: CONCLUSIONS AND RECOMMENDATIONS.....	126
5.1 Conclusions.....	126
5.2 Original contributions to knowledge.....	127
5.3 Recommendations for future works.....	128
REFERENCES.....	129
APPENDIX.....	143

## List of Tables

<b>Table 2. 1:</b> Definition and classification of petroleum material (Gray 2015).....	19
<b>Table 3.1:</b> Properties of the different feedstocks employed in this work. ....	31
<b>Table 3.2:</b> The total energy input to the reactor and the final pressure after cooling for the thermal cracking of Athabasca VR (AVR) and its maltene extract (AVRM) at 400°C. ....	38
<b>Table 3.3:</b> Analysis of gaseous products collected at 400°C for the thermal cracking of AVR at 400°C and 0 rpm for 1 h.....	55
<b>Table s3.1:</b> Summary of heat loss based on estimates from <i>zone I</i> and natural convection. $E_{in}$ (kWh) in <i>zone II</i> over the 54.5 min time duration= 0.2259 kWh. The difference in $Q_{loss}$ values is attributed to the different assumptions employed in the calculations .....	68
<b>Table s3.2:</b> The overall energy input to the reactor and the final pressure after cooling for 1 h thermal cracking of different feedstocks at 400°C, natural pressure and 0 rpm, unless otherwise noted. ....	69
<b>Table 4.1:</b> Summary of literature work on catalytic cracking of VR.....	76
<b>Table 4.2:</b> The total energy input to the reactor and the final pressure after cooling for thermal cracking of AVR at 400°C with and without alumina NPs. ....	96
<b>Table 4.3:</b> Reaction rate constants per reaction (R2) for control samples at different operating conditions and their ratios in presence of different additives. ....	107
<b>Table s4.1:</b> particle size and geometric surface area calculated from TEM and SEM images of different samples.....	114
<b>Table s4.2:</b> The overall energy input to the reactor and the final pressure after cooling for thermal cracking of AVR at different reaction temperature and DC content. ....	121
<b>Table s4.3:</b> Analysis of gaseous product from thermal cracking of AVR at (a) 400°C control; (c) 400°C containing in situ NPs; (h) 420°C control; (i) 420°C containing 10 wt% DC....	122
<b>Table s4.4:</b> Reaction rate constants ( $k$ ) and heat of reaction ( $\Delta H_{rxn}$ ) per reaction (R4.2) for control samples in presence of different additives at different operating conditions. ....	125

## List of Figures and Illustrations

<b>Figure 1.1:</b> Total primary energy supply by fuel in 1971 and 2014 (International Energy Agency 2016).....	14
<b>Figure 1.2:</b> Word’s hydrocarbon reserves distribution (Radial Drilling 2014). .....	15
<b>Figure 2.1:</b> Crude oil classification according to the solubility of the oil in toluene and <i>n</i> -heptane (modified from (Trejo & Rana 2010)).....	20
<b>Figure 2.2:</b> Classification of heavy oil upgrading and operating conditions for some of the technologies (modified from (Speight & Özüm 2002; Rana <i>et al.</i> 2007)) .....	22
<b>Figure 2.3:</b> Reactions involve in thermal cracking (modified from (Rahimi & Gentzis 2006)) .	24
<b>Figure 3.1:</b> Schmatic representation of the experimental procedures involved in this work.....	36
<b>Figure 3.2:</b> Block diagram illustrating the experimental variables and condition. ....	36
<b>Figure 3.3:</b> Energy consumption and pressure buildup inside the batch reactor during the thermal cracking at 400°C of (◆,◇) AVR for 1 h, (▲,△) AVR for 2 h, (◆,◇) AVR for 1 h, and (▲,△) AVR for 2 h. ....	39
<b>Figure 3.4:</b> Product yield based on the AVR or AVR for 1 h, (b) AVR for 2 h, (c) AVR for 1 h, and (d) AVR for 2 h. ....	41
<b>Figure 3.5:</b> Product yield, based on the AVR or AVR for 1 h, (b) AVR for 2 h, (c) AVR for 1 h, and (d) AVR for 2 h. ....	44
<b>Figure 3.6:</b> Product yield based on the AVR or AVR for 1 h, (b) AVR for 2 h, (c) AVR for 1 h, and (d) AVR for 2 h. ....	46
<b>Figure 3.7:</b> Product yield based on the AVR feedstock (A), and product yield based on the parent Athabasca VR (B). °API gravity of the product oil and its maltene extract (C). Viscosity at 37°C of the product oil, the product oil w/o TI and its maltene extract (D) for the thermal cracking at (g) 400°C and (m) 420°C .....	47

<b>Figure 3.8:</b> Product yield based on the AVR or AVRМ feedstock (A), and product yield based on the parent Athabasca VR, (B). °API gravity of the product oil and its maltene extract (C). Viscosity at 37°C of the product oil, the product oil w/o TI and its maltene extract (D) for 1 h thermal cracking at 400°C of (a) AVR, (i) AVRМ with the addition of 10 wt% asphaltenes, and (c) AVRМ. ....	50
<b>Figure 3.9:</b> Product yield based on the AB or ABМ feedstock (A), and product yield based on the parent Athabasca bitumen (B). °API gravity of the product oil and its maltene extract (C). Viscosity at 37°C of the product oil, the product oil w/o TI and its maltene extract (D) for the 1 h thermal cracking at 400°C of (j) AB, (k) ABМ with 5 wt% added asphaltenes, and (l) ABМ. ....	51
<b>Figure 3.10:</b> Difference between initial asphaltenes (Asphi) in the feedstock and asphaltenes yield from the thermal cracking (Asphp) for thermal cracking of (a) Athabasca VR and (b) Athabasca bitumen at different initial asphaltenes content in the feedstock.....	52
<b>Figure 3.11:</b> Overall asphaltenes yield from the thermal cracking of (a) Athabasca VR and (b) Athabasca bitumen at different initial asphaltenes content in the feedstock.....	52
<b>Figure 3.12:</b> High-temperature simulated distillation curves of (a) AVR and (u) product oil from thermal cracking of AVR at 400°C and 0 rpm for 1 h. ....	54
<b>Figure 3.13:</b> TG and DSC curves of TI Product for the thermal cracking of AVR at 400°C and 420°C.....	56
<b>Figure s3.1:</b> Temperature variation and cumulative energy input to the reactor for thermal cracking of AVR at 400°C.....	61
<b>Figure s3.2:</b> Temperature variation and cumulative energy input to the reactor for heating the glass material at 400°C. ....	62
<b>Figure s3.3:</b> Schematic representation of the reactor unit. ....	65
<b>Figure s3.4:</b> Schematic representation of the mantle unit.....	67
<b>Figure s3.5:</b> Energy consumption and pressure buildup inside the batch reactor during the thermal cracking at 400°C and 1 h of (♦,◇) AVR, (●,○) AVR pressurized to 350 psi, (◆,◇) AVRМ, and (●,○) AVRМ, pressurized to 350 psi. ....	70
<b>Figure s3.6:</b> Energy consumption and pressure buildup inside the batch reactor during the thermal cracking at 400°C for 1 h, of (♦,◇) AVR, (■,□) AVR with mixing at 500 rpm after the reactor reaches 300°C, (◆,◇) AVRМ, and (■,□) AVRМ with mixing at 500 rpm after the reactor reaches 300°C .....	70
<b>Figure s3.7:</b> Energy consumption and pressure buildup inside the batch reactor during the thermal cracking for 1h of AVR at (■,□) 400°C and (●,○) 420°C .....	71

<b>Figure s3.8:</b> Energy consumption and pressure buildup inside the batch reactor during the thermal cracking at 400°C for 1 h of (◆,◇) VR, (●,○) AVR with 10 weight% asphaltenes, and (▲,△) AVR	71
<b>Figure s3.9:</b> Energy consumption and pressure buildup inside the batch reactor during the thermal cracking at 400°C for 1 h, of (■,□) AB, (●,○) ABM with 5 wt% asphaltenes, and (▲,△) ABM	72
<b>Figure 4.1:</b> Flow diagram of the experimental procedures involved in this work.	83
<b>Figure 4.2:</b> Block diagram summarizing the experimental variables and conditions.	83
<b>Figure 4.3:</b> (a) XRD pattern of as received <i>commercial</i> Al <sub>2</sub> O <sub>3</sub> NPs; (b) XRD pattern, (c) EDX pattern, (d) SEM image and (e) the particle size distribution histogram of the TI following thermal cracking of AVR in presence of <i>commercial</i> Al <sub>2</sub> O <sub>3</sub> NPs; (f) EDX pattern, (g) SEM image and (h) the particle size distribution histogram of leftover material from STA analysis of the TI.	87
<b>Figure 4.4:</b> (a) XRD pattern, (b) EDX pattern, (c) SEM image and (d) the particle size distribution histogram of TI following thermal cracking of AVR in presence of <i>in situ</i> prepared Al <sub>2</sub> O <sub>3</sub> NPs; (e) EDX pattern, (f) SEM image and (g) the particle size histogram of leftover material from STA analysis of the TI.	89
<b>Figure 4.5:</b> (a) XRD pattern of the as received DC; (b) XRD pattern, (c) SEM image with C EDX mapping, (d) SEM image with Si EDX mapping, (e) SEM photograph, (f) DC particle size distribution histogram of TI following thermal cracking of AVR in presence of of 10 wt% DC at 420°C; (g) EDX pattern, (h) SEM photograph, (i) DC particle size distribution of leftover material of STA analysis of the TI.	92
<b>Figure 4.6:</b> (a) EDX of area 1 (b) EDX of area 2 corresponding to (c) zoomed in SEM image, (d) zoomed out SEM image of control TI following thermal cracking of AVR at 420°C; (e) EDX pattern and (f) SEM image of leftover materials from STA analysis of <i>asphaltenes</i> from AVR.	94
<b>Figure 4.7:</b> Energy consumption and pressure buildup inside the batch reactor during thermal cracking at 400°C for: (◆,◇) AVR, (■,□) AVR with 10,000 ppm <i>commercial</i> Al <sub>2</sub> O <sub>3</sub> NP, (▲,△) AVR with 6,000 ppm <i>in situ</i> Al <sub>2</sub> O <sub>3</sub> NP.	96
<b>Figure 4.8:</b> Product yield (A) °API gravity of the product oil and maltene (B), Viscosity at 37°C of the product oil and the maltene product (C) for thermal cracking at 400°C of (a) AVR, (b) AVR with 10,000 ppm <i>commercial</i> NP, and (c) AVR with 6,000 ppm <i>in situ</i> NPs.	99
<b>Figure 4.9:</b> Product yield (A), °API gravity of the product oil and maltene (B), viscosity at 37°C of the product oil and the maltene product (C) for thermal cracking at 400°C of (d) AVR, (e) AVR with 10 wt% DC, (f) AVR with 20 wt% DC, and (g) AVR with 30 wt% DC.	103

<b>Figure 4.10:</b> Product yield (A), °API gravity of the product oil and maltene (B), Viscosity at 37°C of the product oil and the maltene product (C) for thermal cracking at 420°C of: (h) AVR, (i) AVR with 10 wt% DC. ....	105
<b>Figure 4.11:</b> H/C ratio of TI and asphaltenes product for thermal cracking of control AVR and AVR with 10 wt% DC at 420°C and H/C ratio of original asphaltenes from AVR. ...	108
<b>Figure 4.12:</b> %Mass loss and heat flow profiles of the TI product for the thermal cracking of control AVR (black) and AVR with 10 wt% DC (grey) at 420°C. Thin lines represent the standard deviation for three replicates. ....	109
<b>Figure 4.13:</b> %Mass loss and heat flow profiles of different initial masses of the asphaltenes fraction from thermal cracking of AVR at 420°C.....	110
<b>Figure 4.14:</b> Conv 545 <sup>+</sup> and condensable gas wt% of products from thermal cracking of AVR (a) at 400°C and 0 rpm control (c) at 400°C and 0 rpm containing <i>in situ</i> NPs; (h) at 420°C control and 500 rpm, (i) at 420°C and 500 rpm containing 10 wt% DC. Condensable gas wt% is based on the gas sample.....	112
<b>Figure s4.1:</b> (a) TEM image and (b) corresponding particle size distribution histogram of as received <i>commercial</i> Al <sub>2</sub> O <sub>3</sub> NPs employed in this study.....	115
<b>Figure s4.2:</b> (a) SEM image with C EDX mapping, (b) SEM image with Si EDX mapping, (c) SEM image with Al EDX mapping, and (d) SEM image with O EDX mapping of TI following thermal cracking of AVR in <i>commercial</i> Al <sub>2</sub> O <sub>3</sub> NPs employed in this study....	115
<b>Figure s4.3:</b> (a) TEM, (b) SEM photograph with EDX mapping of Al and O of TI following thermal cracking of AVR in presence of <i>in situ</i> Al <sub>2</sub> O <sub>3</sub> particles and (c) SEM image of left over material from STA heat treating of TI following thermal cracking of AVR in presence of <i>in situ</i> prepared Al <sub>2</sub> O <sub>3</sub> NPs at 400°C. ....	116
<b>Figure s4.4:</b> EDX pattern and corresponding SEM photograph, TI following thermal cracking of AVR in presence of <i>in situ</i> Al <sub>2</sub> O <sub>3</sub> particles at 400°C.....	117
<b>Figure s4.5:</b> (a) SEM image with C EDX mapping, (b) SEM image with Si EDX mapping, (c) SEM image with Al EDX mapping, and (d) SEM image with O EDX mapping of TI following thermal cracking of AVR in presence of <i>in situ</i> Al <sub>2</sub> O <sub>3</sub> particles at 400°C.....	117
<b>Figure s4.6:</b> (a) SEM image with C EDX mapping, (b) SEM image with Si EDX mapping, (c) SEM image with Al EDX mapping, and (d) SEM image with O EDX mapping of TI following thermal cracking of AVR 420°C in presence of 10 wt% DC, (b) SEM photograph with Al and Si EDX mapping of left over material of STA analysis of TI following thermal cracking of AVR in presence of 10 wt% DC at 420°C .....	118
<b>Figure s4.7:</b> (a) SEM image with C EDX mapping, (b) SEM image with Si EDX mapping, (c) SEM image with Al EDX mapping, and (d) SEM image with O EDX mapping of TI following thermal cracking of AVR in presence at 420°C. ....	118

**Figure s4.8:** (a) SEM image with EDX mapping and (b) SEM photograph of left over material of STA analysis of TI following thermal cracking of AVR in presence at 420°C..... 119

**Figure s4.9:** Energy consumption and pressure buildup inside the batch reactor during the thermal cracking at 400°C of: (■,□) AVR, (▲,△) AVR with 10 wt% DC, (◆,◇) AVR with 20 wt% DC, (●,○) AVR with 30 wt% DC..... 120

**Figure s4.10:** Energy consumption and pressure buildup inside the batch reactor during the thermal cracking at 420°C of: (◆,◇) AVR and (●,○) AVR with 10 wt% DC. .... 121

**Figure s4.11:** High-temperature simulated distillation curves of (o) AVR, (a) product oil from thermal cracking of AVR at 400°C and 0 rpm (c) product oil from thermal cracking of AVR at 400°C and 0 rpm containing in situ NPs, (h) product oil from thermal cracking of AVR at 420°C and 500 rpm, (i) product oil from thermal cracking of AVR at 420°C and 500 rpm containing 10 wt% DC..... 122

## List of Symbols, Abbreviations and Nomenclature

<i>Symbol</i>	<i>Definition</i>
PAVR	Parent Athabasca vacuum residue
AVR	Athabasca vacuum residue
AVRM	Maltene extracted from Athabasca vacuum residue
AB	Athabasca bitumen
ABM	Maltene extracted from Athabasca bitumen
TI	Toluene insolubles
$wt\%_{PAVR}$	Weight percent base on parent Athabasca vacuum residue (wt%)
$wt\%_{AVR}$	Weight percent base on Athabasca vacuum residue feedstock (wt%)
$Asph_{pr}$	Product asphaltenes
$Asph_i$	Initial asphaltenes in feedstock
$Conv_{545^{\circ}C}$	Reduction of material with boiling point higher than 545°C in upgraded samples compared to feedstock
$Mass\ of\ 545^{\circ}C_{feed}$	Mass of the material with boiling point higher than 545°C in feedstock
$Mass\ of\ 545^{\circ}C_{product}$	Mass of the material with boiling point higher than 545°C in product oil

## Chapter One: Introduction

### 1.1 Motivation

According to the International Energy Agency (IEA), the world energy consumption increased almost 2.5 times between 1971 and 2014 (International Energy Agency 2016). Figure 1.1 shows that oil contribution to the energy portfolio decreased from 44% to 31% between these years. Nevertheless, oil is still the largest energy source (U.S. Energy Information Administration 2016), by virtue of its high energy density per unit volume and suitability for mobile engines. It is anticipated that between 2014 and 2040 the world energy demand will increase by 37%. Consequently, the demand on oil is expected to rise from its current 14 mb/d to reach 104 mb/d in 2040 (International Energy Agency 2014; U.S. Energy Information Administration 2016).

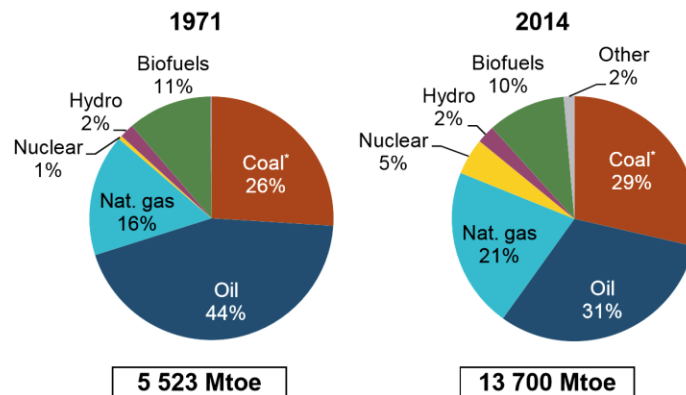


**Figure 1.1:** Total primary energy supply by fuel in 1971 and 2014 (International Energy Agency 2016).

Only a third of the global hydrocarbon resource is conventional. The rest is unconventional, as depicted in Figure 1.2 (Radial Drilling 2014). Heavy oil and bitumen are examples of unconventional hydrocarbon resources and combined together contribute to 34% of the total hydrocarbon proven reserves (Radial Drilling 2014).

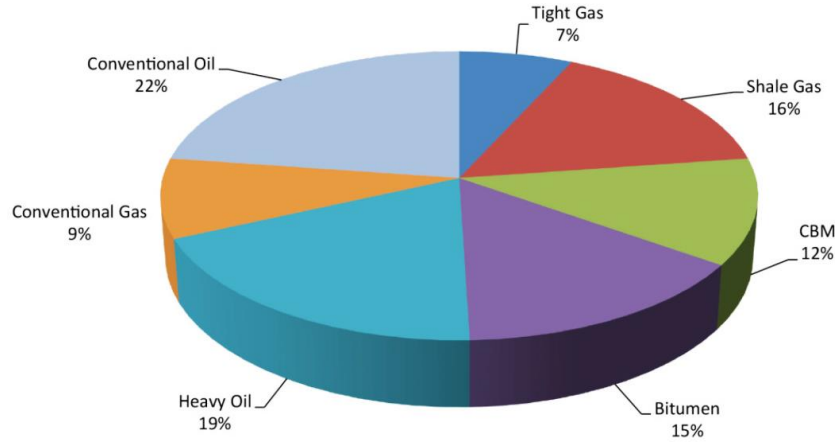


**Figure 1.2:** World's hydrocarbon reserves distribution (Radial Drilling 2014).

As the world's conventional reserves are limited and not widely spread, attention has turned to unconventional heavy oil resources to meet the current and future energy needs (Al-Marshed *et al.* 2015). In order to increase the value of heavy oil and reduce the environmental impact associated with its utilization, petroleum industries employ different upgrading technologies (Oil and Energy Trends 2006; Gray 2015).

Upgrading of heavy oil involves converting the low value heavy fractions into high value light fractions with higher H/C ratio. This improvement is accompanied by viscosity reduction, °API gravity increase and removal of heteroatoms from the oil (Asgharzadeh Shishavan *et al.* 2011; Singh *et al.* 2004; Yang *et al.* 1998; Gray 2015). In general, heavy oil upgrading consists of a sequence of processes based on carbon rejection and hydrogen addition that can be conducted in presence or absence of a catalyst. An upgrading process is only economical if the difference between the price of light and heavy crudes is high enough to pay off the cost of production and upgrading (Oil and Energy Trends 2006). Accordingly, there is a continuous need to improve heavy oil upgrading methods to make them more cost effective.

Thermal conversion is the most popular upgrading process by virtue of its low operating complexity and low capital and operating cost (Gray 2015). During thermal conversion, the molecular structure of the feedstock changes chemically. In general, bigger molecules are cracked into smaller ones. Improving the upgraded product by adding hydrogen is imperative because of the high hydrogen deficiency of heavy oil. In hydrocracking reaction, bigger molecules are cracked leading to radical formation, which in turn react with hydrogen and hence inhibit major polymerization reactions (Banerjee 2012). Hydrocracking products are typically considered more stable as a result of radical termination with hydrogen. Despite these advantages, hydrocracking reactions are costlier and more difficult to run on a large scale, especially in light of the hydrogen and catalyst requirements (Gray 2015). Therefore, focusing the effort on improving thermal cracking to achieve higher yield of the lighter liquid product may be more feasible. In practice, coke formation is a major hurdle in attaining maximum conversion to lighter liquid cuts. Therefore coke suppression is an important step in maximizing the yield of thermal conversion (Wang *et al.* 2016a). The optimum operating condition for thermal cracking is highly dependent on the feedstock and the operating conditions (Hauser *et al.* 2014; Shen *et al.* 2008; Henderson & Weber 1965). Employing a small amount of an effective catalyst or an inexpensive catalyst that may not need regeneration may further boost the process. A Well dispersed nanoparticle (NP) catalyst could improve thermal cracking of heavy oil at low concentration by virtue of its high surface area and high degree of dispersion, which reduce the mass transfer barrier (Husein & Alkhaldi 2014; Abu Tarboush & Husein 2012a; Abu Tarboush & Husein 2015). On the other hand, catalysts are inherently expensive and tend to increase the processing cost. One alternative is to use drilling cuttings (DC). DC is a by-product of oil exploration and production with a potential to catalyze heavy oil upgrading reactions due to abundance of active sites resulting from defective crystals.

## 1.2 Objectives

This work aims at exploring more efficient methods for bitumen and vacuum residue upgrading. More specifically, methods based on thermal and catalytic thermal cracking will be investigated. Athabasca vacuum residue and Athabasca bitumen were selected as examples of heavy oil.

Short term objectives focus on understanding of the effect of process conditions such as pressure, temperature, stirring rate, reaction time, asphaltene content, operation mode and catalysts on thermal cracking in closed system arrangement in order to identify optimum conversion conditions. Performance parameters include energy consumption, percent conversion to the different products, conversion of the residue, viscosity and specific gravity of the product oil and its maltene fraction.

In order to achieve these goals, this study is divided into four main phases:

Phase one studies the effect of several operating conditions toward thermal cracking of Athabasca vacuum residue and bitumen in closed system arrangement, in which the gases are not allowed to vent during the reaction.

Phase two investigates the effect of operating conditions in the presence and absence of asphaltene, in order to identify the role of asphaltene in thermal cracking reactions.

Phase three explores the effect of *in situ* prepared and *commercial* alumina NP and their catalytic activity toward thermal cracking.

Phase four investigates the role of drill cuttings (DC) toward thermal cracking.

## 1.3 Outline of the thesis

This is a paper based thesis. Two papers, one published in *Fuel* (Eshraghian & Husein 2017) and another was submitted to a journal, covering Phases One and Two and Phases Three and Four constitute Chapters Three and Four of the thesis. Each of the chapters has its own detailed

introduction, experimental procedure, result and discussion, conclusions, and supporting material sections.

In Chapter 3, thermal cracking of Athabasca vacuum residue (AVR) and Athabasca bitumen (AB) and their maltene fraction at 400°C in a closed system (an autoclave) is considered. The effect of the following variables on the extent of the thermal cracking reactions are investigated; residence time, pressure of the reactor unit, stirring, temperature, and asphaltenes content of the feedstock. Key performance measures were the product yield, the properties of the liquid fraction and its maltene extract, the total energy consumption, and the pressure buildup in the batch reactor. Several detection techniques were employed to measure the quantity and quality of the reaction products; including high-temperature simulated distillation (HTSD) analysis and gas chromatography (GC).

In Chapter 4, the catalytic thermal cracking of Athabasca VR (AVR) by means of *commercial* and *in situ* prepared alumina NP and drill cuttings (DC) was investigated. The same key performance measures were employed. In addition to the techniques employed above, simultaneous thermal analysis (STA) and elemental analysis were used to explore the chemical nature of the toluene insolubles (TI), which are typically collected with the catalyst.

In Chapter 5, the main conclusions drawn from this work are summarized and the major contributions to knowledge are highlighted.

## Chapter Two: Literature review

In this section, an overview of heavy oil properties and the current state of knowledge of heavy oil upgrading with a focus on thermal and catalytic thermal cracking is presented. First, properties and composition of heavy oil feedstocks as well as common heavy oil upgrading are reported. Then an overview of thermal cracking and catalytic thermal cracking are discussed with a special emphasis on coke formation.

### 2.1.1 Unconventional oil

Crude oils are classified based on their physical properties such as viscosity and °API gravity. bitumen and heavy oils are known by their high viscosity, low °API gravity, low hydrogen to carbon ratio, and high asphaltenes and heteroatom content, which complicate their processing (Nassar *et al.* 2011a; Abu Tarboush & Husein 2012a). Typical classifications and physical properties of different types of crude oils are given in Table 2.1.

**Table 2. 1:** Definition and classification of petroleum material (Gray 2015).

Type of Oil	Definition of oil	°API gravity	Viscosity (mPa.s)
Unconventional	Bitumen	<10	>10 <sup>5</sup>
	Extra Heavy Oil	<10	>10 <sup>5</sup>
	Heavy Oil	10-19	10 <sup>5</sup> -10 <sup>5</sup>
Conventional	Medium Crude Oil	19-34	-
	Light Crude Oil	34-42	-
	Condensate	>45	-

Residues are also considered as heavy oils because of their low H/C ratio and high metal content (Oballa & Shih 1994). There are two types of residue: atmospheric residue and vacuum residue, corresponding to atmospheric and vacuum distillation processes, respectively (Rana *et al.* 2007).

Crude oils consist of a wide range of hydrocarbons with different molecular size and structures. A detailed analysis of crude oil specifications and composition is very complex. Solubility of crude oil in different solvents is one method to characterize the oil (Banerjee 2012). Figure 2.1 summarizes the chemical classification of crude oil based on its solubility (Trejo & Rana 2010; Rahimi & Gentzis 2006; Speight 2011). Note that heavier fractions of heavy oil have higher heavy metal content (e.g. Ni, V, etc.).

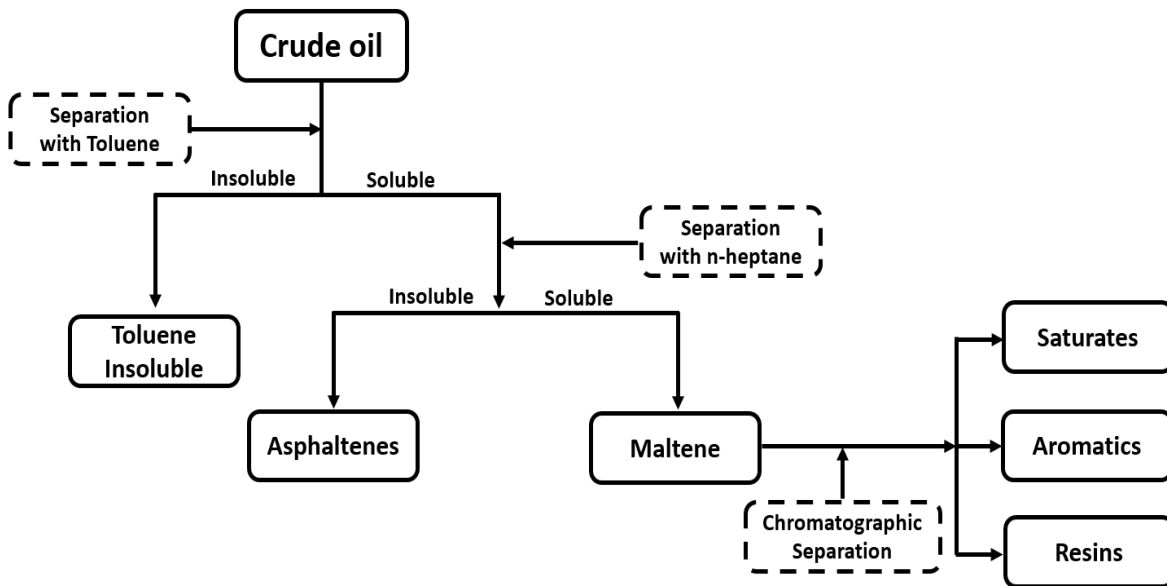


**Figure 2.1:** Crude oil classification according to the solubility of the oil in toluene and *n*-heptane (modified from (Trejo & Rana 2010)).

### 2.1.2 Asphaltenes

Asphaltenes are defined as polar, high molecular weight, low °API gravity, and high boiling point hydrocarbon fraction of the crude which is insoluble in *n*-alkanes (e.g. *n*-heptane) while soluble in aromatic solvent such as toluene (Ancheyta *et al.* 2005; Trejo *et al.* 2005; Trejo 2005; Lababidi *et al.* 2014). Asphaltenes are the most problematic fraction in heavy oil and are responsible for coke formation that cause deactivation of catalysts (Avid *et al.* 2004). Asphaltenes precipitation during

production and transportation of oil depends on the operating pressure and temperature. Heavy oils usually have a higher asphaltenes content relative to conventional oils (Gray 2015).

### **2.1.3 The upgrading process**

Upgrading of heavy oil is the process of producing higher quality petroleum fractions, and it includes removal of contaminants, reduction in viscosity, and increase in °API gravity. The economic efficiency of an upgrading process depends on the difference in price between the low-value feed material and high-value light upgraded material, the existence of markets for upgraded oil, and the cost of operating an upgrader (Oil and Energy Trends 2006). Upgrading of heavy oil involves three major process: separation, carbon rejection, and hydrogen addition. Figure 2.2 shows the classification of heavy oil upgrading processes. There are advantages and disadvantages in the operating and the economic aspects of each of these technologies (Castañeda *et al.* 2014; Ortiz-Moreno *et al.* 2012; Angeles *et al.* 2014; Rana *et al.* 2007; Castañeda *et al.* 2012; Robinson 2006). Lower complexity and operating cost for thermal cracking process is one of its advantages, compared with hydrogen addition processes (Rana *et al.* 2007).

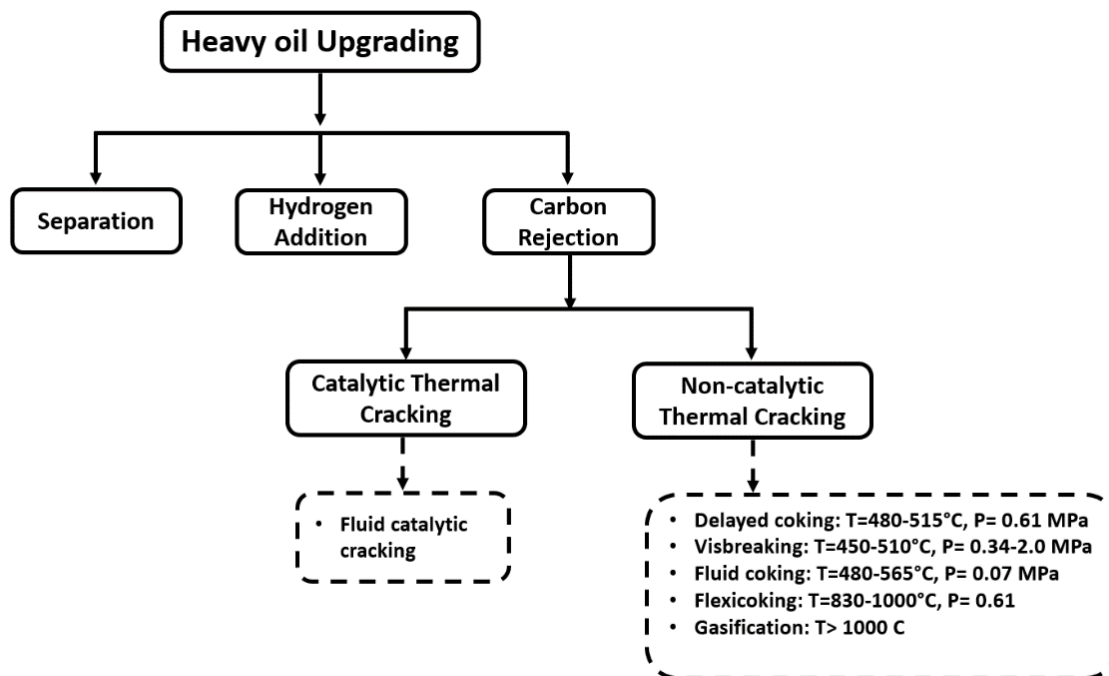


**Figure 2.2:** Classification of heavy oil upgrading and operating conditions for some of the technologies (modified from (Speight & Özüm 2002; Rana *et al.* 2007))

#### 2.1.4 Non-catalytic thermal cracking

Thermal cracking of hydrocarbons involves cleavage of C-C bonds through radical reactions with the objective of breaking down the large molecules of heavy oil into smaller ones, which occurs at temperatures higher than 350°C (Gray & McCaffrey 2002). In commercial non-catalytic thermal cracking process, a temperature of at least 420°C is required. This process is compatible with different feeds because the reactions rely on heat without the requirement of a catalyst or solvent. There are several thermal cracking processes as depicted in Figure 2.2, which differ in operating parameters such as temperature, pressure, reaction time, and reactor type and size (Banerjee 2012). Visbreaking is a mild thermal cracking treatment performed with the objective of viscosity reduction of the heavy oil by 5-10 times to provide smoother transportation through pipelines (Speight 2012). The visbreaking process takes place in furnaces having a temperature range

between 450°C and 510°C, pressure of 0.34-2 MPa, and residence time of 1-5 mins (Banerjee 2012; Gray 2015). Higher temperatures and reaction times are avoided to prevent coke formation (Gray 2015). Coking is a form of thermal conversion that occurs at very high temperatures, in which the coke forms (Rana *et al.* 2007). Delayed coking and fluid or flexi coking are the major commercial coking processes (Banerjee 2012). Delayed coking is the most commonly used among all commercial coking processes, and it is a semi-batch process operating at high temperatures of 480-515°C with a high cycle time of 12-48 h, to convert the heavy oil to lighter hydrocarbons and coke. (Wiehe 1993). Fluid coking is a continuous process operating at high temperatures of 480-565°C. As the name suggests, coking of the sprayed feed occurs on the surface of fluidized coke particles. The liquid is separated from the coke by steam and some coke is also burned to provide heat for the reactor (Banerjee 2012).

### **2.1.5 The chemistry of thermal cracking**

Many complex reactions mechanisms are associated with thermal cracking of hydrocarbons. Figure 2.2 shows the thermal cracking reaction of a hypothetical molecule of M. Heat- breaks a C-C bond of M and splits it into two free radicals. Then, propagation reactions take place and hydrogen transfers from nearby molecules to produce a radical of parent (H-donor) molecules. Next the parent radical undergoes a B-scission reaction to produce more free radicals. Finally, the recombination of free radicals produces heavier molecules (Gray & McCaffrey 2002; Rahimi & Gentzis 2006). The molecules that recombine to form heavier molecules eventually form a separate heavier phase (Alvarez *et al.* 2011; Speight 2014).

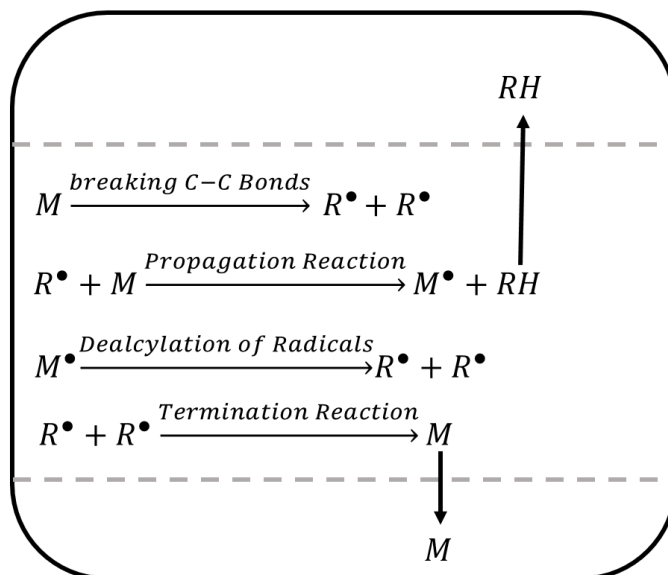


**Figure 2.3:** Reactions involve in thermal cracking (modified from (Rahimi & Gentzis 2006))

When the concentration of heavier molecules with high molar mass and aromaticity in the liquid phase reach a critical concentration, phase separation occurs (Khorasheh & Gray 1993; Gray 2015). This highly aromatic and dense phase may also separate as mesophase which is responsible for coke formation. Carbonaceous solids of coke contains high carbon content, and it is an unwanted, low-value by-product of thermal cracking of heavy oil (Rahimi *et al.* 1999; Tanabe & Gray 1997; Wang *et al.* 2016a; Gray 2015; Khorasheh & Gray 1993). Therefore, reducing the amount of coke formation increases the lighter hydrocarbon yield and efficiency of the upgrading process (Gray 2015). More aromatic feedstock with higher asphaltenes content, tend to form higher amount coke (Wiehe 1993).

### 2.1.6 Catalytic cracking

Catalysis is one of the essential tools in oil processing technologies. Cracking reactions can take place on catalysts with acidic support. Amorphous oxides (e.g. silica-alumina, crystalline zeolite modified with Y-zeolite) plus binder such as alumina are acidic supports. Parameters such as activity, stability and selectivity are key performance parameters for cracking catalysts which

depend on the formulation and the physical and textural properties of the catalyst (Gruia 2006; Liu *et al.* 2009). Catalytic cracking begins with cracking of paraffin over acidic sites of catalyst to form carbonium ions; that is, hydrocarbon ions with a positive charge on carbon atom. The carbonium ions desorb from the catalyst and collapse in a termination step to produce light hydrocarbons or hydrogen (Gong *et al.* 2008).

### **2.1.7 *In situ* prepared nanoparticles**

Ultra-dispersed catalysts provide a potential solution for some of the problems encountered when using bulk supported catalysts such as deactivation, coke formation, and low catalytic effect due to diffusion limitations (Del Bianco, Panariti, Di Carlo, *et al.* 1993). Nano-scale size of catalysts provide higher surface to volume ratios and improve the physical and chemical properties of the catalyst by reducing the internal and external mass transfer resistance (Abu Tarboush & Husein 2015; Husein & Alkhaldi 2014; Hashemi *et al.* 2014; Hosokawa 2012).

Nanoparticles can be provided through physical or chemical techniques. There are five chemical methods for preparing nanoparticles: the chemical co-precipitation, electrochemical, sonochemical, sol-gel, and micro-emulsion methods (Husein & Nassar 2008). All of these methods need stabilizing agent to hinder aggregation of produced nanoparticles. In the micro emulsion method, a thermodynamically stable mixture of oil and water is stabilized with the aid of surfactant. Nano-sized water droplets are dispersed in the continuous oil phase. Synthesizing nanoparticles using microemulsion method consists of mixing two macroemulsions containing appropriate reactants to produce the desired particles. Different studies have been done on the preparation of nano particles in heavy oil medium using the micro emulsion method. (Husein & Alkhaldi 2014; Abu Tarboush & Husein 2015; Husein & Nassar 2008). The use of alumina as catalyst and/or support has been studied extensively (Nassar *et al.* 2011b; Husein & Alkhaldi 2014;

Yao *et al.* 2001b). An experimental investigation on the effects of *in situ* prepared alumina nanoparticles on the thermal cracking of a mixture of Athabasca vacuum gas oil and vacuum residue at 350°C showed that the °API gravity of product oil improved while the its viscosity increased due to cross linking (Husein & Alkhaldi 2014). The performance of the *in situ* prepared alumina nano particles was limited by particles agglomeration (Husein & Alkhaldi 2014).

### **2.1.8 Role of fine solid in cracking**

Phase separation and consequent coke formation during cracking of hydrocarbons is sensitive to the surface-to-volume ratio because the surface-to-volume ratio is a significant factor in the hydrogen transfer between the coke phase and the liquid phase (Gray 2015). Coke precursors typically accumulate on the surface of solids, whenever present in heavy oil, which provides better dispersion and exposure to react more rapidly with hydrogen donors from the bulk oil phase (Sanaie *et al.* 2001). In addition, coke precursors inhibited from coalescence to form bigger coke particles. According to studies, coke precursors reaction with hydrogen donors suppressed coke formation and growth significantly (Rahmani *et al.* 2002). Subsequently, when fine solids are present, the yield of toluene insoluble (TI) product decreases and higher severity operating conditions can be used (Nhieu *et al.* 2016; Tanabe & Gray 1997; Sanaie *et al.* 2001; Wang *et al.* 1998; Bi *et al.* 2007; Rahimi *et al.* 1999; Gray 2015).

## Chapter Three: Thermal cracking of Athabasca VR and bitumen and their maltene fraction in a closed reactor system\*

Afroz Eshraghian and Maen M. Husein\*\*  
*Department of Chemical & Petroleum Engineering, University of Calgary, Calgary, AB,  
Canada T2N 1N4*

### 3.1 Abstract

Thermal cracking of Athabasca vacuum residue (AVR) and Athabasca bitumen (AB) and their maltene fraction was investigated at 400°C in a closed system, i.e. autoclave. The effect of the following variables on the product yield and the properties of the liquid fraction and its maltene extract was evaluated: residence time, pressure of the reactor unit, stirring, temperature and asphaltenes content of the feedstock. The yield of the different fractions, the total energy consumption, the pressure buildup in the batch reactor and the °API gravity and viscosity of the liquid fraction and its maltene extract were used to evaluate the impact of each parameter. In addition, high-temperature simulated distillation (HTSD) analysis of the liquid product and gas chromatography (GC) analysis for gas product were performed. The effect of reaction time, mixing and pressure on the yield of toluene insolubles (TI) depended on the presence of asphaltenes in the feedstock. TI yield increased at the expense of the asphaltenic fraction when reaction time, mixing and pressure increased. There is an inverse relationship between the initial asphaltenes content in the feedstock and the overall asphaltenes yield based on the parent feedstock. Moreover, increasing the asphaltenes content of the feedstock did not introduce significant changes in the total energy input to the reactor.

*Keywords: thermal cracking, Athabasca, VR, bitumen, heavy oil, asphaltenes, maltene*

---

\* Eshraghian, A. & Husein, M.M., Fuel, 2017, 190, 396–408

\*\*Correspondence address: Department of Chemical & Petroleum Engineering, University of Calgary, Calgary, AB, Canada  
T2N 1N4, Tel: (403) 220-6691; Fax: (403) 282-3945; E-mail: maen.husein@ucalgary.ca

### 3.2 Introduction

There is a growing interest in upgrading heavy oil due to an increased demand on liquid fuel coupled with the need to improve the transportability of heavy crude. The presence of asphaltenes, the constituents of heavy oil with the highest molecular weight and polarity, complicates heavy oil recovery, transportability and processing (Speight 2004). Upgrading of heavy oil involves a conversion of low value feedstock, the heavy fraction, to high value light fractions with higher H:C ratio (Asgharzadeh Shishavan *et al.* 2011; Singh *et al.* 2004; Yang *et al.* 1998). Thermal cracking is an example of carbon rejection upgrading process at temperatures higher than 350°C. It targets maximizing the yield of the light fractions and lowering the viscosity of the liquid product at the expense of producing some coke (Speight 2004). The advantages of thermal cracking processes stems from their lower complexity and operating expense as compared with hydrocracking processes (Rana *et al.* 2007). Nevertheless, to improve the feasibility and efficiency of thermal cracking, it is important to control coke and asphaltenes formation and maximize the production of light oil (Rahmani *et al.* 2002; Henderson & Weber 1965).

The quality of the thermal cracking product depends on the properties of the feedstock, the process conditions, the processing technology and the cracking catalyst, whenever applied (Hauser *et al.* 2014; Shen *et al.* 2008; Henderson & Weber 1965). A number of experimental studies have been reported on thermal cracking of different kinds of heavy oils (AlHumaidan *et al.* 2013; Al-Soufi *et al.* 1988; Asgharzadeh Shishavan *et al.* 2011; Bello *et al.* 2006; Carbognani *et al.* 2007; Del Bianco, Panariti, Anelli, *et al.* 1993; Di Carlo & Janis 1992; Ebrahimi *et al.* 2008; Gray *et al.* 2008; Gray *et al.* 2004; Hauser *et al.* 2014; Henderson & Weber 1965; Hill *et al.* 1996; Krishna *et al.* 1988; Mallinson *et al.* 1992; Marriott *et al.* 2013; Martínez-Escandell *et al.* 1999; Shen *et al.* 2008; Shu & Venkatesan 2013; Singh *et al.* 2004; Vafi *et al.* 2012b; Wang *et al.* 2014; Yue *et al.*

2004). Some focused on the effect of process conditions on product yield and/or properties (Al-Soufi *et al.* 1988; Asgharzadeh Shishavan *et al.* 2011; Bello *et al.* 2006; Carbognani *et al.* 2007; Del Bianco, Panariti, Anelli, *et al.* 1993; Di Carlo & Janis 1992; Ebrahimi *et al.* 2008; Gray *et al.* 2008; Henderson & Weber 1965; Hill *et al.* 1996; Krishna *et al.* 1988; Mallinson *et al.* 1992; Martínez-Escandell *et al.* 1999; Shen *et al.* 2008; Wang *et al.* 2014; Yue *et al.* 2004; Sawarkar *et al.* 2007) and reported that appreciable thermal cracking typically takes place at temperature higher than 350-370°C (Del Bianco, Panariti, Anelli, *et al.* 1993), while the effect of pressure, temperature and reaction time on product yield and properties depended on the chemical composition of the feedstock (Hill *et al.* 1996; Martínez-Escandell *et al.* 1999). For example, increasing the aromaticity of the feed, increased the dependency of solid and liquid yields on pressure, while reduced the role of temperature and reaction time. It is generally accepted that mesophase formation, an intermediate leading to coke formation (Wiehe 1993), increased upon increasing aromaticity of the feedstock (Martínez-Escandell *et al.* 1999). Chemical interactions between the asphaltenes and the solvent medium; including the ability to transfer hydrogen dominantly, affected coke formation (Rahmani *et al.* 2002). Higher molecular weight fractions and higher asphaltenes content in a given feed contributed to higher coke yield under thermal cracking conditions (Gray 1994).

Low cracking temperature results in low liquid yield, while a too high temperature leads to unstable liquid product due to sediment deposition of more active intermediates (Le Page *et al.* 1992). Too high cracking temperatures promote higher coke and gas yields as a result of increasing reaction rates for coke formation (Pilviol & Vilhunen 1998). Several researchers concluded that longer thermal cracking residence time and temperature increase coke formation (Del Bianco, Panariti, Anelli, *et al.* 1993; Ebrahimi *et al.* 2008; Yue *et al.* 2004), while reducing the viscosity

of the liquid fraction (Al Darouich *et al.* 2006; Bello *et al.* 2006; Shen *et al.* 2008). Finally, thermal cracking at lower operating temperature than typically applied in industry (455°C-540°C) (Speight 2013) with the objective of improving the fluidity of bitumen led to a viscosity reduction (Wang *et al.* 2014).

The effect of pressure on thermal cracking of heavy oil was found to be minimal, secondary to temperature, and depends on the operating temperature and pressure (Hill *et al.* 1996). Nevertheless, it was found that coke yield can be manipulated through controlling the reactor pressure during thermal cracking. Studies on thermal cracking of different kinds of oil at temperatures between 350°C-480°C showed that at higher operating temperature radical decomposition is quite rapid and leads to a wide range of smaller molecular weight species. However, increasing the pressure at high operating temperature, solid yield increased by virtue of increased asphaltene precipitation tendency at the lower specific volume of the oil phase (Wiehe 1993; Hill *et al.* 1996). At low operating temperature, on the other hand, the high activation energy for decomposition reactions inhibited these reactions. As the pressure was increased at low temperatures, the rate of the radical recombination reactions increased and more stable material was produced, which led to a decrease in solid formation until relatively high pressure (Hill *et al.* 1996; Martínez-Escandell *et al.* 1999). Previous work from our group comparing closed and open reactor system arrangement showed that higher liquid product viscosity and lower °API gravity was obtained under the open system arrangement and a higher fraction of lighter material was achieved under closed system arrangement. In the open system arrangement allowing the volatile products to leave the reaction media resulted in reduction of the secondary reaction for lighter hydrocarbon and increased the concentration of the pseudo phase which is responsible for coke formation (Alkhalidi & Jarallah 2013).

In the current study, we investigate the influence of the asphaltenes content of the feedstock, pressure, stirring, temperature and residence time on the thermal cracking of Athabasca vacuum residue (AVR) and Athabasca bitumen (AB) and their maltene fraction in a closed reactor system. Despite the abundance of literature on thermal cracking of heavy oil, very few authors have in fact employed a closed reactor arrangement, while many used semi-batch reactor allowing gases to vent during the reaction. Moreover, this study considers Athabasca VR and bitumen and their maltene extracts and takes into account energy consumption during thermal cracking to better capture the impact of feedstock on the extent of the endothermic reactions. Parameters such as the yield of the different fractions and °API gravity and viscosity of the liquid product were used to characterize the effect of a given variable.

### 3.3 Experimental procedures

#### 3.3.1 Materials

Thermal cracking experiments were conducted on Athabasca vacuum residue (AVR), following fines removal (Nhieu *et al.* 2016), and its maltene extract (AVRM). In addition, some of the experiments used Athabasca bitumen (AB) and its maltene extract (ABM). Parent Athabasca VR contains  $3.6\pm 3.4$  wt% fines,  $29.5\pm 3.2$  wt% asphaltenes and  $63.9\pm 4.9$  wt% maltene. However, fines were removed prior to the experiments, in order to avoid possible catalytic cracking. Table 3.1 lists the major properties of the different feedstocks employed in this work. 95% confidence interval were added to the results based on the three replicate measurements.

**Table 3.1:** Properties of the different feedstocks employed in this work.

Oil sample	°API at 24°C	Viscosity at 37°C (cP)	Asphaltenes (wt%)	Maltene (wt%)
Athabasca VR (AVR)	4.4±1.1	>200,000	31.6±3.2	68.4±4.9
Maltene from Athabasca VR (AVRM)	8.4±1.5	>200,000	0	100

Oil sample	$^{\circ}\text{API}$ at 24°C	Viscosity at 37°C (cP)	Asphaltenes (wt%)	Maltene (wt%)
Athabasca bitumen (AB)	13.1±0.8	35,145±225	15.9±1.9	84.1±1.2
Maltene from Athabasca bitumen (ABM)	17.2±1.3	20,395±320	0	100

Toluene (BDH 99.8%, VWR, Canada) and *n*-heptane (BDH technical, VWR, Canada) were used to reject the toluene insolubles (TI) and asphaltenes, respectively, from the oil samples. Nitrogen (Praxair Specialty Gas & Equipment, AB, Canada) was used as inert gas to purge the reactor vessel and buildup the pressure, whenever applicable.

### 3.3.2 Feedstock preparation

The as received oil samples were heated to 190°C in a gravity convection oven (model: DX300, Yamato Scientific America Inc., CA, USA) in order to reduce their viscosity, and mixed using a metallic rod to ensure consistency of the samples. Fines and toluene insolubles were filtered out from the oil samples by precipitation with excess toluene at a volume ratio of 40:1 and filtration using 25 µm VWR filter paper. Asphaltenes were separated from AVR or AB by mixing the oil after evaporating the toluene with *n*-heptane at a volume ratio of 40:1. Precipitated asphaltenes were removed from the solution by filtration on a 25 µm VWR filter paper and washed with *n*-heptane several times. The asphaltenes were dried until no change in mass was recorded. The remainder of the sample, following *n*-heptane evaporation, constituted the maltene feedstock. In order to study the effect of asphaltenes content on thermal cracking, asphaltenes extracted in the previous step were used to prepare a feedstock with different asphaltenes content: 10 wt% of Athabasca VR extracted asphaltenes for experiments involving AVR and 5 wt% Athabasca bitumen extracted asphaltenes for experiments involving AB.

### 3.3.3 Thermal cracking

The thermal cracking experiments were run in a batch mode, where no gases were allowed to escape during heat treatment. For each experiment, 50 mL of the feedstock was loaded into a 100 mL Parr reactor (1.3 inches I.D. and 4.6 inches length, 4590 Micro Bench top Reactor, Parr Instrument Company, IL, USA). The reactor was placed in an electrically heated jacket and connected to a control unit. Before heating the samples, a leak test was performed by pressurizing the reactor with nitrogen. Following the leak test, the reactor pressure was released and the reactor was heated to the desired temperature of 400°C in order to avoid low yield at low temperatures and unstable product at high temperatures (Pilviol & Vilhunen 1998) at 25°C/min temperature ramp. Once the temperature reached 120°C, the reactor was purged with nitrogen to eliminate air while continuously releasing nitrogen from the unit. Following purging, the reactor was sealed. For some of the experiments, nitrogen was allowed to build up in the reactor unit following purging to an initial pressure of 290 psi. The reaction time was considered from the moment the reactor temperature reached 300°C, which is below the 350°C reported as the typical thermal cracking temperature (Singh *et al.* 2004). The difference between the cumulative energy from the moment heating started until the moment the reactor reached 300°C for the different experiments was small and usually less than the experimental errors. Therefore, cumulative energy readings were taken from the moment heating started. The temperature, pressure and accumulative energy readings on the reactor unit were recorded from the control unit every 5 min. At the end of the reaction, heating was stopped and the reactor was immediately quenched by submerging the unit in a water bath, and the final pressure inside the reactor at 24°C was reported. During quenching, the reaction temperature dropped to below the typical cracking temperature of 350°C (Singh *et al.* 2004) in less than 3 minutes. Therefore, thermal cracking during quenching was assumed negligible. Gases were

then vented by slowly opening the gas valve to release the pressure inside the reactor. The mass of the gaseous product was obtained from the difference between the mass of the feedstock and the final product. In order to determine the liquid yields, the product was washed several times with an excess volume of toluene (40:1) to reject the toluene insolubles, followed by the filtration of the toluene suspension using 25  $\mu\text{m}$  VWR filter paper. The filter paper was washed several times with toluene until filtrate appeared colorless. The mass of the solids left on the filter paper was determined and termed as the toluene insolubles (TI). Toluene was evaporated from the filtrate using a rotary evaporator (Model: Hei-Vap value digital HL/G3, Heidolph instruments GmbH & Co. KG, Germany) at 95°C and 2 psi. In the process of evaporating the toluene other volatiles resulting from the thermal cracking process were also lost from the liquid product to the vapor phase. Total loss during evaporation of the solvent is in fact a component of the liquid product. Equation (E3.1) below shows how this fraction was calculated:

$$\begin{aligned} \text{Total Loss } wt\%_{AVR} = 100 \text{ } wt\%_{AVR} - TI \text{ } wt\%_{AVR} - \text{Asphaltenes } wt\%_{AVR} - \\ \text{Maltene } wt\%_{AVR} \end{aligned} \quad (\text{E3.1})$$

Yields calculated based on the parent Athabasca VR (PAVR) were obtained from E3.2 to E3.4 below.

$$TI \text{ } wt\%_{PAVR} = TI \text{ } wt\%_{AVR} \times a \quad (\text{E3.2})$$

$$Maltene \text{ } wt\%_{PAVR} = Maltene \text{ } wt\%_{AVR} \times a \quad (\text{E3.3})$$

$$Asphaltenes \text{ } wt\%_{PAVR} = Asphaltenes \text{ } wt\%_{AVR} \times a + b \quad (\text{E3.4})$$

where  $a = 1, 0.76,$  and  $0.68$  and  $b = 0, 24,$  and  $31.6$  for feed containing 31.6, 10, and 0 wt% asphaltenes, respectively. The maltene constituent of the product oil was determined by adding  $n$ -

heptane at volume ratio of 40:1 to the upgraded sample to reject the asphaltenes, followed by *n*-heptane evaporation. The *n*-heptane-oil suspension was filtered using 25 µm VWR filter paper. The residue on the filter paper was washed with *n*-heptane until the solution appeared colorless, then dried for 12 h at 25°C to determine the mass of the asphaltenes product. The maltene product was obtained following the evaporation of *n*-heptane using rotary evaporator at the above temperature and pressure, a process which also led to the loss of the lighter upgrading product.

The viscosity of the product oil and its maltene extract was measured at 37°C using a Brookfield digital viscometer (Model: LV DV-1 PRIME, Brookfield Engineering Laboratories Inc., MA, USA) equipped with a water bath to control the temperature. The °API gravity was measured at room temperature using a specific gravity bottle (Thomas Scientific, NJ, USA). In addition, AVR feed and its best upgraded sample in term of quality and quantity of the liquid product were analyzed using a high-temperature simulated distillation (HTSD) which was performed on Aglient GC (ON, Canada) following ASTM D7169-2005 standard procedure. The product gases were analyzed using gas chromatography (Model: Varian-3900 GC, Varian Inc., USA). A gas sample was taken at the end of the reaction time before quenching the reactor in cold water. The gas sampling tube was connected to the reactor and, together with the connection line, was wrapped in a heating tape to prevent any condensation of gases. Thermogravimetry (TG) and differential scanning calorimetry (DSC) were performed on a simultaneous thermal analyzer (Model: STA 6000, PerkinElmer Inc., AB, Canada). Two TI samples from the upgraded crude at 400°C and 420°C of 10 mg were first heated up to 30°C followed by a 1 min isothermal step. Then, the samples were heated up to 800°C at 15°C/min ramp in a 30 mL/min air atmosphere.

Schematic representations summarizing the experimental procedures and the experimental variables are given in Figures 3.1 and 3.2, respectively. Three replicates were prepared for some of the samples and the 95% confidence intervals were added to the results.

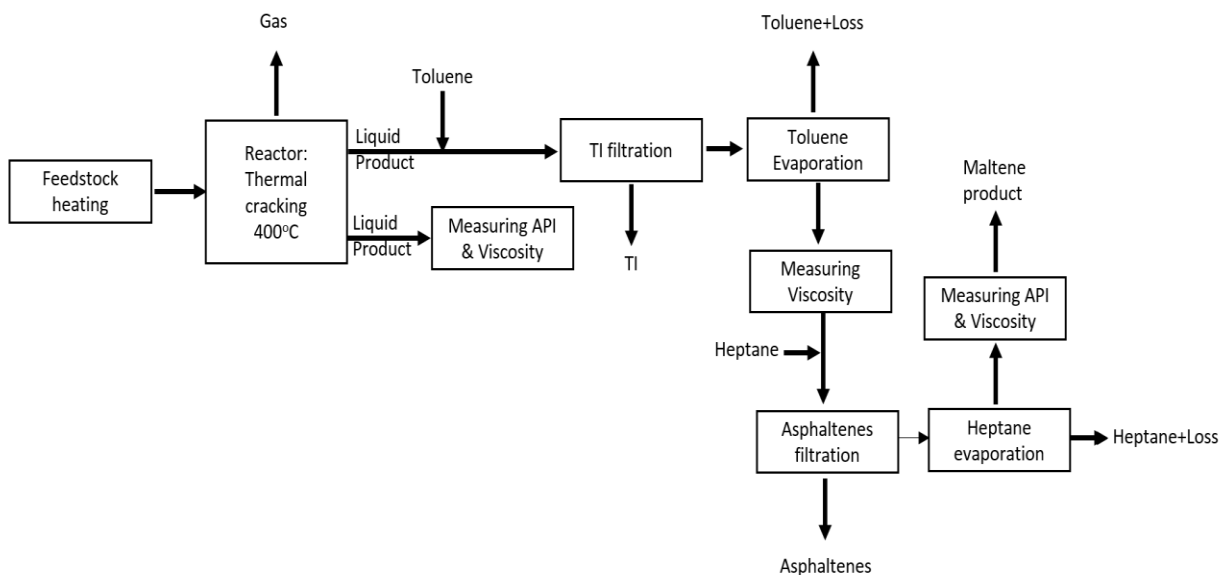


**Figure 3.1:** Schematic representation of the experimental procedures involved in this work.

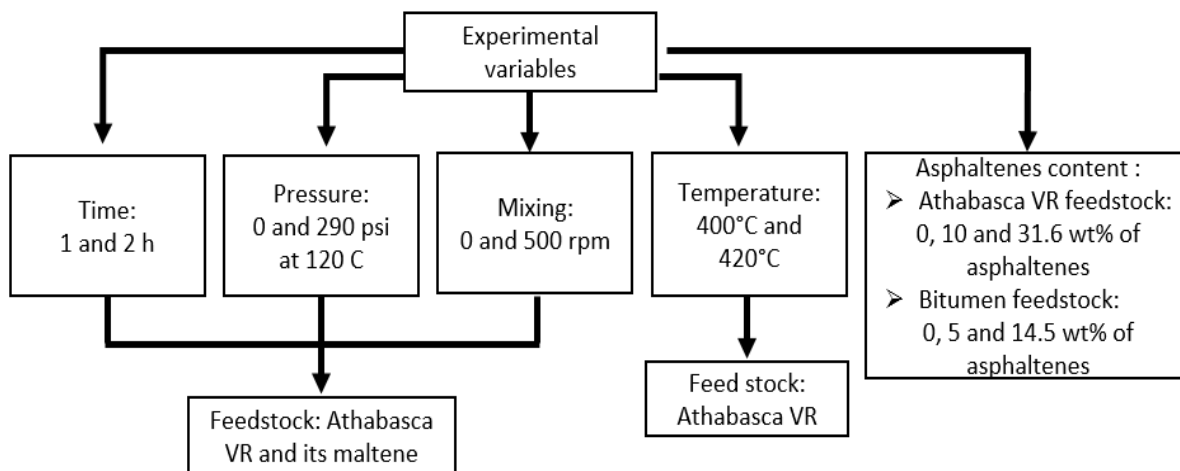


**Figure 3.2:** Block diagram illustrating the experimental variables and condition.

### **3.4 Results and discussion**

Calculations pertaining to energy balance on the reactor system with three major heat sinks; namely the sensible heat of the reactor and its content, the heat loss, and the endothermic heat of reaction/evaporation of reaction products, confirmed that reliable estimates of the endothermic heat of reaction/evaporation of the reaction products can be obtained from the current reactor setup. These estimates were much larger than the experimental error encountered in this study. Detailed conservative estimates are provided in the supporting material. It should be noted that very few literature reports, in fact, attempted estimating the heat of cracking reactions and cracked material vaporization (Gray 2015; Raseev 2003) as a function of molar ratio of hydrogen and carbon in the feed (Agroskin *et al.* 1978).

#### **3.4.1 Effect of reaction time**

Generally, longer thermal cracking times reduce the viscosity of the liquid product (Al-Soufi *et al.* 1988; Bello *et al.* 2006; Shen *et al.* 2008; Shu & Venkatesan 2013) while increasing the gas and the coke yields. These trends approach an asymptotic value at higher reaction time (Zhao *et al.* 2001; Gray *et al.* 2004; Yue *et al.* 2004; Ebrahimi *et al.* 2008; Asgharzadeh Shishavan *et al.* 2011). Over time, asphaltenes concentration increases at first and then decreases at the end of the coke induction period (Ebrahimi *et al.* 2008).

Two residence times were studied in this work, 60 min and 120 min, which are appropriate for thermal cracking of vacuum residues at the chosen experimental temperature based on the quality and quantity of the liquid product. It should be noted that the effect of residence time is less significant at lower temperatures (Bello *et al.* 2006; Wiehe 1993). The total energy input to maintain the reactor at 400°C and the final pressure after cooling for the thermal cracking of Athabasca VR (AVR) and its maltene fraction (AVRM) are given in Table 3.2.

**Table 3.2:** The total energy input to the reactor and the final pressure after cooling for the thermal cracking of Athabasca VR (AVR) and its maltene extract (AVRM) at 400°C.

<b>Feed stock</b>	<b>Reaction time (min)</b>	<b>Cumulative energy (kWh)</b>	<b>Final pressure after cooling (psi)</b>
AVR	60	0.45±0.01	162±8
	120	0.66	212
<b>Feed stock</b>	<b>Reaction time (min)</b>	<b>Cumulative energy (kWh)</b>	<b>Final pressure after cooling (psi)</b>
AVRM	60	0.46±0.01	130±5
	120	0.70	142

Table 3.2 shows that there is no significant difference between the total energy consumption for the thermal cracking of AVR and the thermal cracking of AVRM, which suggests that reactions involving asphaltenes do not contribute to significant endothermic trends. The pressure and the energy consumption variation during reaction are given in Figure 3.3. The energy consumption increases sharply at the beginning and once the temperature reached 350°C it tended to a lower but constant slope. Such a trend is in part due to the controller action and the prescribed temperature program. Nevertheless, it shows that since the start of the cracking reactions, i.e. 350°C, a constant supply of energy is needed to maintain the reactor at 400°C suggesting the same extent of endothermic reactions persists over the duration of the reaction independent of the asphaltenes content of the feedstock. Pressure buildup increased during the reaction and approached an asymptotic value. A constant extent of endothermic reactions and a decrease in gas evolution suggest that more condensation and dehydrogenation reactions occur over time, which cause the content of polycondensed aromatic compounds to increase in the cracked residua and make them relatively resistant to decomposition (Asgharzadeh Shishavan *et al.* 2011). It is

interesting to note that the trend in energy consumption and the pressure buildup with time correlate very well for the two feedstocks.

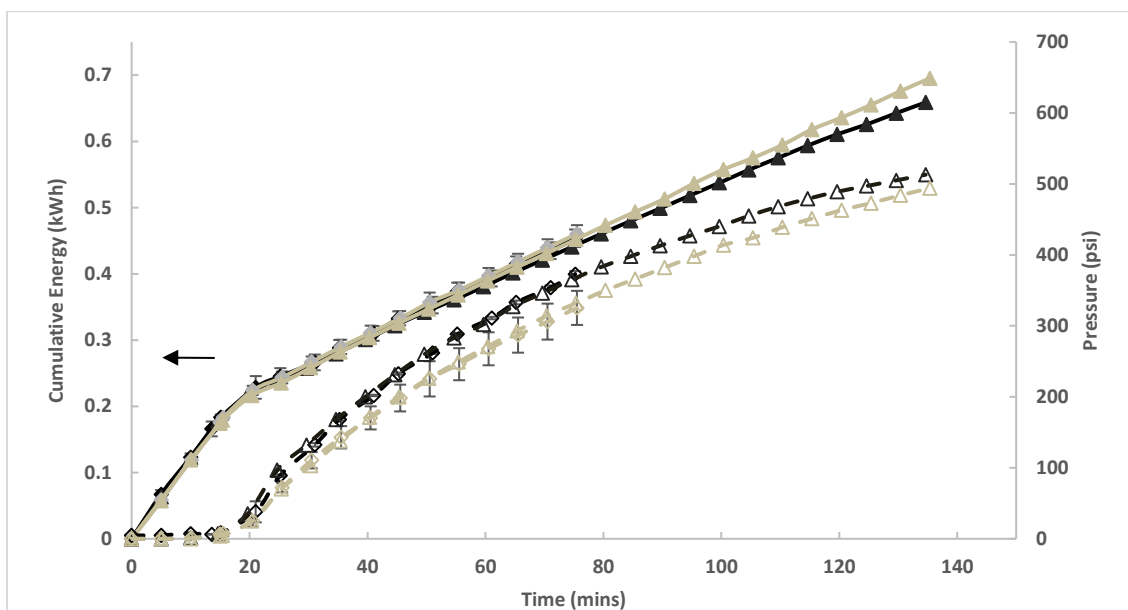


**Figure 3.3:** Energy consumption and pressure buildup inside the batch reactor during the thermal cracking at 400°C of (◆,◇) AVR for 1 h, (▲,△) AVR for 2 h, (◆,◇) AVR for 1 h, and (▲,△) AVR for 2 h.

The final pressure inside the reactor after cooling is higher for the two-hour experiments and the experiments involving AVR. Since the amount of gas produced directly correlates to the amount of coke (Gray 1994), this suggests greater coke content in the experiments with the two-hour residence time and/or with AVR. It should be noted that higher reactivity of the mesophase is encountered in the presence of asphaltenes (Martínez-Escandell *et al.* 1999) due to the lower content of hydrogen donor molecules in presence of higher content of asphaltenes in the reaction media (Torregrosa-Rodríguez *et al.* 2000; Marsh *et al.* 1999).

As depicted in Figure 3.4(A,B), with increasing residence time less asphaltenes and maltene are generated, while the TI, i.e. coke content, and the gas fraction increase. For a given feedstock, on the other hand, it is evident that the coke content increased by  $9.4 \pm 0.2$  wt% and

2.5±0.2 wt% using AVR and AVRМ feed stocks, respectively, with time at the expense of the asphaltic fraction. Yields calculated based on the parent Athabasca VR, shown in Figure 3.4(B), confirm that the overall maltene yield is lower, 14±0.5 wt% for the 1 h experiments and 14.5±0.5 wt% for the 2 h experiments, and the overall asphaltenes content is higher, 15.4±0.8 wt% for the 1 h experiments and 23.2±0.6 wt% for the 2 h experiments, for the thermal cracking of the AVRМ feedstock versus AVR. This result is very important in light of some practices that encourage deasphalting the crude prior to thermal cracking.

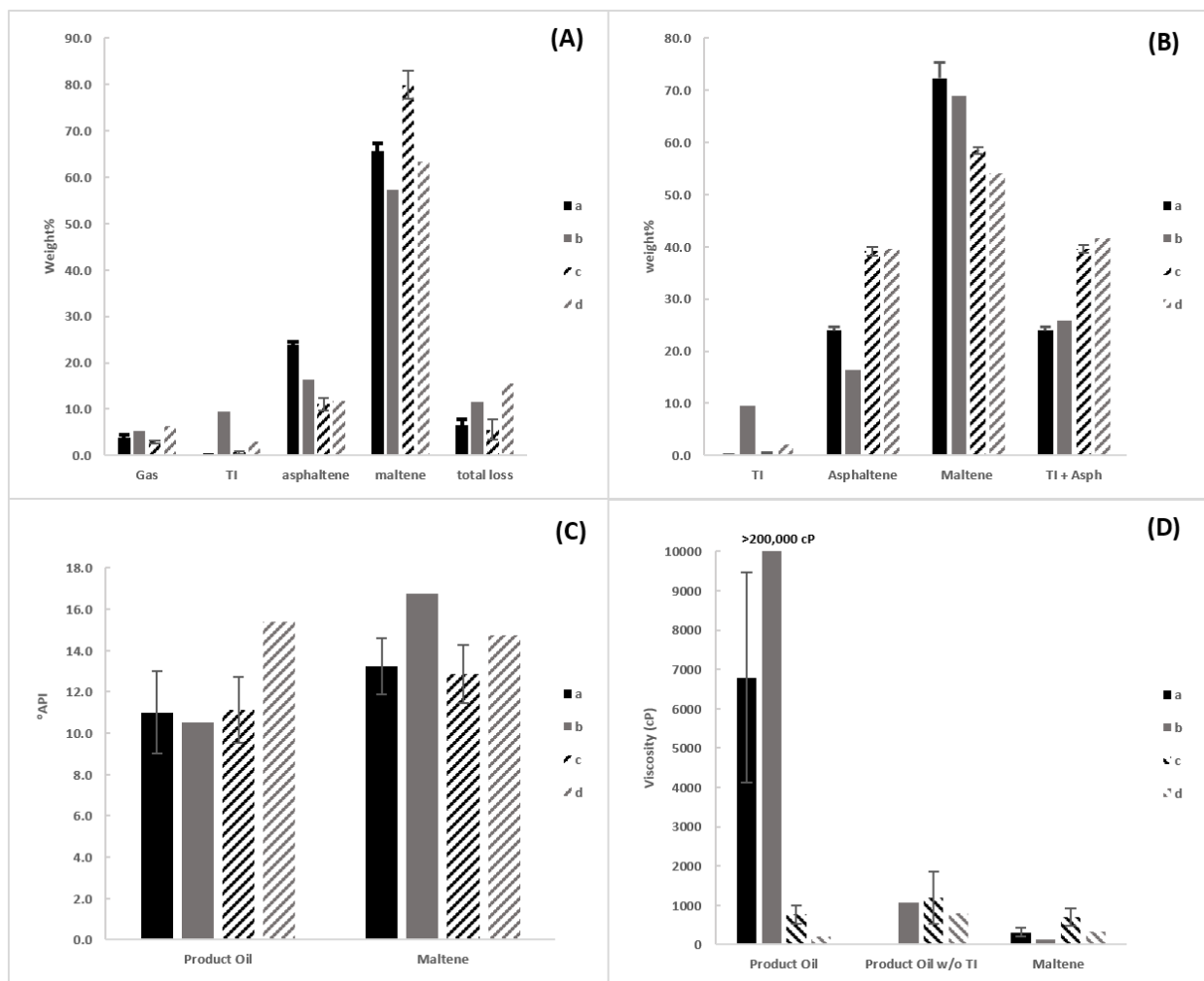


**Figure 3.4:** Product yield based on the AVR or AVR feedstock (A), and product yield based on the parent Athabasca VR (B). °API gravity of the product oil and its maltene extract (C). Viscosity at 37°C of the product oil, the product oil w/o TI and its maltene extract (D) for thermal cracking at 400°C of (a) AVR for 1 h, (b) AVR for 2 h, (c) AVR for 1 h, and (d) AVR for 2 h.

The liquid product viscosity at 37°C and °API gravity at 24°C following the thermal cracking experiments are depicted in Figure 3.4(C,D). In terms of °API gravity, there is no difference between the °API of the product oil after thermal cracking of AVR for 1 h and 2 h experiments. Moreover, there is no significant difference in the °API gravity of the product oil between the experiments involving AVR and AVR for 1 h and any difference falls within the experimental error. For the experiments involving AVR feedstock, a 2 h residence time

increased the °API of the product oil increased from 10.5 to 15.4 probably due to higher extent of cracking reactions, as evident from the larger fraction of TI and the losses associated with the evaporation of lighter fractions as evident from Figure 3.4(A).

The viscosity of the product maltene decreased for the two feedstocks, AVR and AVR<sub>M</sub>, with time and the maltene extract had lower viscosity than the liquid product. These observations are consistent with previous works with different feedstocks (Bello *et al.* 2006; Del Bianco, Panariti, Anelli, *et al.* 1993; Ebrahimi *et al.* 2008; Yue *et al.* 2004). Moreover, following TI rejection and evaporating the associated toluene, the viscosity decreased significantly for the two feedstocks. It appears that the decrease in the viscosity of the product oil following TI rejection overshadows any increase in viscosity arising from evaporating lighter products during toluene evaporation. The viscosity of the product maltene for 1 and 2 h experiments were higher for the experiments involving AVR<sub>M</sub>.

To summarize, the effect of thermal cracking residence time depended on the presence of asphaltenes in the feedstock and increasing residence time increased the TI yield at the expense of the asphaltenes fraction. Moreover, having more asphaltenes in the feedstock did not increase the energy requirement of the thermal cracking reactions.

### **3.4.2 Effect of pressure**

Product yield of pressurized thermal cracking under N<sub>2</sub> atmosphere is compared to a control experiment without pressurizing in Figure 3.5(A,B). Pressurizing the reactor during the thermal cracking of AVR contributed to a 7.4±2.2 wt% reduction in the asphaltenes and a 6.2±1.9 wt% increase in the content of TI. This trend can be explained in light of the increased tendency of asphaltenes precipitation at higher pressure as the specific volume of the oil decreases (Wiehe 1993; Hill *et al.* 1996). On the other hand, for the thermal cracking of the AVR<sub>M</sub>, pressurizing the

reactor did not seem to affect the product yield. This observation is inline with the above explanation involving asphaltenes tendency to precipitate. Energy consumption for AVR shown in Table s3.2 of the supporting material is the same with or without pressurizing. On the other hand, energy consumption for the thermal cracking of AVR with pressurizing is more than AVR without pressurizing, which suggest endothermic reactions of more condensed material at higher pressure.

When analyzing the product yield base on the parent Athabasca VR as captured by Figure 3.5(B), the total asphaltenes yield for the experiments involving the AVR feedstock are  $22\pm 2$  wt% and  $15\pm 1$  wt% higher than the AVR feedstock for the experiments with and without pressurizing, respectively. In addition, although pressurizing the reactor led to a reduction in asphaltenes and an increase in the coke content for the experiments involving AVR, the overall coke, i.e. TI, and asphaltenes content was the same, which suggests faster asphaltenes conversion kinetics into coke than the kinetics of asphaltenes formation reactions.

There is negligible difference in terms of °API gravity and the viscosity of the product oil and the maltene product at the pressures employed in this experiment as per Figure 3.5(C,D). Therefore, it can be concluded that, at the conditions of the current experiments, pressurizing the reactor is not advantageous, regardless of the feedstock.

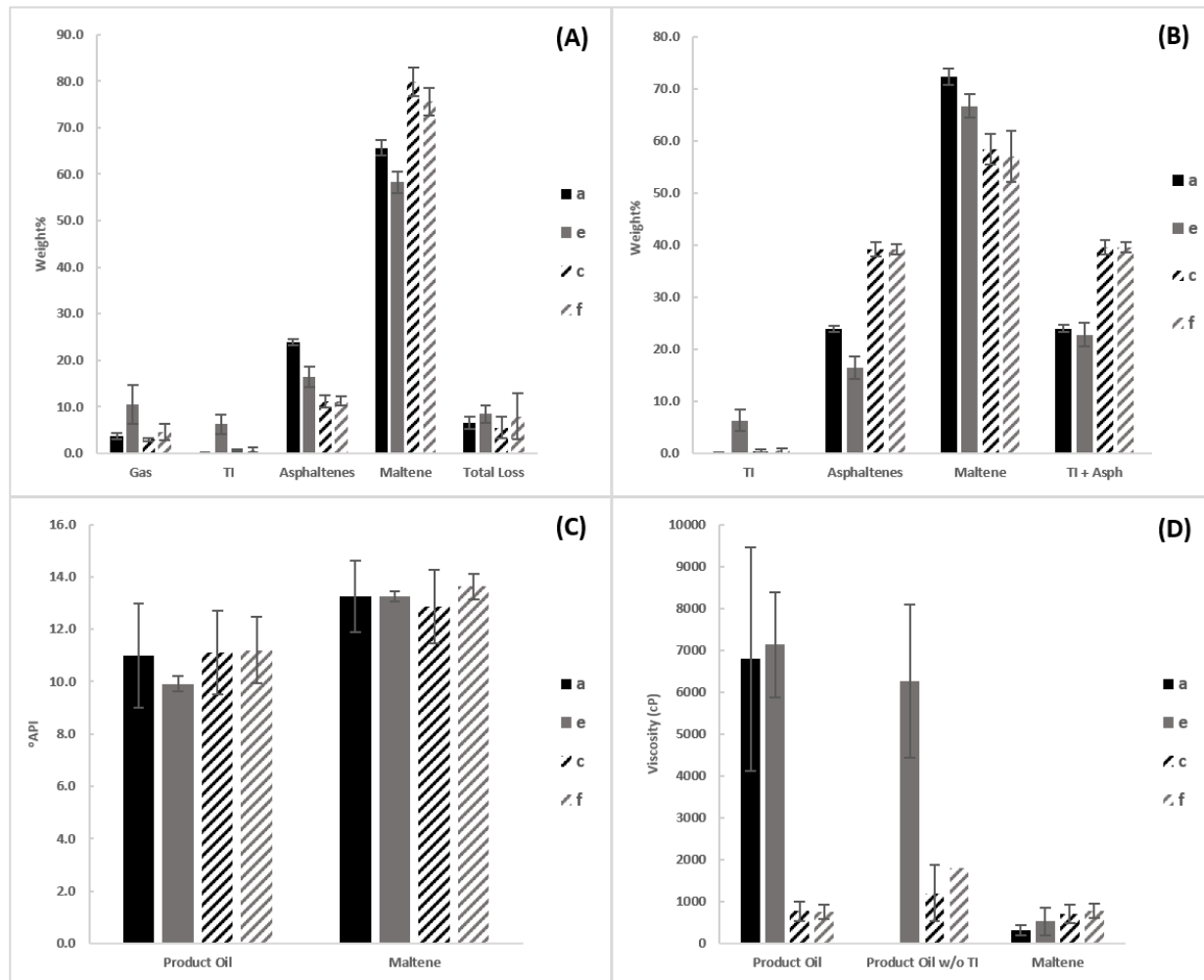


**Figure 3.5:** Product yield, based on the AVR or AVR feedstock (A), and product yield based on the parent Athabasca VR (B). °API gravity of the product oil and its maltene extract (C). Viscosity at 37°C of the product oil, the product oil w/o TI and its maltene extract (D) for the thermal cracking at 400°C of (a) AVR, (e) AVR, pressurized to 350 psi, (c) AVR, and (f) AVR, pressurized to 350 psi.

### 3.4.3 Effect of stirring

In order to explore possible role for mass and/or heat transfer, mixing at 500 rpm was provided in this experiments.

The cumulative energy and the final pressure after cooling are shown in Table s3.2. The product yield and the quality of the liquid product are depicted in Figure 3.6(A-D). For the AVR and AVR feedstock, mixing at 500 rpm did not significantly change the total energy input to the

reactor. On the other hand, the pressure buildup for the AVR feedstock decreased with mixing as shown in Figure s3.6 of the supporting material. Nevertheless, the final pressure after cooling did not change significantly. This suggests that more volatiles are generated in absence of mixing. Product yield in Figure 3.6(A) confirms an increase in coke formation, up to  $4.8 \pm 0.1$  wt%, when mixing the AVR feedstock. The above observations suggest that the polymerization reactions of free radicals are mass transfer limited and became more pronounced with mixing. Subsequently, less volatiles and more coke formed upon mixing, which in turn, led to  $2 \pm 1$  lower °API gravity and  $3.2 \times 10^3 \pm 4.9 \times 10^3$  cP higher viscosity. For the AVR feedstock, on the other hand, much less free radicals formed in absence of asphaltenes.

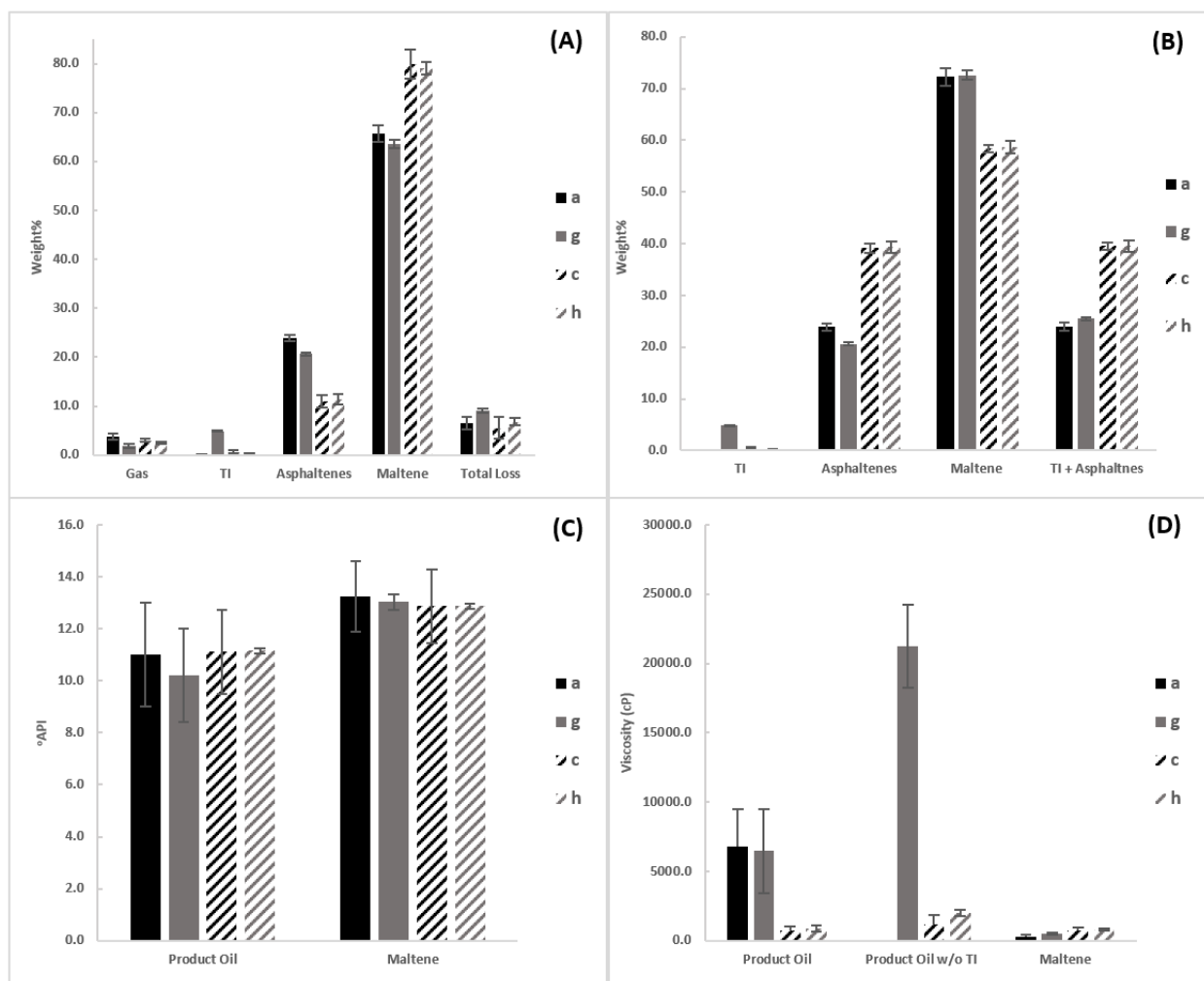


**Figure 3.6:** Product yield based on the AVR or AVRМ feedstock (A), and product yield based on the parent Athabasca VR (B). °API gravity of the product oil and its maltene extract (C). Viscosity at 37°C of the product oil, the product oil w/o TI and its maltene extract (D) for the thermal cracking at 400°C of (a) AVR, (g) AVR with mixing at 500 rpm after the reactor reached 300°C, (c) AVRМ and (h) AVRМ with mixing at 500 rpm after the reactor reached 300°C.

### 3.4.4 Effect of temperature

Generally, higher thermal cracking temperature reduces the viscosity of the liquid product (Al Darouich *et al.* 2006; Bello *et al.* 2006; Shen *et al.* 2008), while increasing the coke and the gas fractions (Pilviol & Vilhunen 1998). In order to explore the effect of temperature, thermal cracking at 420°C was compared to cracking at 400°C. In order to ensure homogeneity of the liquid phase, due to the higher potential of coke formation, mixing at 500 rpm was provided.

The pressure and the energy consumption during the reaction are given in Figure s3.7. At 420°C, Table s3.2 shows 9.1±2.0% increase in energy consumption and 132±13% higher pressure buildup probably due to higher thermal cracking rates. The product yield and the quality of the liquid product are depicted in Figure 3.7(A-D). Increasing the thermal cracking temperature from 400°C to 420°C result in a 3.1±0.3 wt% and 14.9±0.9 wt% reduction in the asphaltenes and maltene products, respectively, and a 10.1±1.4 wt% increase in the content of TI as a result of increased rates of coke formation. Therefore, the increase in TI content comes at the expense of the asphaltene and the maltene fractions, which may suggest faster rates of asphaltenes conversion to coke, but also faster rates of maltene conversion to asphaltenes. On the other hand, the viscosity of the product maltene decreased by 89.5% to  $5.17 \times 10^2 \pm 0.2 \times 10^2$  cP and the °API gravity increased by 41.5% to 18.4±0.9 which is consistent with previous work employing different feedstocks (Al Darouich *et al.* 2006; Bello *et al.* 2006; Shen *et al.* 2008). This suggests formation of more short chain hydrocarbons probably as a result of higher rates of scission reactions. This conclusion is in

harmony with higher rates of asphaltenes formation quoted above where the aromatic radicals resulting from the scission reactions probably contribute to more asphaltenes.

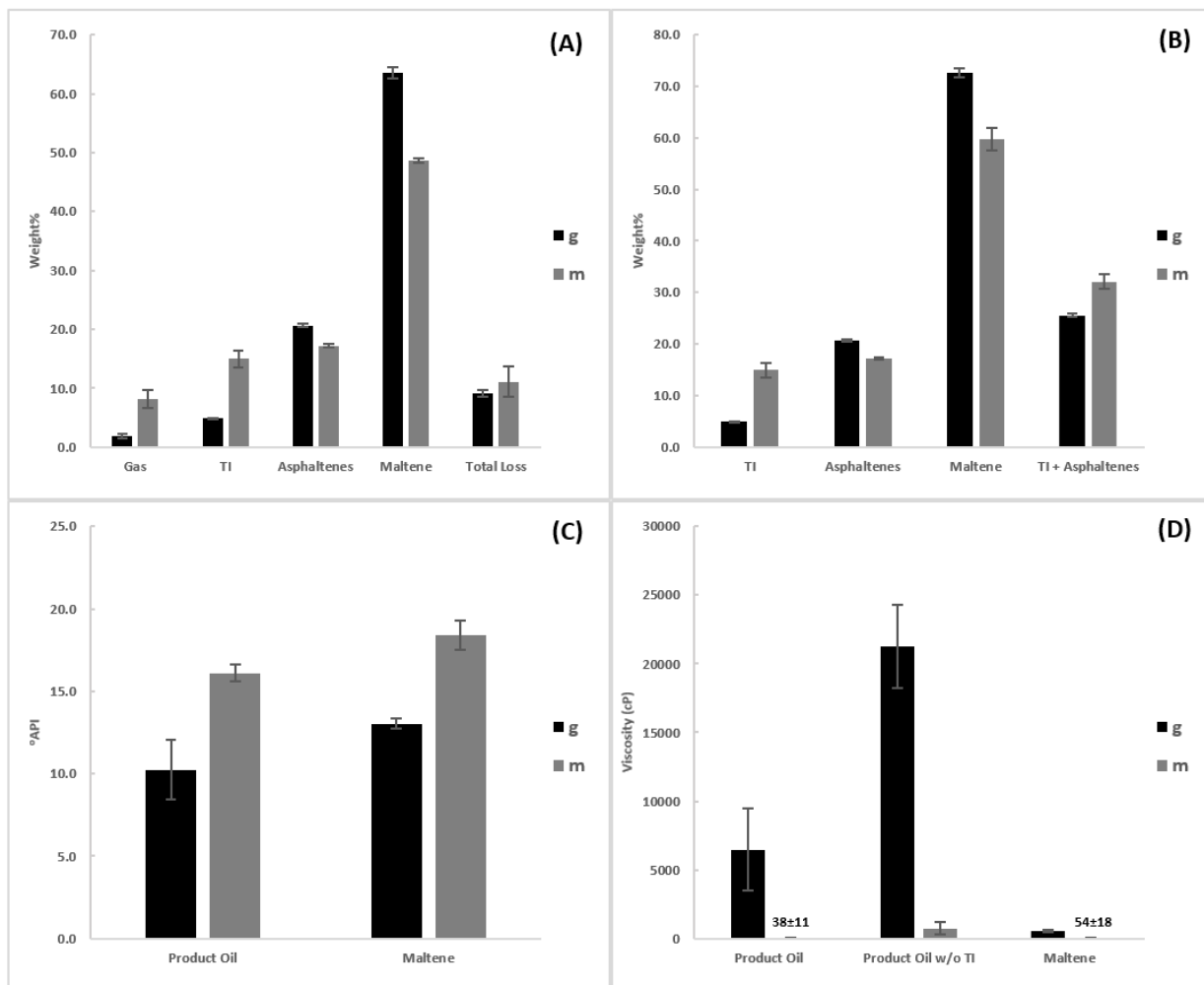


**Figure 3.7:** Product yield based on the AVR feedstock (A), and product yield based on the parent Athabasca VR (B). °API gravity of the product oil and its maltene extract (C). Viscosity at 37°C of the product oil, the product oil w/o TI and its maltene extract (D) for the thermal cracking at (g) 400°C and (m) 420°C

### 3.4.5 Effect of asphaltenes content

From literature findings and the results obtained thus far, it is evident that asphaltenes content of the feedstock significantly affects the thermal cracking of AVR. In this experiment we studied the effect of the asphaltenes content by controlling the mass of asphaltenes added to the maltene

extract of the feedstock. Thermal cracking of AVR was compared to thermal cracking of AVR<sub>M</sub> and AVR<sub>M</sub> containing 10 wt% added asphaltenes. In order to better capture the trends, thermal cracking of Athabasca bitumen, AB, was compared to the thermal cracking of its maltene extract, AB<sub>M</sub>, and AB<sub>M</sub> containing 5 wt% of added asphaltenes.

The final pressure after cooling and the cumulative energy are shown in Table s3.2. Increasing asphaltenes content of the feedstock did not introduce significant changes in the total energy input to the reactor. In addition, and inline with our previous observations, the pressure buildup decreased when removing asphaltenes from the feedstock as shown in Figure s3.8.

From the yield based on the feedstock shown in Figure 3.8(A), increasing the asphaltenes portion of the feedstock leads to more asphaltenes and less maltene product for all the different feedstocks. On the other hand, the total asphaltenes content decreased for the AVR feedstock, relative to its initial value, after thermal cracking at 400°C. Following thermal cracking of AVR, the product oil consists of 23.9±0.6 wt% of asphaltenes and 72.3±1.6 wt% maltene, whereas the original composition of the parent AVR, w/o TI, was 31.6 wt% asphaltenes, which suggests conversion of asphaltenes to other products, e.g. TI and volatiles. For AVR<sub>M</sub> containing 10 wt% and 0 wt% asphaltenes (AVR<sub>M</sub>), there is 5.5±3.5 wt% and 11.1±1.3 wt% increase in asphaltenes content after thermal cracking. It is evident that removing the asphaltenes from the feedstock shifts the reactions to produce more asphaltenes. From an overall yield based on the parent Athabasca VR shown in Figure 3.8(B), there is a declining trend relating the initial asphaltenes content in the feedstock and the overall asphaltenes yield after the thermal cracking process, since, again, removing the asphaltenes from the feedstock shifts the reactions to produce more asphaltenes. Moreover, there is negligible difference in °API gravity of the maltene product irrespective of the

asphaltenes content, while the viscosity of the maltene product at 37°C was lower for the AVR feedstock.

Results for the experiments involving AB with different asphaltenes content, 0 wt% (ABM), ABM containing 5 wt% asphaltenes and 15.9 wt% (AB), are shown in Figure 3.9(A,B). For the feedstocks containing 5 wt% and 0 wt% asphaltenes, there is  $6.3 \pm 2.8$  wt% and  $8.3 \pm 2.1$  wt% increase in asphaltenes content after thermal cracking. From an overall yield based on the parent AB shown in Figure 3.9(B), there is a declining trend relating the initial asphaltenes content in the feedstock and the overall asphaltenes yield after the thermal cracking process. Figure 3.9 and Table 3.2 confirm an increase in the final pressure after cooling and the pressure buildup during thermal cracking with increasing asphaltenes content in the feedstock. The trend pertaining to the asphaltenes content in the feedstock and the product asphaltenes correlate well for the AVR and the AB feedstocks.

From the yield of asphaltenes product for experiments with AVR an AB, it is obvious that there is a specific value for the asphaltenes content in the feedstock below which reactions shift to producing more asphaltenes. On the other hand, higher amount of asphaltenes leads to conversion of asphaltenes to other products, e.g. TI and volatiles. This asphaltenes content value for AVR feedstock is between 10-30 wt% and for AB feedstock should be around 15 wt% as shown in Figure 3.10. The declining trend relating the initial asphaltenes content of AVR and AB feedstock and the overall asphaltenes yield after the thermal cracking process is depicted in Figure 3.11. From comparing these key performance parameters, it can be concluded that deasphalting the feedstock leads to an overall lower quality/quantity thermal cracking product. This conclusion, of course, should not be generalized for the catalytic upgrading processes, where asphaltenes may deactivate the catalyst.

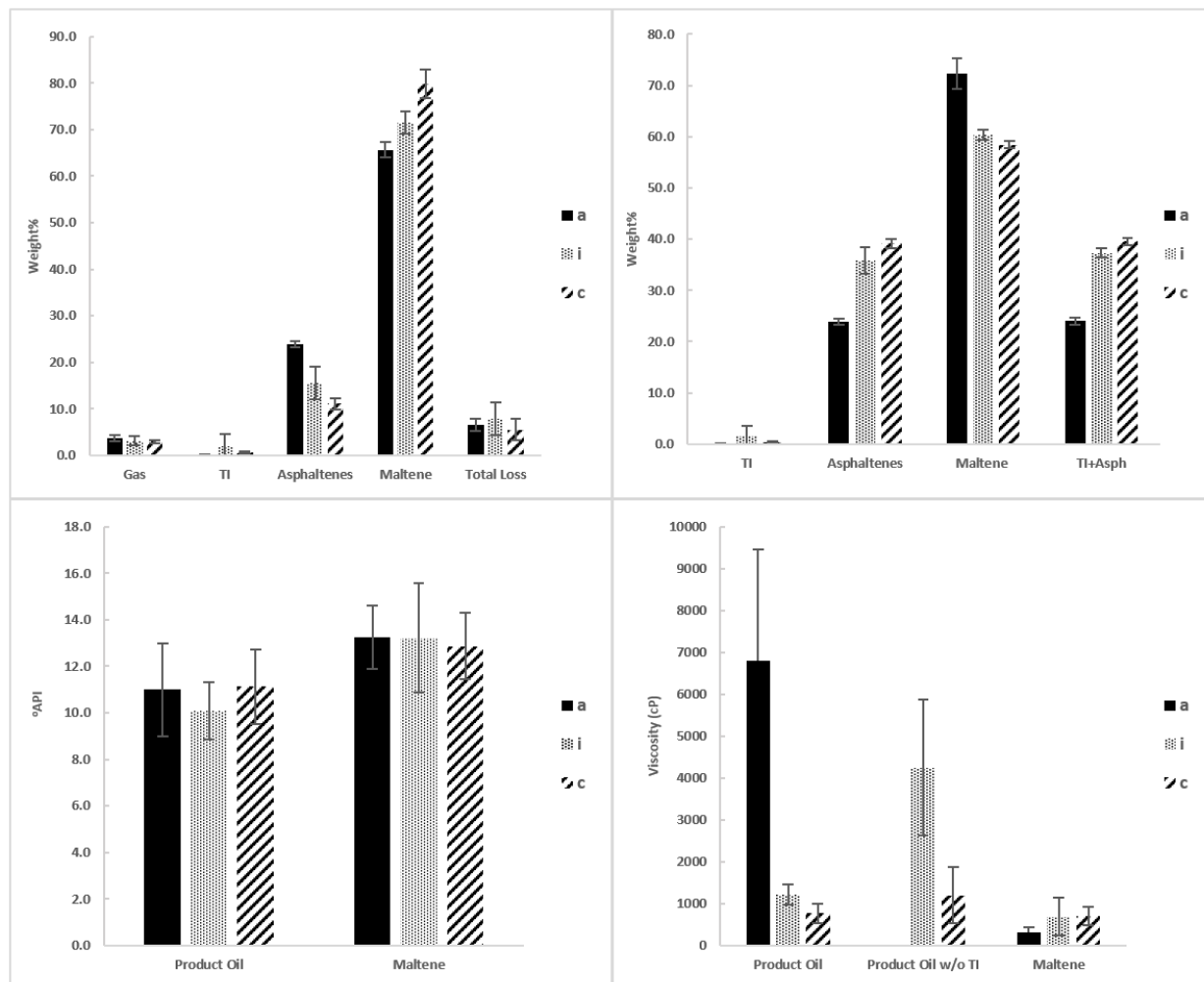


**Figure 3.8:** Product yield based on the AVR or AVR with 10 wt% asphaltene feedstock (A), and product yield based on the parent Athabasca VR, (B). °API gravity of the product oil and its maltene extract (C). Viscosity at 37°C of the product oil, the product oil w/o TI and its maltene extract (D) for 1 h thermal cracking at 400°C of (a) AVR, (i) AVR with the addition of 10 wt% asphaltene, and (c) AVR with 10 wt% maltene.

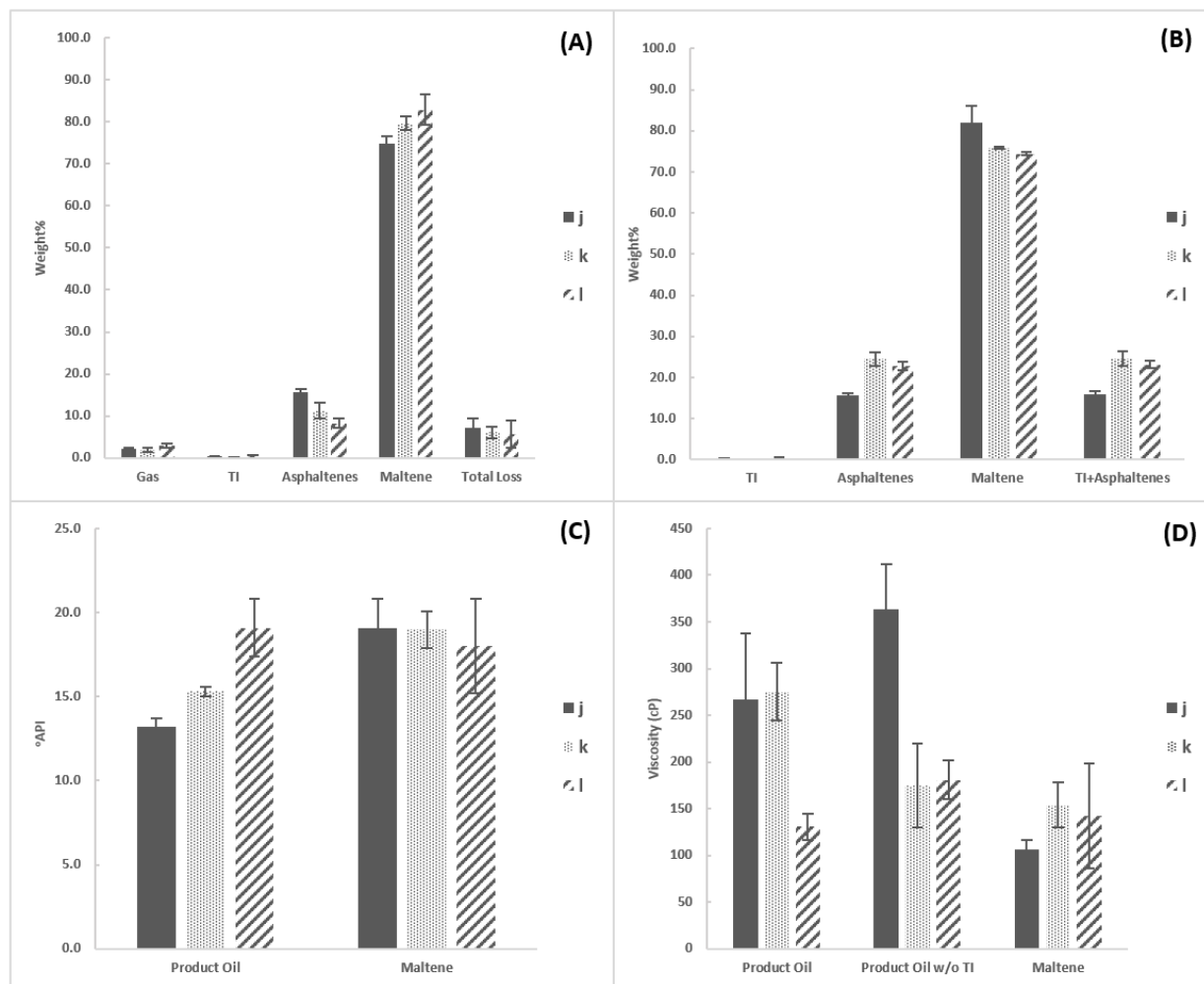


**Figure 3.9:** Product yield based on the AB or ABM feedstock (A), and product yield based on the parent Athabasca bitumen (B). °API gravity of the product oil and its maltene extract (C). Viscosity at 37°C of the product oil, the product oil w/o TI and its maltene extract (D) for the 1 h thermal cracking at 400°C of (j) AB, (k) ABM with 5 wt% added asphaltenes, and (l) ABM.

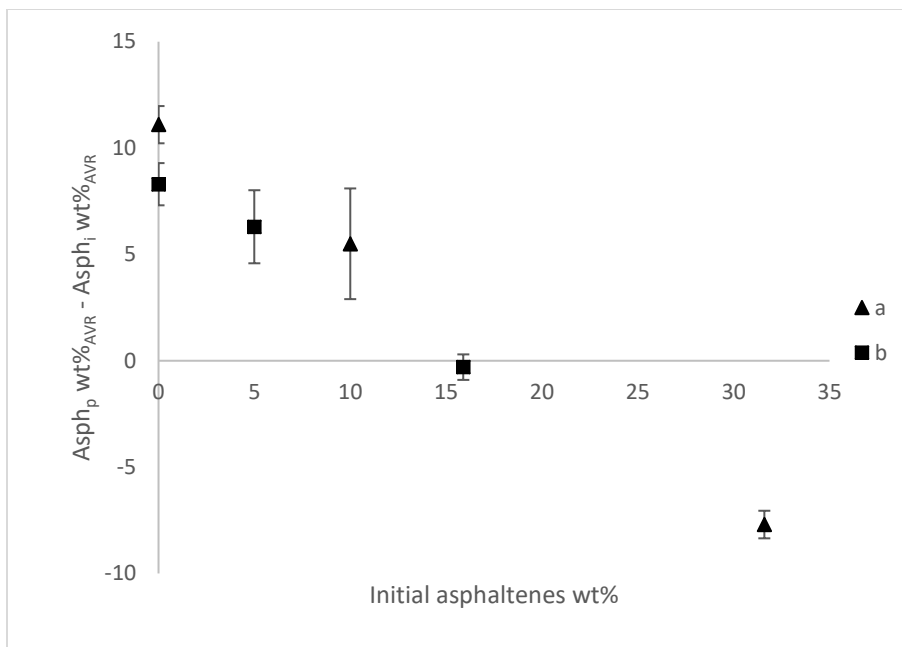


**Figure 3.10:** Difference between initial asphaltenes (Asph<sub>i</sub>) in the feedstock and asphaltenes yield from the thermal cracking (Asph<sub>p</sub>) for thermal cracking of (a) Athabasca VR and (b) Athabasca bitumen at different initial asphaltenes content in the feedstock.

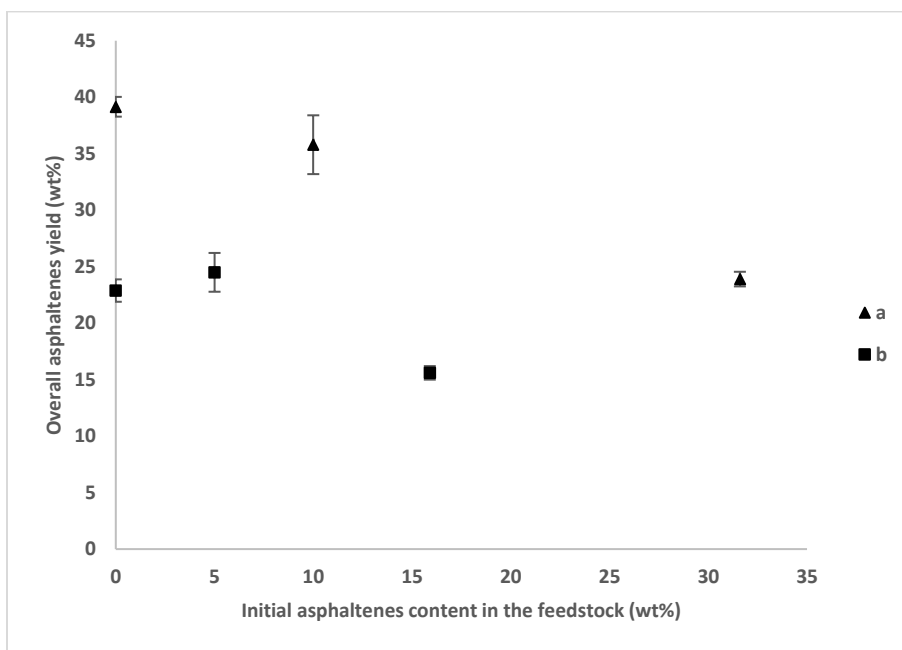


**Figure 3.11:** Overall asphaltenes yield from the thermal cracking of (a) Athabasca VR and (b) Athabasca bitumen at different initial asphaltenes content in the feedstock.

### 3.4.6 SimDist and GC test results

The yield of standard distillation cuts from the thermal cracking products is an essential parameter for economic evaluation of the upgrading process (Carbognani *et al.* 2007). Figure 3.12 presents the comparison of the simulated distillation curves between the AVR feed and the product oil of the thermal cracking of AVR at 400°C and 0 rpm mixing for 1 h. The difference in the boiling points between the AVR feed and product oil suggests significant upgrading took place. The common cut point as a dividing line between light distillates and residual component is n-C44 boiling point (545°C). Figure 3.12 shows that the upgraded sample contain an average of 30% lighter fractions ( $T_{b.p.} < 545^{\circ}\text{C}$ ) compared with the original feed.

The conversion of the 545<sup>+</sup>°C, the residue, for the product oil from thermal cracking at 400°C for 1 h, was obtained using the E3.5:

$$Conv_{545^{+}C} = \frac{Mass\ of\ 545^{+}C_{feed} - Mass\ of\ 545^{+}C_{Product}}{Mass\ of\ 545^{+}C_{feed}} \times 100\% \quad (E3.5)$$

The conversion of residue, 545<sup>+</sup>°C, was 34.5%. This calculation, of course, is only based on the liquid product of the upgraded sample and ignores the conversion to TI and asphaltenes, which again suggests that big picture should always involve calculation of the fraction of all the cuts. Radical cracking is responsible for the conversion of the residue to the lighter fractions, as discussed earlier. Producing lighter fraction will result in an improvement of the quality of the product liquid (Carbognani *et al.* 2007).

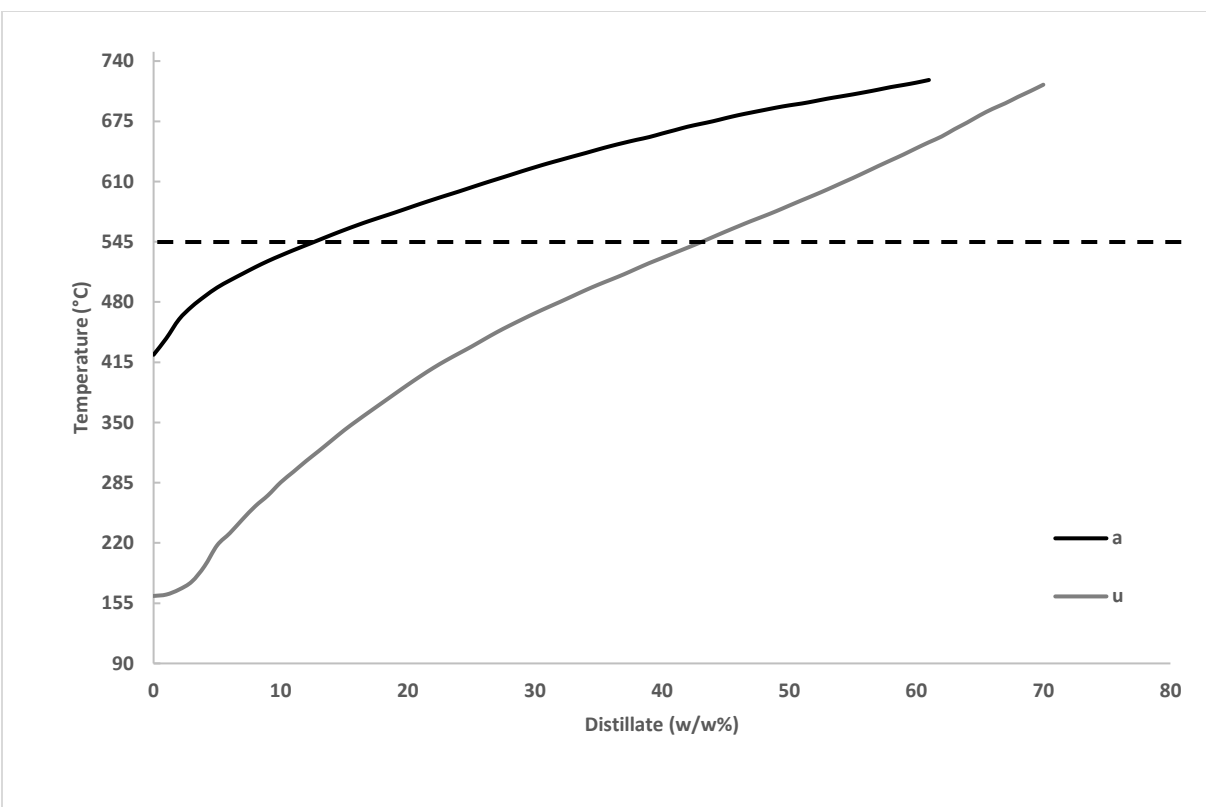


**Figure 3.12:** High-temperature simulated distillation curves of (a) AVR and (u) product oil from thermal cracking of AVR at 400°C and 0 rpm for 1 h.

Analysis of the gaseous product from the thermal cracking of AVR is included in Table 3.3. The analysis shows major contributions from hydrocarbon components ranging C1 to C6 which is expected, since the temperature at which the gases were collected is the upgrading temperature of 400°C. Following quenching the reactor, it is anticipated that the main constituents would be C1, C2 and C3. There are 30.2 wt% condensable gases based on gas sample which should be part of the maltene product. Generally higher average molecular weight of gas products from thermal cracking stems from higher aliphatic nature of the feedstock (Martínez-Escandell *et al.* 1999).

**Table 3.3:** Analysis of gaseous products collected at 400°C for the thermal cracking of AVR at 400°C and 0 rpm for 1 h.

Gas	Wt%	MW	Mol%
C1	15.64	16.04	36.58
C2	18.82	30.07	23.48
C3	18.39	44.1	15.64
i-C4	5.82	58.1	3.76
n-C4	11.14	58.1	7.19
C5	11.24	72.2	5.84
C6	9.31	86.2	4.05
C7	6.21	100.2	2.32
C8	3.43	114.2	1.13

### 3.4.7 DSC/DTG test results

Figure 3.13 compares the mass loss and the heat flow results for TI products of thermal cracking at 400°C and 420°C. The change in slope of the mass loss curves indicate more than one oxidation stage for the TI products for the two thermal cracking temperatures. In addition, the reaction zones had shifted to the left for the TI product of thermal cracking at 420°C, which suggests more reactive TI. This trend will be further explored and results will be communicated shortly.

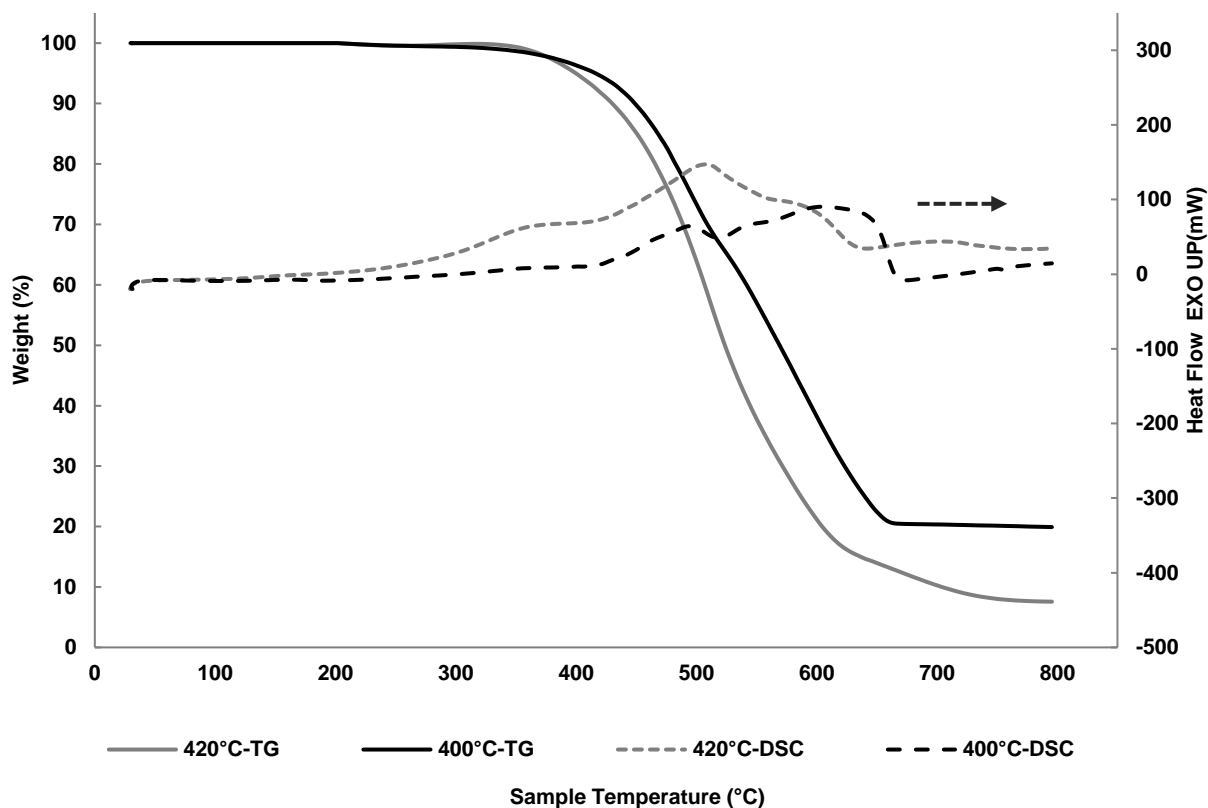


**Figure 3.13:** TG and DSC curves of TI Product for the thermal cracking of AVR at 400°C and 420°C

All of the above observations suggest that during thermal cracking reactions, lighter hydrocarbons were produced, which results in a decrease of asphaltenes solubility in the reaction media (Rahimi & Gentzis 2006). Asphaltenes aromatic core, on the other hand, were exposed by cleavage of side alkyl chains. Cracking of large molecules (Krishna *et al.* 1988) leads to more reactive or unstable products, where they undergo polymerization or combine with one another to produce larger molecules which produces coke (Henderson & Weber 1965). Studied variables has effect on conversion of these reactions and led to formation of more coke (Rahimi & Gentzis 2006).

### 3.5 Conclusions

This paper reports on the effect of reaction time, pressure, mixing and asphaltenes content of the feedstock on the thermal cracking of Athabasca vacuum residue, Athabasca bitumen and their maltene fractions at 400°C in a closed system. Most literature reports, in fact, employed semi-batch reactor arrangement, while terming their process batch operation. The experimental results revealed the following:

1. The effect of reaction time, mixing and reactor pressure on TI yield depended on the asphaltenes content of the feedstock. The higher reactivity of the mesophase and the abundance of free radicals in the presence of asphaltenes led to higher TI yield.
2. The TI yield increased at the expense of the asphaltenic fraction at higher residence time, mixing and higher reactor pressure suggesting faster asphaltenes conversion kinetics into coke than the kinetics of asphaltenes formation reactions.
3. Free radical polymerization reactions are mass transfer limited and became more pronounced with mixing leading to an increase in TI formation and reduction in the °API gravity and an increase in the viscosity of the liquid product.
4. Increasing the asphaltenes content of the feedstock did not introduce significant changes in the total energy input to the reactor suggesting that asphaltenes may not be the main contributors to the endothermic trends. Energy consumption for AVR is the same with or without pressurizing. On the other hand, energy consumption for the thermal cracking of AVR with pressurizing is more than AVR without pressurizing, which suggest endothermic reactions of more condensed material at higher pressure. For the AVR and AVR feedstock, mixing at 500 rpm did not introduce significant changes in the total energy input to the reactor.

5. There is an inverse relationship between the initial asphaltenes content in the feedstock and the overall asphaltenes yield after thermal cracking at the experimental conditions considered in this study. Removing asphaltenes from the feedstock shifts the reactions to produce more asphaltenes. Moreover, viscosity of the maltene product was lower for feedstocks containing asphaltenes compared to feedstock without asphaltenes. This result is very important in light of some practices that encourage deasphalting the crude prior to thermal cracking.

6. TGA/DSC analysis of the TI collected at 400°C and 420°C suggest more reactive TI at higher thermal cracking the temperature. This observation will be further studied and results will be communicated shortly.

### **3.6 Acknowledgment**

The authors would like to thank the Natural Sciences and Engineering Research Council of Canada (NSERC) for the financial support, and Ms. Tong Xu for helping in running part of the experiments.

### 3.7 Supporting material

#### 3.7.1 Supporting material A: Estimating heat losses from the reactor unit

##### Nomenclature:

$Q_{\text{loss}}$ : Energy loss (kWh)

$\dot{Q}_{\text{Loss}}$ : Rate of energy loss  $\frac{kWh}{min}$

$h$ : Natural convection heat transfer coefficient ( $\frac{W}{K.m^2}$ )

$A$ : Total area of heat transfer ( $m^2$ )

$T$ : Temperature reading inside the reactor (K)

$T_s$ : Surface temperature (K)

$T_{\infty}$ : Ambient temperature (K)

$T_f$ : Film temperature (K)

$C_p$ : Specific heat ( $\frac{J}{Kg.K}$ )

$Nu$ : Nusselt number

$Ra$ : Rayleigh number

$Gr$ : Grashoff number

$Pr$ : Prandtl number

$\beta$ : Coefficient of volumetric expansion ( $\frac{1}{K}$ )

$G$ : Gravitational acceleration =  $9.81 \frac{m}{s^2}$

$L_c$ : Characteristic length of cylinder (m)

$K$ : Thermal conductivity ( $\frac{W}{m.k}$ )

$\nu$ : Kinematic viscosity ( $\frac{m^2}{s}$ )

$\Delta E_{in}$ : Energy input (kWh)

$\Delta E_{SR}$ : Sensible heat for the reactor (kWh)

$\Delta E_{SVR}$ : Sensible heat for VR (kWh)

$\Delta E_{SG}$ : Sensible heat for glass beads (kWh)

$\Delta E_{rxn}$ : Energy expended for reactions/evaporation of reaction products (kWh)

### **3.7.1.1 Introduction**

The following analysis is carried out to explore the contribution of the endothermic reactions to the overall energy consumption. If not appreciable, then the similarity in the cumulative energy input to the reactor in presence and absence of asphaltenes reported in this work can be simply attributed to heat losses. If appreciable on the other hand, and given the high reproducibility of the results, one should be able to draw sound conclusions on heat of reaction in presence and absence of asphaltenes.

Overall, the energy input to the reactor during any time interval is expended as sensible heat to increase the temperature of the reactor and its content to the set point, overcome heat losses and provide the energy required for the endothermic cracking reactions. For starters, and given the two distinct slopes of the cumulative energy lines in the regions before and after approaching 400°C, as depicted in Figure s3.1, one concludes that heat loss is not the only major energy sink and at least sensible heat, given the higher slope in *zone I*, also appreciably contributes as a heat sink.

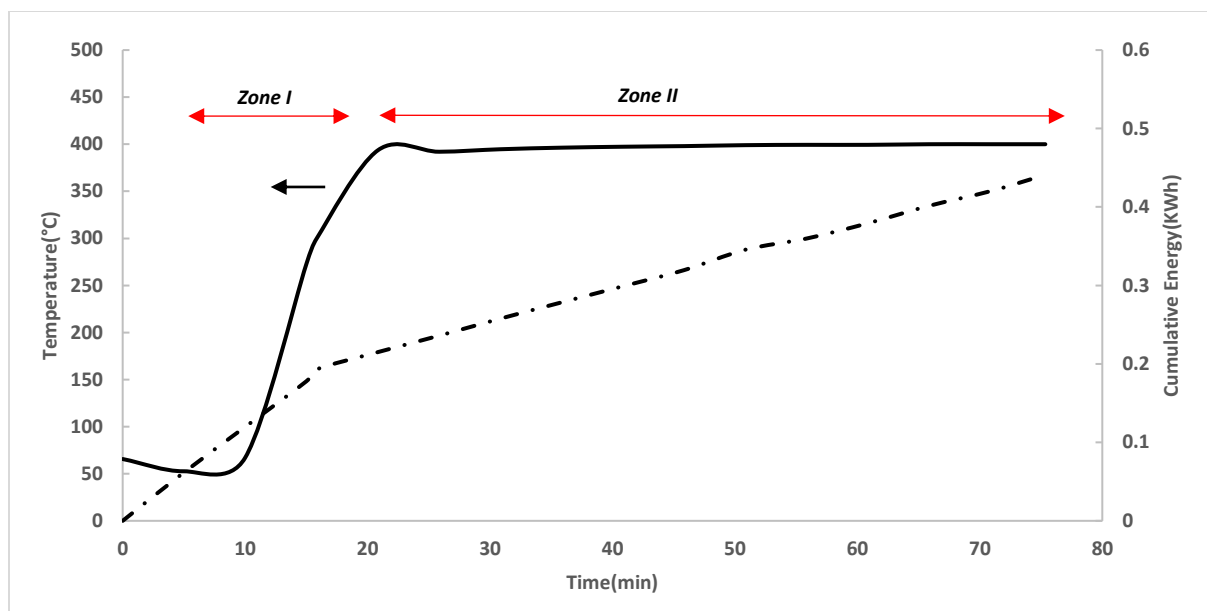


**Figure s3.1:** Temperature variation and cumulative energy input to the reactor for thermal cracking of AVR at 400°C.

In an attempt to exaggerate heat loss calculations and, subsequently, obtain a conservative estimate of the heat of reactions, the energy supplied to the reactor during any time interval within *zone I* of Figure s3.1 is assumed to only equal to heat loss and energy accumulation, which in turn equal the sensible heat of the reactor material and the vacuum residue. The energy expended toward possible endo thermic reactions, especially between 350°C and 400°C, is assumed zero. Beyond 400°C (*zone II* of Figure s3.1), and given the consistency in the reactor temperature reading, energy input to the reactor was assumed equal to the heat loss and the endothermic energy of the cracking reactions. It is constructive to note that the rate of heat loss calculated near 400°C from *zone I* will most likely be constant for the rest of reaction time (*zone II*). But first, and in order to study the heat transfer through the heavy oil feed, since it surrounds the temperature sensor, and whether it is effective or not, a control run for the reactor at the same temperature program was performed with glass beads. Figure s3.2 captures the energy and the temperature profiles for this run. Glass beads are known to have low thermal conductivity (Sakatani *et al.*

2012). Figure s3.2 shows that, the controller was unable to attain the set-point over the course of the run and the temperature kept oscillating with a damping effect, nevertheless. This action of the controller is attributed to the low heat conductivity of the glass beads (Sakatani *et al.* 2012). Consequently, one may conclude that a constant temperature with minor deviation from the set point is reflective of effective heat transfer in the presence of the heavy oil feed.

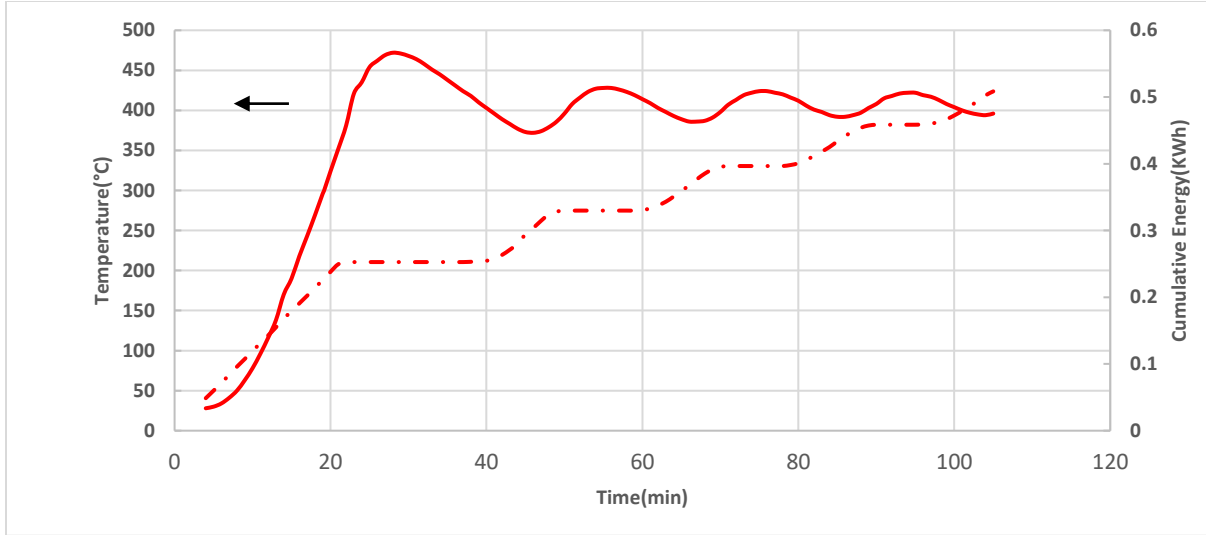


**Figure s3.2:** Temperature variation and cumulative energy input to the reactor for heating the glass material at 400°C.

### 3.7.1.2 Heat loss estimation

#### 3.7.1.2.1 Estimates based on zone I

In *zone I* of Figure s3.1, for any time interval  $\Delta t$  with known  $\Delta T$  and per assumptions stated above, the energy input and the energy accumulation terms are obtained from equations Es3.1 and Es3.2.

$$\Delta E_{in} = Q_{loss} + \Delta E_{accu} \quad (Es3.1)$$

$$\Delta E_{accu} = \Delta E_{SR} + \Delta E_{SVR} \quad (Es3.2)$$

The sensible heat of the reactor material is given by,

$$\Delta E_{SR} = (mC_p \Delta T)_{SVR} = \frac{1239.9g}{1000g/kg} * \left( C_p \Delta T \frac{J}{Kg.K} \right) * \left( 2.78 * 10^{-7} \frac{kWh}{J} \right) \quad (Es3.3)$$

where the  $C_p$  is as a function of temperature is obtained from (Redmond & Lones 1952),

$$\begin{aligned} C_p \Delta T &= 4186.6 * \int_{T_1}^{T_2} (0.109 + 5.7 * 10^{-5} T) dT \\ &= 4186.6 \frac{\frac{J}{kg.K}}{\frac{cal}{g.K}} * (0.109 * \Delta T * \frac{5.7 * 10^{-5}}{2} * (T_2^2 - T_1^2)) \quad (Es3.4) \end{aligned}$$

It should be noted here, and in order to exaggerate heat loss, only the mass of the reactor material contained within the heating mantle is accounted for. Again, this should provide a conservative estimate of the heat of reaction in *zone II*.

Assuming the feed maintains constant composition throughout *zone I*, the sensible heat of VR is calculated from (Shaw *et al.* 2015),

$$\begin{aligned} \Delta E_{SVR} &= (m C_p \Delta T)_{SR} = \left( \frac{50 \text{ g}}{1000 \text{ g}} * \left( 1.48 \frac{J}{g.K} * 1000 \frac{g}{kg} \right) * (\Delta T \text{ K}) * \left( 2.78 * 10^{-7} \frac{kWh}{J} \right) \right) \\ (Es3.5) \end{aligned}$$

For the time interval between 19.57 min and 20.85 min, the temperature rose from 370°C to 393°C, while the total energy input increased from 0.209 kWh to 0.215 kWh. Accordingly, the values for the heat loss and energy accumulation calculated from Es2.1 to Es2.5 are as follows:  $\Delta E_{SR} = 0.0043$  kWh,  $\Delta E_{SVR} = 0.00047$  kWh,  $Q_{loss} = 0.0007$  kWh and the rate of heat loss is

$$\dot{Q}_{Loss} = \frac{0.0007 \text{ kWh}}{(20.85 - 19.57) \text{ min}} = 0.0006 \frac{kWh}{min}$$

Since the temperature was stable in *zone II* at its maximum value; namely 400°C, the energy balance in this zone reduces to

$$\Delta E_{in} = Q_{loss} + \Delta E_{rxn} \quad (Es3.6)$$

If one assumes  $\dot{Q}_{Loss}$  calculated above from *zone I* to be the same throughout *zone II*, then the total heat loss in *zone II* is  $Q_{loss} = \dot{Q}_{Loss} * \Delta t = 0.0006 \frac{kWh}{min} * 54.5 \text{ min} = 0.032 \text{ kWh}$ . Since the

cumulative energy input in this zone is 0.2259 kWh, then per E6,  $\Delta E_{rxn} = 0.2259 - 0.032 = 0.1939$  kWh,  $Q_{loss} / \Delta E_{in} * 100 = 15\%$ ,  
and,  $\Delta E_{rxn} / \Delta E_{in} * 100 = 85\%$ .

From these calculations it is evident shown that the endothermic heat of cracking reactions is a major contributor as a heat sink. Subsequently, the trend in total energy input to the reactor indeed helps drawing reliable conclusions on heat of reactions in presence and absence of asphaltenes.

In the sections below, a method based on convection heat transfer is used to further provide another way estimate of heat loss relative to the total energy input to the reactor.

### **3.7.1.2.2 Estimates based on natural convection**

#### **3.7.1.2.2.1 Convection from the Reactor**

In this section,  $Q_{loss}$  is estimated from natural convection calculation assuming the outer surface of the reactor is exposed to air at 25°C. In principle, this should exaggerate the value for  $Q_{loss}$ , especially since the mantle surrounding the reactor is insulated. The following assumptions were used to facilitate the calculations.

- Uniform surface temperature of the reactor was assumed equal to the temperature reading inside the reactor, since as stated above, the heat transfer through VR appears rapid.
- Ambient temperature is constant at 25°C
- Heat transfer was assumed to take place through natural convection from the surface of the reactor.
- The reactor unit was assumed as a vertical cylinder with dimensions shown in Figure s3.3. These dimensions account for the maximum possible surface area of the reactor; including the lid.

Again, this should exaggerate the value for  $Q_{loss}$ .

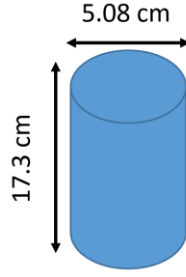


**Figure s3.3:** Schematic representation of the reactor unit.

The rate of heat loss through natural convection can be obtained from Newton's law of cooling.

$$\dot{Q}_{\text{Loss}} = h A (T_s - T_\infty) \quad (\text{Es3.7})$$

The convection heat transfer coefficient can be obtained from Nusslet number as follows (Totala *et al.* 2013),

$$h = \frac{Nu K}{L_c} \quad (\text{Es3.8})$$

where, Nusslet number can be calculated from (Totala *et al.* 2013),

$$Nu = 0.59 (Ra)^{0.25} \quad (\text{Es3.9})$$

where,

$$Ra = Gr Pr \quad (\text{Es3.10})$$

and,

$$Gr = \beta g L_c^3 \frac{\Delta T}{\nu^2} \quad 10^4 < Ra < 10^9 \quad (\text{Es3.11})$$

where,

$$\beta = \frac{1}{T_f} \quad (\text{Es3.12})$$

and

$$T_f = \frac{(25+273)+(400+273)}{2} = 485.5 \text{ K},$$

Accordingly,

$$\beta = \frac{1}{485.5} = 2.06 * 10^{-3} \frac{1}{K},$$

Substituting for  $g = 9.81 \frac{m}{s^2}$ ,  $L_c = 0.173 m$ ,  $\Delta T = (400 - 25) = 375 K$ ,

$Pr$  (for air @ 485.5 K) = 0.685 (Dixon 2007),  $\nu$  (for air @ 485.5 K) =  $34.63 * 10^{-6} \frac{m^2}{s}$  (Dixon 2007) and  $K$  (for air @ 485.5 K) =  $0.038 \frac{W}{m.k}$  (Dixon 2007), gives

$Gr = 2.06 * 10^{-3} \frac{1}{K} * 9.81 \frac{m}{s^2} * (0.173 m)^3 * \frac{375 K}{\left(34.63 * 10^{-6} \frac{m^2}{s}\right)^2} = 3.3 * 10^7$

$$Gr = 2.06 * 10^{-3} \frac{1}{K} * 9.81 \frac{m}{s^2} * (0.173 m)^3 * \frac{375 K}{\left(34.63 * 10^{-6} \frac{m^2}{s}\right)^2} = 3.3 * 10^7$$

$$Ra = Gr Pr = 3.3 * 10^7 * 0.685 = 2.2 * 10^7$$

$$Nu = 0.59 (Ra)^{0.25} = 0.59 (2.2 * 10^7)^{0.25} = 40.6$$

$$h = \frac{Nu K}{L_c} = \frac{40.6 * 0.038 \frac{W}{m.k}}{0.173 m} = 9.1 \frac{W}{K.m^2}$$

$$\dot{Q}_{Loss} = h A \Delta T = 9.1 \frac{W}{K.m^2} * (0.0296 m^2) * (375 K) = 101.6 W$$

$$\dot{Q}_{Loss} = 101.6 W = 0.101 \frac{kJ}{s} * \frac{60 s}{1 min} * \frac{0.00027 kWh}{1 kJ} = 0.0016 \frac{kWh}{min}$$

$\Delta E_{rxn}$  is obtained from Es3.6

$$Q_{loss} = 0.0016 \frac{kWh}{min} * 54.5 min = 0.09 kWh$$

$$\Delta E_{rxn} = 0.2259 - 0.09 = 0.136 kWh$$

$$Q_{loss} / \Delta E_{in} * 100 = 40\%$$

$$\Delta E_{rxn} / \Delta E_{in} * 100 = 60\%$$

$Q_{loss}$  and  $\Delta E_{rxn}$  relative to the total energy input to the reactor confirm the appreciable contribution of the endothermic reaction as an energy sink and the reliability of conclusions on endothermicity drawn from the cumulative energy input to the reactor.

### 3.7.1.2.2.2 Convection from the mantle

In this section,  $Q_{\text{loss}}$  is estimated from natural convection calculation assuming the outer surface of the mantle is exposed to air at 25°C. The following assumptions were used to facilitate the calculations.

- Uniform surface temperature of the mantle was assumed equal to the temperature reading inside the reactor, i.e. 400°C, in order to exaggerate the value of  $Q_{\text{loss}}$ .
- Ambient temperature is constant at 25°C.
- Heat transfer was assumed to take place through natural convection from the surface of the mantle.
- The mantle was assumed as a vertical cylinder with dimensions shown in Figure s3.4. These dimensions account for the maximum possible surface area of the mantle.

All of the calculations are the same as previous calculations except the dimensions of the unit depicted in Figure s3.4:

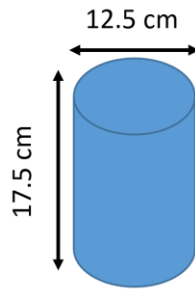


**Figure s3.4:** Schematic representation of the mantle unit.

$$A = 0.06 \text{ m}^2$$

$$L_c = 0.175 \text{ m}$$

$$Gr = 2.06 * 10^{-3} \frac{1}{K} g * 9.81 \frac{m}{s^2} * (0.175 \text{ m})^3 * \frac{375 \text{ K}}{(34.63 * 10^{-6} \frac{m^2}{s})^2} = 3.3 * 10^7$$

$$Ra = Gr Pr = 3.3 * 10^7 * 0.685 = 2.3 * 10^7$$

$$Nu = 0.59 (Ra)^{0.25} = 40.8$$

$$h = 8.8 \frac{W}{K.m^2}$$

$$\dot{Q}_{Loss} = h A \Delta T = 8.8 \frac{W}{K.m^2} * (0.06)m^2 * (375K) = 199 W$$

$$\dot{Q}_{Loss} = 199 W = 0.199 \frac{kJ}{s} * \frac{60 s}{1 min} * \frac{2.7 * 10^{-4} kWh}{1 kJ} = 0.003 \frac{kWh}{min}$$

$\Delta E_{rxn}$  is obtained from Es3.6

$$Q_{loss} = 0.003 \frac{kWh}{min} * 54.5 min = 0.163 kWh$$

$$\Delta E_{rxn} = 0.2259 - 0.163 = 0.062 kWh$$

$$Q_{loss} / \Delta E_{in} * 100 = 72\%$$

$$\Delta E_{rxn} / \Delta E_{in} * 100 = 28\%$$

$Q_{loss}$  and  $\Delta E_{rxn}$  relative to total energy input to the reactor showed large enough contribution, beyond the experimental error, of the endothermic reaction to the total energy consumption. Hence, even at this level of exaggerating the heat loss value, sound conclusions on the contribution of asphaltenes to the endothermic cracking reactions can still be made.

**Table s3.1:** Summary of heat loss based on estimates from *zone I* and natural convection.  $E_{in}(kWh)$  in *zone II* over the 54.5 min time duration = 0.2259 kWh. The difference in  $Q_{loss}$  values is attributed to the different assumptions employed in the calculations

Method	$\dot{Q}_{Loss}$ (kWh/min)	$Q_{loss}$ (kWh) over 54.5 min	Percent: $Q_{loss}(kWh)/E_{in}(kWh)$ %
Estimations based on <i>zone I</i>	0.0006	0.032	15
Convection from reactor	0.0016	0.09	40
Convection from mantle	0.003	0.163	72

### 3.7.2 Supporting material B

**Table s3.2:** The overall energy input to the reactor and the final pressure after cooling for 1 h thermal cracking of different feedstocks at 400°C, natural pressure and 0 rpm, unless otherwise noted.

Feed stock	Cumulative Energy (kWh)	Final Pressure after cooling (psi)
1) Effect of the nature of feedstock		
AVR	0.45±0.01	162±8
AVRM	0.46±0.01	130±5
2) Effect of reactor pressure (initial pressure of 350 psi)		
AVR	0.45±0.03	358±11
AVRM	0.48±0.01	347±3
3) Effect of mixing (mixing at 500 rpm)		
AVR	0.44±0.01	149±10
AVRM	0.46±0.02	136±12
4) Effect of asphaltenes content (mixing at 500 rpm)		
AVR	0.45±0.01	162±8
VRM with 10 wt% asphaltenes	0.45±0.00	144±5
AVRM	0.46±0.01	130±5
AB	0.43±0.01	123±3
ABM with 5 wt% asphaltenes	0.44 ±0.00	119±3
ABM	0.44±0.01	113±1
5) Effect of Temperature (T= 420°C, mixing at 500 rpm)		
AVR	0.48±0.00	346±17

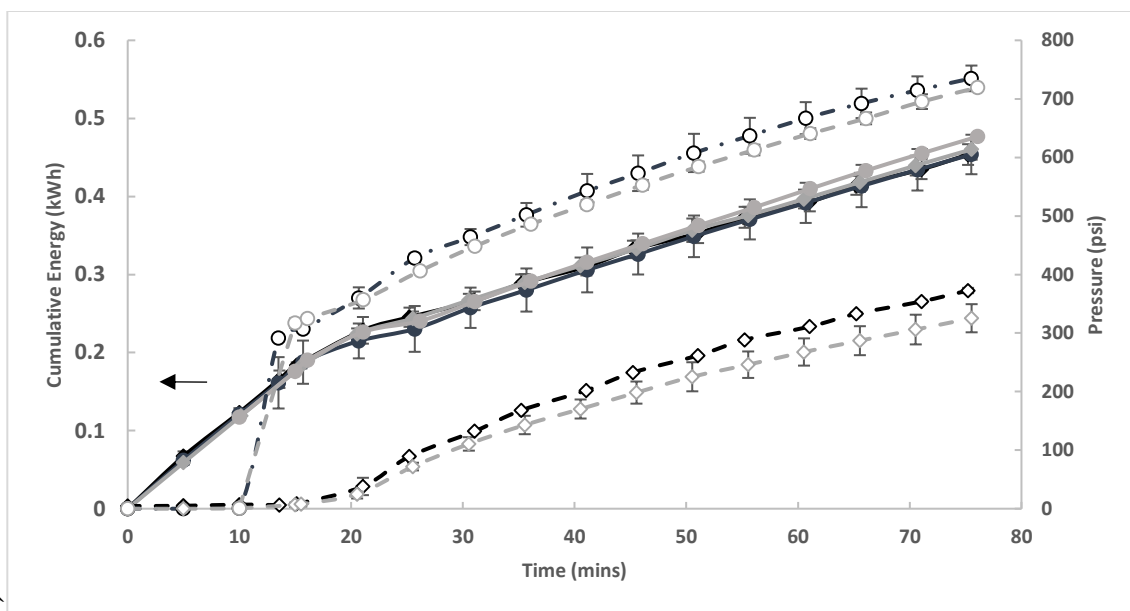


**Figure s3.5:** Energy consumption and pressure buildup inside the batch reactor during the thermal cracking at 400°C and 1 h of (◆,◇) AVR, (●,○) AVR pressurized to 350 psi, (◆,◇) AVR with mixing, and (●,○) AVR with mixing, pressurized to 350 psi.

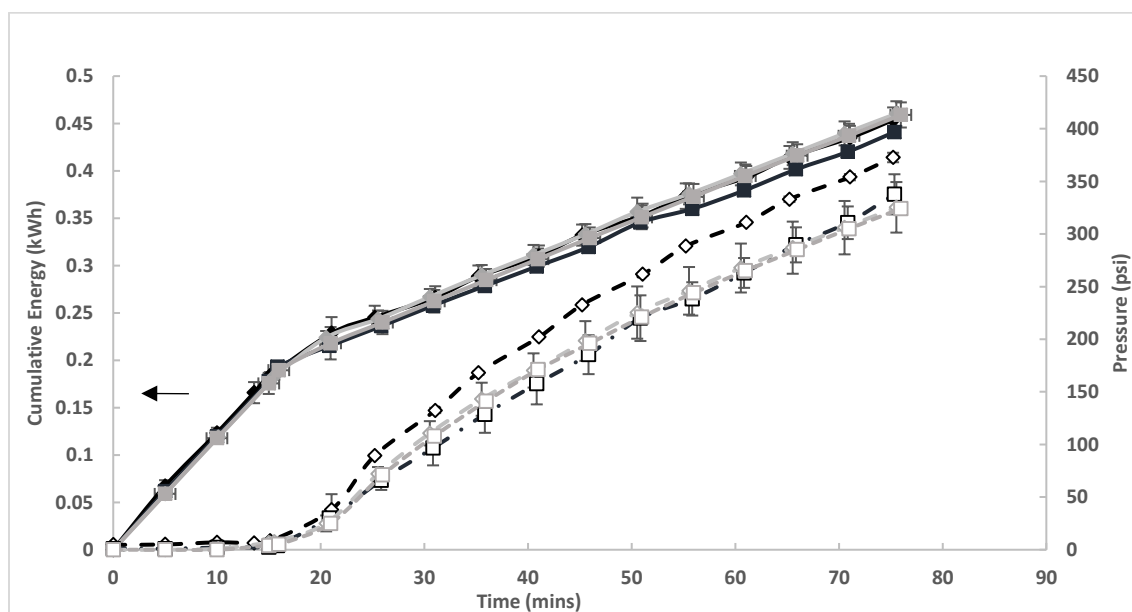


**Figure s3.6:** Energy consumption and pressure buildup inside the batch reactor during the thermal cracking at 400°C for 1 h, of (◆,◇) AVR, (■,□) AVR with mixing at 500 rpm after the reactor reaches 300°C, (◆,◇) AVR with mixing at 500 rpm after the reactor reaches 300°C, and (■,□) AVR with mixing at 500 rpm after the reactor reaches 300°C.

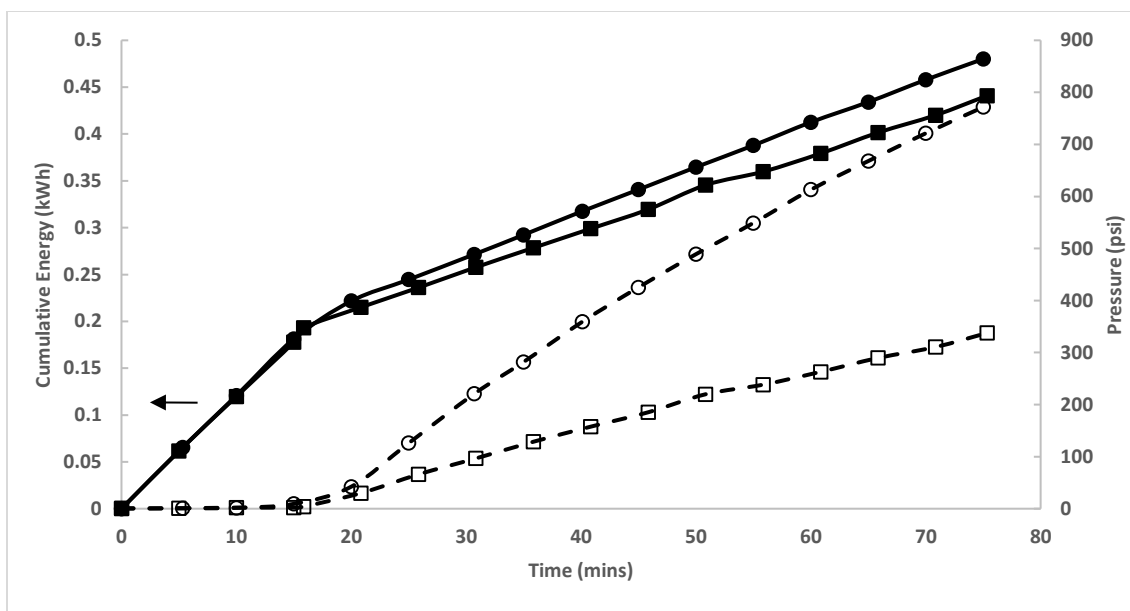


**Figure s3.7:** Energy consumption and pressure buildup inside the batch reactor during the thermal cracking for 1h of AVR at (■,□) 400°C and (●,○) 420°C

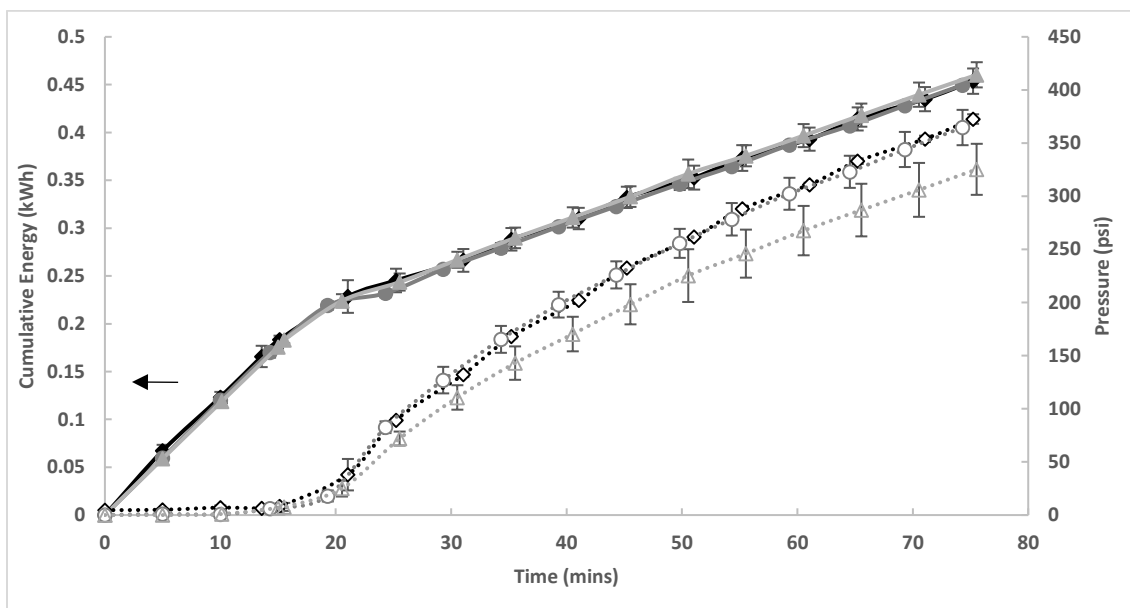


**Figure s3.8:** Energy consumption and pressure buildup inside the batch reactor during the thermal cracking at 400°C for 1 h of (◆,◇) VR, (●,○) AVR with 10 weight% asphaltenes, and (▲,△) AVR

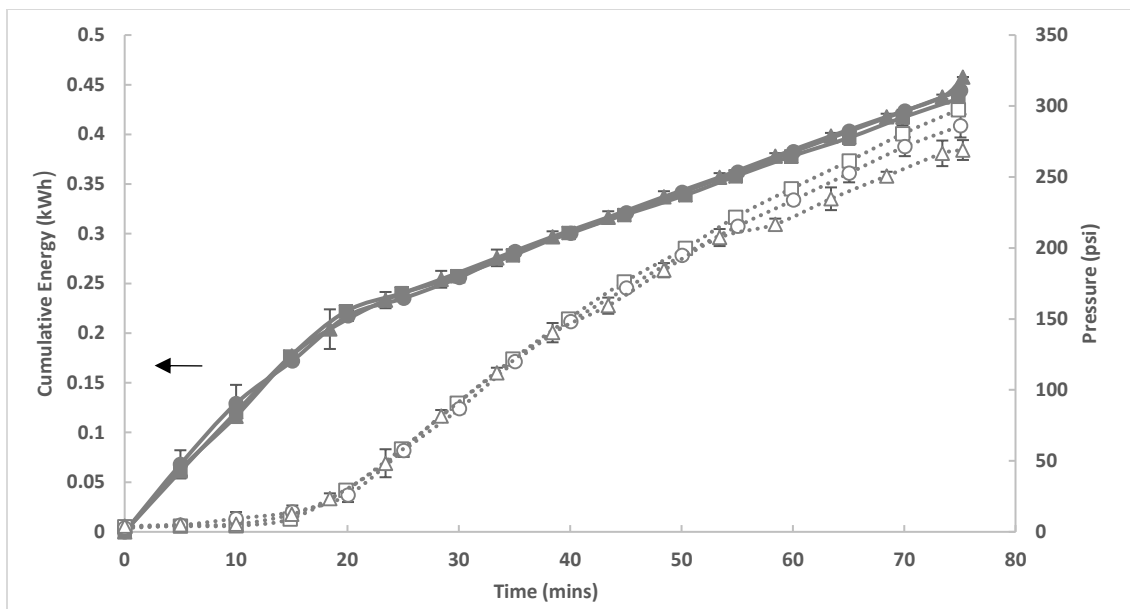


**Figure s3.9:** Energy consumption and pressure buildup inside the batch reactor during the thermal cracking at 400°C for 1 h, of (■,□) AB, (●,○) ABM with 5 wt% asphaltenes, and (▲,△) ABM

## Chapter Four: Catalytic Thermal Cracking of Athabasca VR in a Closed Reactor System

Afroz Eshraghian and Maen M. Husein\*

*Department of Chemical & Petroleum Engineering, University of Calgary, Calgary, AB, Canada T2N 1N4*

### 4.1 Abstract

In this work, catalytic thermal cracking of Athabasca vacuum residue (AVR) at 400 °C was investigated in an autoclave in presence of in situ prepared and commercial alumina nanoparticles (NPs) as well as drill cuttings (DC); a waste product. The properties of the liquid product and its maltene fraction; including °API gravity, viscosity and high-temperature simulated distillation analysis (HTSD), in addition to the yield of the different fractions, the total energy input and the pressure buildup were used to assess the performance of the additives. The results confirmed a catalytic role for the additives and higher liquid yields were observed in this study relative to literature reports. The performance of DC at the highest concentration, 30 wt%, did not yield the highest liquid fraction and matched that of the NPs. The mechanism of coke inhibition could be elucidated from scanning electron microscopy (SEM) photographs coupled with energy-dispersive X-ray spectroscopy (EDX) analysis of the toluene insoluble (TI) fraction. Finally, thermogravimetry and H/C ratio analyses of the TI and asphaltenes confirmed the heavier nature of these products. Optimum product quality and yield was obtained at 10 wt% DC and hence a run at 420 °C was compared.

*Keywords: catalytic cracking, Athabasca, VR, nanoparticles, in situ, drill cuttings*

---

\*Correspondence address: Department of Chemical & Petroleum Engineering, University of Calgary, Calgary, AB, Canada T2N 1N4, Tel: (403) 220-6691; Fax: (403) 282-3945; E-mail: [maen.husein@ucalgary.ca](mailto:maen.husein@ucalgary.ca)

## 4.2 Introduction

Heavy oil is highly viscous with low °API gravity and low economic value, since it is more difficult to transport and process compared with conventional crude (Castañeda et al. 2012). Nonetheless, the increase in world energy consumption draws attention to heavy oil upgrading as a viable approach for meeting the demand on liquid fuels (Kraemer et al. 2009; Vaillancourt et al. 2014; Bian et al. 2008; Kim et al. 2017). Heavy oil upgrading consists of processes aiming at increasing the H/C ratio of the crude by either rejecting part of its carbon atoms or adding hydrogen atoms from an external source (Asgharzadeh Shishavan et al. 2011; Yang et al. 1998; Bellussi et al. 2013). Thermal cracking is one of several heavy oil upgrading processes which relies on temperatures higher than 350 °C to break the C-C bonds, reject some carbon while concentrating the hydrogen atoms onto a lighter product with lower viscosity, higher °API gravity (Speight 2012), improved combustibility and ultimately much more attenuated environmental impact.

The reaction mechanisms involved in thermal cracking of heavy oil are very complex and consist of not only reactions that form the desired products but also reactions that lead to low value products such as coke (Zachariah et al. 2013; Joshi et al. 2008; Torregrosa-Rodríguez et al. 2000; Marsh et al. 1999). Coke formation during thermal cracking, and upgrading in general, reduces the liquid yield and deactivates catalyst, whenever applicable (Wang et al. 2016b; Vafi et al. 2012a; Zachariah et al. 2013). Suppressing coke formation has been the subject of many investigations, and a number of alternatives have been suggested; including addition of a hydrogen donor (Rahmani et al. 2002; James G. Speight 1982; A. Del Bianco, Panariti, Prandini, et al. 1993), fine particles (Wang et al. 1998; Nhieu et al. 2016; Tanabe & Gray 1997; Sanaie et al. 2001; Rahimi et al. 1999; Bi et al. 2007) and organic-based materials such as coke (Gentzis et al. 2001) to the crude oil feed. For example, different researchers showed that in presence of fines, coke precursors

accumulate on the surface of the solids, which provides better dispersion and exposure to hydrogen donors from the bulk, leading to a lower fraction of toluene insolubles (TI) and an increase in the overall conversion to liquid (Sanaie et al. 2001; Tanabe & Gray 1997). This in turn enabled running thermal cracking at higher temperatures, while ensuring less coking.

Commercial scale thermal cracking units use temperatures > 420 °C to enable rapid conversion without catalyst addition. On the other hand, using proper catalysts significantly reduces the operating conditions (Rana et al. 2007). In principle, the catalyst for breaking C-C bonds during heat treatment promotes carbenium ion intermediates with its acid sites (Gong et al. 2008; Corma & Orchillés 2000). However, catalyst use during thermal cracking is limited in view of the high potential for deactivation (Wang & Manos 2007). Coke phase can easily deposit on the surface of conventional catalysts rendering the pores inaccessible. Moreover, the high concentration of metals in VR increases the potential for catalyst poisoning (Gao et al. 2012). Nevertheless, some studies on catalytic cracking of VR were performed and are summarized Table 4.1. As can be seen in the table, and to the best of our no knowledge, no previous literature has considered catalytic cracking of VR in a closed reactor arrangement. Our earlier results confirmed achieving higher liquid yield with better quality in an autoclave relative to an open system (Eshraghian & Husein 2017). Preventing vapors from escaping the reactor arrangement leads to high liquid volume, thus reduces the concentration of the pseudo phase and ultimately the coke yield. Furthermore, from a commercial point of view, most of the cracking catalysts are expensive. Subsequently, there is a pressing need for effective and inexpensive upgrading catalysts (Quitian & Ancheyta 2016).

**Table 4.1:** Summary of literature work on catalytic cracking of VR.

Reference	Experimental Conditions			Major Conclusions																												
	Feed	Reactor mode	Catalyst																													
Meng et al. (Meng et al. 2005)	Chinese Daqing vacuum residue Density (20 °C) =0.9221 g/cm <sup>3</sup> Viscosity (100 °C) = 106 mm <sup>2</sup> /s H/C mol ratio=1.76 Resin and asphaltenes = 22.56 wt%	Fluidized bed	CEP-1 (catalytic pyrolysis process(CPP) catalyst) Surface area=80 m <sup>2</sup> /g Pore volume =0.19 cm <sup>3</sup> /g Particle size distribution (wt%): 0–20 (mm)=1.2 20–40 (mm)=13.4 40–80 (mm)=55.9 >80 (mm)=29.5	T=660 °C Residence time=2.2 s Catalyst/oil mass ratio=15.5	Conversion to liquid product (without dry gas or LPG) = 22.68 wt% Coke= 14.78 wt%																											
Meng et al. (Meng et al. 2007)	Chinese Daqing vacuum residue Density (20 °C) =0.9221 g/cm <sup>3</sup> Viscosity (100 °C) = 106 mm <sup>2</sup> /s H/C mol ratio=1.76 Resin and asphaltenes = 22.56 wt%	Fluidized bed	CEP-1 (catalytic pyrolysis process(CPP) catalyst) Chemical content, wt%: Al <sub>2</sub> O <sub>3</sub> =52 wt% Fe <sub>2</sub> O <sub>3</sub> =1 wt% Surface area =104 m <sup>2</sup> /g Pore volume=0.08 cm <sup>3</sup> /g Particle size distribution (wt%): 0–20 (mm)=1.9 20–40 (mm)=20.3 40–80 (mm)=43.9 80–120 (mm)=12.5 >120 (mm)=21.4	T=600-716 °C Catalyst/oil mass ratio=6-27	<ul style="list-style-type: none"> <li>➤ Reaction temperature ↑ → Coke yield ↑</li> <li>➤ Catalyst to oil mass ratio ↑ → Coke yield ↑</li> </ul>																											
Gao et al. (Gao et al. 2012)	Changqing VR density (20 °C) =939.7 kg/m <sup>3</sup> viscosity (80 °C) =172.73 mm <sup>2</sup> /s H/C mol ratio=1.76 Asphaltenes= 1.6 wt%	Fixed fluidized bed	Commercial Y zeolite-based equilibrium FCC catalysts: (LVR–60R, CDC) supplied by CNPC. <table border="1" style="margin-left: auto; margin-right: auto;"> <thead> <tr> <th></th> <th>LVR-60R</th> <th>CDC</th> </tr> </thead> <tbody> <tr> <td>Composition (wt%)</td> <td></td> <td></td> </tr> <tr> <td>Al<sub>2</sub>O<sub>3</sub> wt %</td> <td>48.2</td> <td>51.5</td> </tr> <tr> <td>RE<sub>2</sub>O<sub>3</sub> wt %</td> <td>5.5</td> <td>4.8</td> </tr> <tr> <td>Pore volume (cm<sup>3</sup>/g)</td> <td>0.19</td> <td>0.14</td> </tr> <tr> <td>Surface area (m<sup>2</sup>/g)</td> <td>141</td> <td>77</td> </tr> </tbody> </table>		LVR-60R	CDC	Composition (wt%)			Al <sub>2</sub> O <sub>3</sub> wt %	48.2	51.5	RE <sub>2</sub> O <sub>3</sub> wt %	5.5	4.8	Pore volume (cm <sup>3</sup> /g)	0.19	0.14	Surface area (m <sup>2</sup> /g)	141	77	T=500 °C Catalyst/oil mass ratio=6	<table border="1" style="margin-left: auto; margin-right: auto;"> <thead> <tr> <th></th> <th>LVR-60R</th> <th>CDC</th> </tr> </thead> <tbody> <tr> <td>Conversion to liquid product</td> <td>73.4</td> <td>69.1</td> </tr> <tr> <td>Coke wt%</td> <td>9.69</td> <td>10.81</td> </tr> </tbody> </table>		LVR-60R	CDC	Conversion to liquid product	73.4	69.1	Coke wt%	9.69	10.81
	LVR-60R	CDC																														
Composition (wt%)																																
Al <sub>2</sub> O <sub>3</sub> wt %	48.2	51.5																														
RE <sub>2</sub> O <sub>3</sub> wt %	5.5	4.8																														
Pore volume (cm <sup>3</sup> /g)	0.19	0.14																														
Surface area (m <sup>2</sup> /g)	141	77																														
	LVR-60R	CDC																														
Conversion to liquid product	73.4	69.1																														
Coke wt%	9.69	10.81																														
Safiri et al. (Safiri et al. 2015)	Vacuum residue of the Abadan refinery in Iran kinematic viscosity (100 °C)= 572 cSt specific gravity at 25 °C= 1.004	Semi batch (N <sub>2</sub> flow rate=15 mL/min)	<table border="1" style="margin-left: auto; margin-right: auto;"> <thead> <tr> <th></th> <th>Fe<sub>2</sub>O<sub>3</sub> (III)</th> <th>Al<sub>2</sub>O<sub>3</sub> (γ)</th> </tr> </thead> <tbody> <tr> <td></td> <td></td> <td></td> </tr> </tbody> </table>		Fe <sub>2</sub> O <sub>3</sub> (III)	Al <sub>2</sub> O <sub>3</sub> (γ)				T=440-500 °C P=1-5 bar Catalyst concentration = 0-1000 ppm	<ul style="list-style-type: none"> <li>➤ Reaction temperature ↑ → Liquid product yield ↑</li> <li>➤ Reaction Pressure ↑ → Liquid yield ↓</li> </ul> <table border="1" style="margin-left: auto; margin-right: auto;"> <thead> <tr> <th>Pressure (bar)</th> <th>1</th> <th>5</th> </tr> </thead> <tbody> <tr> <td></td> <td></td> <td></td> </tr> </tbody> </table>	Pressure (bar)	1	5																		
	Fe <sub>2</sub> O <sub>3</sub> (III)	Al <sub>2</sub> O <sub>3</sub> (γ)																														
Pressure (bar)	1	5																														

	asphaltenes= 4.3 wt% H/C mol ratio= 1.4		Average particle size (nm)	20-30	<30			Temperature (°C)	Coke (wt%)	Liquid (wt%)	Coke (wt%)	Liquid (wt%)
			Surface area (m <sup>2</sup> /g)	80-90	>30			440	28	58	-	-
								460	27	59	-	-
								480	26	60	28.9	39
								500	23	62	28.2	49
								➤ In presence of catalyst → more liquid yield and less coke yield				
								Catalyst	ppm	Coke (wt%)	Liquid (wt%)	
								Control	0	26.3	60	
								Al <sub>2</sub> O <sub>3</sub>	100	22.19	64.43	
								Al <sub>2</sub> O <sub>3</sub>	500	25.19	64.45	
								Al <sub>2</sub> O <sub>3</sub>	1000	23.56	66.44	
								Fe <sub>2</sub> O <sub>3</sub>	100	25.36	62.86	
								Fe <sub>2</sub> O <sub>3</sub>	500	23.47	66.67	
								Fe <sub>2</sub> O <sub>3</sub>	1000	24.68	62.99	

Nanotechnology has emerged as a new approach for the recovery and upgrading of heavy oil (Cheraghian & Hendraningrat 2015; Abu Tarboush & Husein 2015; Husein & Alkhaldi 2014). With their inherent high degree of dispersion, nanoparticles (NPs) serve as ideal catalyst materials, even at low concentrations, since they are capable of mitigating the internal and the external mass transfer barriers (Abu Tarboush & Husein 2015; Husein & Alkhaldi 2014). In principle, and in the context of heavy oil thermal cracking, dispersed NPs may have a dual effect: promote thermal cracking of heavy oil as well as adsorb and, hence, disperse coke precursors. Previous results from our group showed that commercial and in situ prepared  $\text{Al}_2\text{O}_3$  NPs have promoted thermal cracking at 350 °C of a heavy oil mixture composed of Athabasca vacuum gas oil and vacuum residue with an °API gravity of  $16.8 \pm 2.2$  and a viscosity of  $1485 \pm 95$  cP (Husein & Alkhaldi 2014). Yet, Husein & Alkhaldi (Husein & Alkhaldi 2014) observed that the NP activity was restricted by particle aggregation, in part due to the relatively low viscosity of the feedstock. The current investigation builds on our previous work and applies in situ prepared and commercial  $\text{Al}_2\text{O}_3$  NPs to the upgrading of Athabasca vacuum residue (AVR) at higher temperatures. Alumina is a known catalyst support and a cracking catalyst by virtue of its acidity and hence ability to break C-C bonds (Husein & Alkhaldi 2014). In addition, we explore the use of drill cuttings (DC), a waste product from drilling industry, as a potential inexpensive catalyst for thermal cracking. It is worth noting that constructive use of a waste material makes both economic and environmental sense (Mostavi et al. 2015). For example, pyrolysis of oil sludge in presence of oil sludge ash, a solid waste produced in the petroleum industry, displayed an increase in the conversion and the quality of the light product through decreasing the carbon residue and/or the asphaltenes yield (Aimin Li et al. 2015; Cheng et al. 2016; Cheng et al. 2017; Shie et al. 2004).

## 4.3 Experimental procedure

### 4.3.1 Materials

The as received Athabasca vacuum residue (AVR) contained  $3.6\pm 3.4$  wt% fine solids,  $29.5\pm 3.2$  wt% asphaltenes and  $63.9\pm 4.9$  wt% maltene. Fines were removed from AVR before the thermal cracking experiments by addition of toluene (BDH 99.8%, VWR, Canada), filtration and evaporating the toluene (Eshraghian & Husein 2017). The AVR feed stock, following fines removal, exhibited °API gravity of  $4.4\pm 1.1$  at 24°C, viscosity of  $> 200,00$  cP at 37°C,  $31.6\pm 3.2$  wt% asphaltenes and  $68.4\pm 4.9$  wt% maltene. *n*-heptane (BDH technical, VWR, Canada) was used to reject asphaltenes, and nitrogen (Praxair Specialty Gas & Equipment, AB, Canada) was used to purge air from the reactor prior to upgrading. For the experiments involving *in situ* preparation of Al<sub>2</sub>O<sub>3</sub> NPs, aluminum nitrate nonahydrate, Al(NO<sub>3</sub>)<sub>3</sub>·9H<sub>2</sub>O (98% pure powder, Sigma-Aldrich Fine Chemical, ON, Canada) was used as the precursor salt, while commercial Al<sub>2</sub>O<sub>3</sub> NPs (dp<50 nm, 99.8%, Sigma-Aldrich Fine Chemical, Toronto, ON) were used for comparison. Sandstone-based drill cuttings (DC) were provided by Executive Mat Service, Calgary, AB. The as received DC were washed with water in order to separate impurities and then dried in an oven at 70°C for 12 h. Dried cuttings were screened with 350 µm sieve and only those with diameter < 350 µm were used for upgrading.

### 4.3.2 Thermal cracking

The thermal cracking experiments were conducted in a closed reactor system following procedures outlined in our previous work (Eshraghian & Husein 2017). In brief, a 100 mL Parr reactor (3.3 cm i.d. and 11.7 cm length, 4590 Micro Bench Top Reactor, Parr Instrument Company, IL, USA) was loaded with 50 g of the feedstock. Then, the reactor was heated to a set temperature at a 25 °C/min temperature ramp. Once the temperature reached 120°C, the reactor was purged with

nitrogen to displace air. For experiments involving NPs, *commercial* Al<sub>2</sub>O<sub>3</sub> NPs were added to the reactor at 190°C to form an AVR suspension of 10,000 ppm NPs under 500 rpm of mixing prior to thermal cracking. The *in situ* preparation of dispersed Al<sub>2</sub>O<sub>3</sub> NPs followed the work of Husein and Alkhaldi (Husein & Alkhaldi 2014). In brief, 2.5 ml of 120 g/L aqueous Al(NO<sub>3</sub>)<sub>3</sub> solution was mixed with 50 g of AVR at 190 °C and 500 rpm prior to thermal cracking. It is worth noting that a higher concentration of the *commercial* NPs was used due to their higher tendency to agglomerate and separate (Husein & Alkhaldi 2014). For the experiments involving DC, DC was mixed with AVR to form suspensions of 10 wt%, 20 wt% or 30 wt% DC. In these experiments the required mass of DC was first added to 20 g of the AVR at 190°C, followed by the addition of the remaining AVR sample under continuous mixing of 500 rpm. It should be noted that experiments in presence of DC were the only experiments that involved mixing during thermal cracking in this study, since per our previous results (Eshraghian & Husein, 2017), mixing negatively impacted thermal cracking. Thermal cracking using DC without mixing resulted in precipitation of DC and produced huge amount of TI which was very difficult to remove from the reactor. Following purging and catalyst addition, the reactor unit was tightly sealed to achieve a batch mode operation. The reaction time started when the reactor temperature reached 300°C. The reactor unit was fixed at 400°C or 420°C for 60 min. During the experiment, the temperature, pressure and total energy input to the reactor were recorded every 5 min. At the end of the reaction, heating was stopped, the reactor vessel was immediately quenched in a water bath at 24°C and its final pressure was recorded. The gaseous product was slowly vented and the liquid and solid products were collected for analysis.

### 4.3.3 Characterization

The upgraded product was centrifuged at 5,000 rpm for 60 min in order to separate the solids, e.g. catalyst, before its viscosity and °API gravity could be recorded. The viscosity of the product oil before toluene addition, the oil after filtering TI and rejecting toluene, and the maltene fraction were measured at 37°C using a Brookfield digital viscometer (Model: LVDV-1 PRIME, Brookfield Engineering Laboratories Inc., MA, USA). The °API gravity of the product oil before adding toluene and its maltene fraction was determined at 25°C using a specific gravity bottle (Thomas Scientific, NJ, USA). The toluene insolubles (TI) and the asphaltenes were extracted from the oil samples by sequential addition and evaporation of toluene and *n*-heptane mediated by filtration as described in our earlier work (Eshraghian & Husein 2017). The light hydrocarbon products lost during solvent evaporation were accounted for by mass balance.

To further quantify the extent of upgrading, the feedstock and the upgraded AVR before addition of toluene and TI rejection were introduced to a high-temperature simulated distillation (HTSD) (Aglient GC, ON, Canada) and analyzed following ASTM D7169-2005 standard procedure. In addition, some samples of the gaseous product were analyzed using gas chromatography (Model: Varian-3900 GC, Varian Inc., USA). Gas sampling was conducted once the reaction time elapsed before quenching the reactor following procedures outlined in our previous work (Eshraghian & Husein 2017).

In order to characterize TI and asphaltenes, thermogravimetry (TG) and differential scanning calorimetry (DSC) were performed on STA 6000 simultaneous thermal analyzer (PerkinElmer Inc., AB, Canada). STA measurements involved heating up a small mass of the sample, under 30 mL/min of flowing air, to 800°C at constant temperature ramp of 10 °C/min. Elemental analyzer (2400 series II, Perkin Elmer Inc., AB, Canada) was used to determine the H/C

ratio of some asphaltenes and TI samples. The X-Ray diffraction (XRD) analysis of TI, NPs and DC was carried out on Ultima III Multi Purpose Diffracto meter (Rigaku Corp., The Woodlands, TX, USA) with Cu K $\alpha$  radiation as the X-ray source operating at 40 kV and 44 mA. The scans were done in the range from 1 to 90° of  $\theta$ -2 $\theta$  goniometer using a 0.02° step and a counting time of 2.0° per minute. Scanning electron microscopy (SEM) (Quanta FEG 250, FEI inc., Canada) photographs were collected to further analyze TI, NPs, DC and leftover materials following STA analysis. Energy-dispersive X-ray spectroscopy (EDX) was also conducted to provide elemental analysis of the particles using Quantax 5030 (Bruker, Canada) by zooming on a specific location of the SEM sample. Transmission electron microscopy (TEM) of the *in situ* prepared NPs was conducted on a Tecnai F20 TEM (FEI USA Inc. Hillsboro, OR) operating at 200 KV field emission. TI, the most likely location for NPs, was washed with toluene few times to ensure removal of the oil residue. Finally, TI was dispersed in toluene using an ultrasonic bath (Model: CPX2800, Crystal Electronics Inc., ON, Canada) and one drop of the suspension was added to a carbon-coated copper grid and left to evaporate before the analysis. The surface area of DC and *commercial* Al<sub>2</sub>O<sub>3</sub> NPs was evaluated using nitrogen adsorption at -196°C. The as received samples were first degassed at 150°C under nitrogen environment overnight prior to the adsorption. The samples were then loaded into a Micromeritics surface area analyzer (TriStar 2000, Micromeritics Instrument Corporation, USA). The Brunauer-Emmet-Teller (BET) model was used to determine the surface area of the samples. The total pore volume of was calculated by nitrogen uptake at the relative pressure (P/P<sub>0</sub>) of 0.99 using Barrett-Joyner-Halenda (BJH) method.

Three different replicates were prepared for some of the experiments and the standard error bars are reported. Figures 4.1 and 4.2 summarise the experimental procedures and the experimental variables.



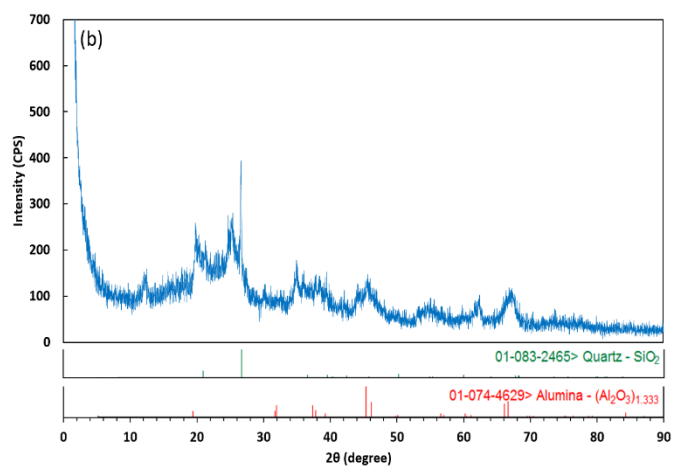
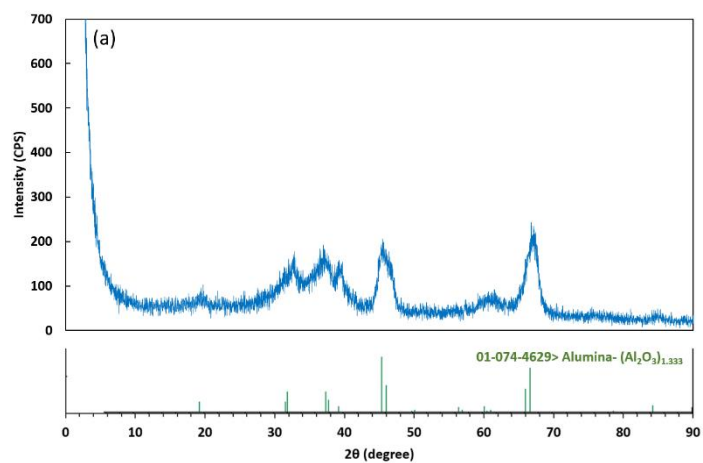
## 4.4.1 Catalyst Characterization

### 4.4.1.1 Alumina characterization

The surface area and pore volume of the as received *commercial* Al<sub>2</sub>O<sub>3</sub> NPs measured by Tristar surface area analyzer and estimated by fitting BET and BJH models to the adsorption isotherm were 155 (m<sup>2</sup>/g) and 1.01 (cm<sup>3</sup>/g), respectively. Figure 4.3(a) shows the XRD pattern of the as received *commercial* NPs. The mean Al<sub>2</sub>O<sub>3</sub> crystal size estimated by Scherrer's equation (Mirzayi & Shayan 2014) from the XRD peak at  $2\theta = 67.08^\circ$  is 4.5 nm. The geometric surface area calculated using the XRD estimate assuming spherical crystals is 335 m<sup>2</sup>/g, almost twice the value obtained from the BET model, probably due to a smaller crystal size than particle size.

The XRD analysis, EDX pattern, SEM image and its corresponding particle size distribution histogram of the TI collected following thermal cracking of AVR in presence of *commercial* Al<sub>2</sub>O<sub>3</sub> at 400°C is presented in Figure 4.3(b-e). The XRD pattern of Figure 4.3(b) captures all the peaks of Figure 4.3(a), but also shows other peaks for SiO<sub>2</sub>, mostly belonging to remaining fines, hydrocarbons (Nassar & Husein 2007) and carbonaceous material (Al-Marshed *et al.* 2015), especially at the lower end of the spectrum. The mean Al<sub>2</sub>O<sub>3</sub> crystal size estimated by Scherrer's equation from the XRD pattern of Figure 4.3(b) is 5 nm, which is similar to the as received Al<sub>2</sub>O<sub>3</sub> NPs. Major peaks in EDX pattern of Figure 4.3(c) belong to Al and O, while some other peaks can be attributed to adsorbed material and unremoved fines, which is inline with the XRD result. Discussion pertaining to the morphology of TI will follow. Since, particle size analysis in Figure 4.3(e) could be clouded by the adsorbed impurities, the SEM analysis accompanied by EDX was performed following STA analysis of the TI, which should at least remove combustible materials. EDX pattern of this sample in Figure 4.3(f) shows sharper Al and O peaks, while SEM image of Figure 4.3(g) shows finer particles. The particle size distribution histogram for this

sample is presented in Figure 4.3(h). It should be note that the particles used in establishing Figure 4.3(d) and 4.3(h) were manually selected in order to eliminate background noise; including those belonging to aluminium from leftover fines as will be discussed later. Despite the heat treatment, a comparison between Figure 4.3(e) and 4.3(h) histograms confirms smaller particle range after removing the combustibles. Accordingly, particle size from SEM image of TI leftover from STA analysis is considered more representative of the  $\text{Al}_2\text{O}_3$  particles during thermal cracking. The surface area calculated from the particle analysis in Figure 4.3(h) is  $2 \text{ m}^2/\text{g}$ , which is less than the as received particles, due to the presence of adsorbed impurities and probable aggregation during thermal cracking.



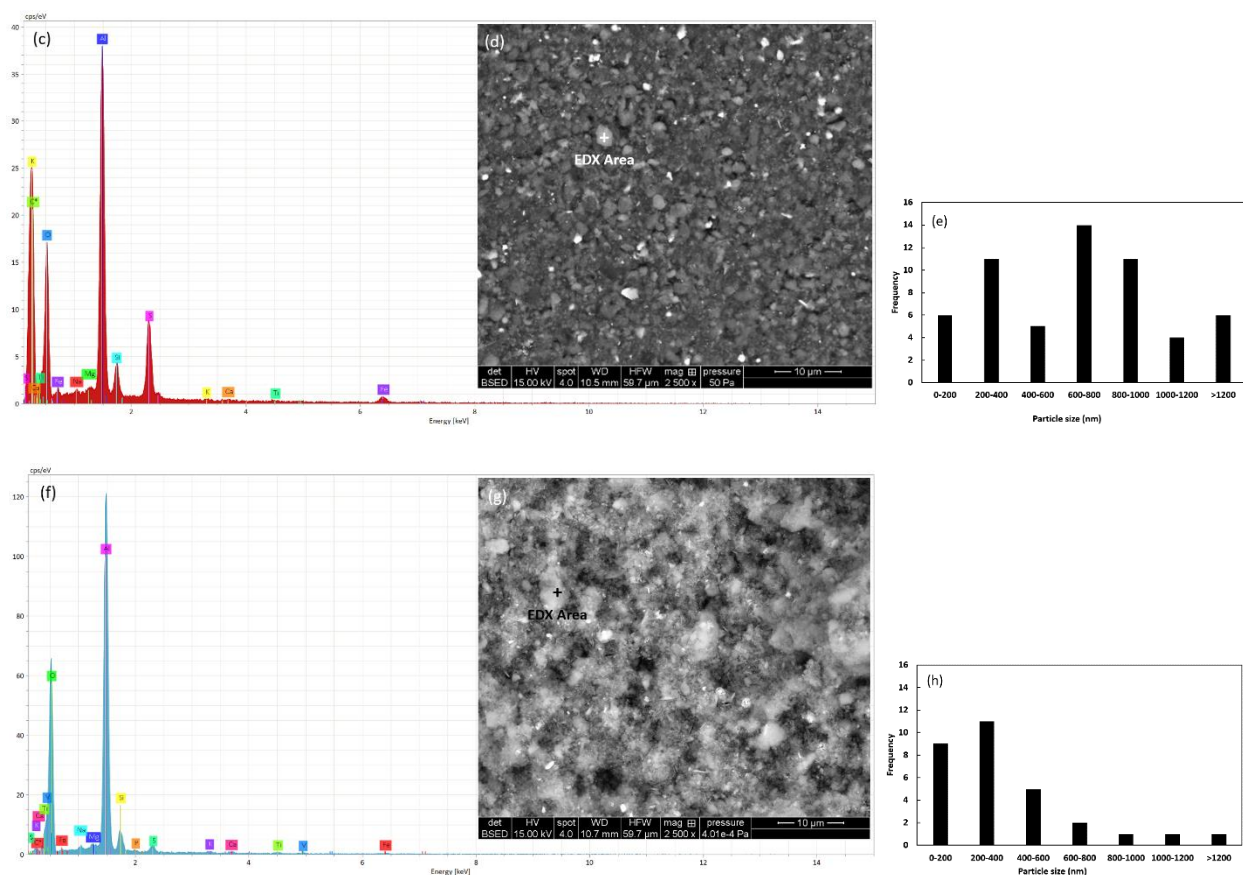


**Figure 4.3:** (a) XRD pattern of as received *commercial*  $\text{Al}_2\text{O}_3$  NPs; (b) XRD pattern, (c) EDX pattern, (d) SEM image and (e) the particle size distribution histogram of the TI following thermal cracking of AVR in presence of *commercial*  $\text{Al}_2\text{O}_3$  NPs; (f) EDX pattern, (g) SEM image and (h) the particle size distribution histogram of leftover material from STA analysis of the TI.

XRD analysis, EDX pattern, SEM photograph and particle size distribution histogram of TI following thermal cracking of AVR in presence of *in situ* prepared  $\text{Al}_2\text{O}_3$  particles are depicted in Figure 4.4(a-d). The XRD finger print includes noise, especially at the lower end of the spectrum, representing hydrocarbons and carbonaceous material, and no sharp peaks except that of  $\text{SiO}_2$  probably associated with remaining fines. Husein and Alkhalidi (2014) (Husein & Alkhalidi 2014) reported the formation of amorphous *in situ* prepared  $\text{Al}_2\text{O}_3$  in heavy oil, which could also be the case here. The EDX elemental analysis in Figure 4.4(b) of a spherical particle within the

SEM photograph of Figure 4.4(c) confirmed the existence of Al and O, component of Al<sub>2</sub>O<sub>3</sub> particles, in addition to other impurities as discussed above. The TEM image in Figure s4.3(a) and the EDX mapping for Al and O atoms in Figure s4.3(b) confirmed the presence of Al<sub>2</sub>O<sub>3</sub> particles, mainly in spherical shape. The histogram of the Al<sub>2</sub>O<sub>3</sub> particles collected with the TI prior to STA analysis is shown in Figure 4.4(d). This wide range of particle size distribution could be attributed to deposited/adsorbed impurities onto Al<sub>2</sub>O<sub>3</sub> particles. In order to obtain more reliable results, TI sample following STA analysis was collected for EDX, SEM and particle size distribution analyses, as shown in Figure 4.4(e-g). EDX pattern in Figure 4.4(e) of a selected spherical particle from SEM analysis indicates mainly Al and O elements and much less carbonaceous impurities compared to EDX result of the sample before STA analysis. Figure 4.4(f) and Figure s4.3(c) confirm the spherical shape of the Al<sub>2</sub>O<sub>3</sub> particles even after STA heat treating. The mean particle diameter calculated from SEM image of Figure s4.3(c) averaged over 82 particles was 90±80 nm. Large Al<sub>2</sub>O<sub>3</sub> particles also appeared in the SEM image, which could have formed at the very high temperature of the STA analysis or from aggregation during thermal cracking, but they were few in number. Accordingly, the particle size distribution of Figure 4.4(g) is most likely representative of the dispersed *in situ* Al<sub>2</sub>O<sub>3</sub> NPs with average diameter < 40 nm. The geometric surface area calculated based on Figure 4.4(g) was found to be 3.2 m<sup>2</sup>/g, 1.6 times larger than the *commercial* NPs. This observation is inline with previous findings (Husein & Alkhaldi 2014) and suggests lower extent of aggregation and higher stability of the *in situ* prepared NPs. Unfortunately, no other means, e.g. Tristar surface area analyzer, XRD, etc. could be used to measure the surface area of the *in situ* Al<sub>2</sub>O<sub>3</sub> particles due to their low concentration, difficulty to separate from impurities and lack of crystallinity.

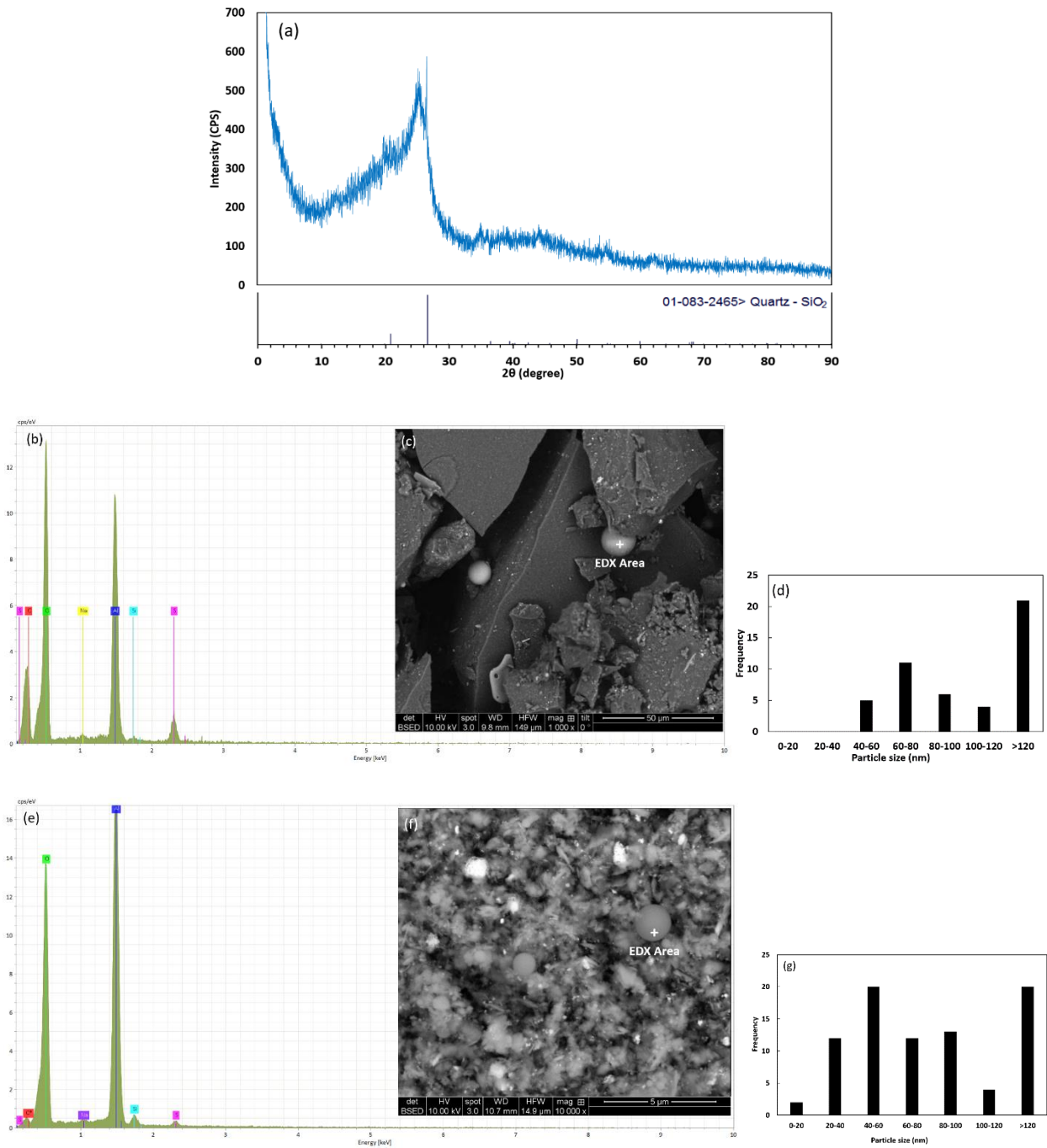
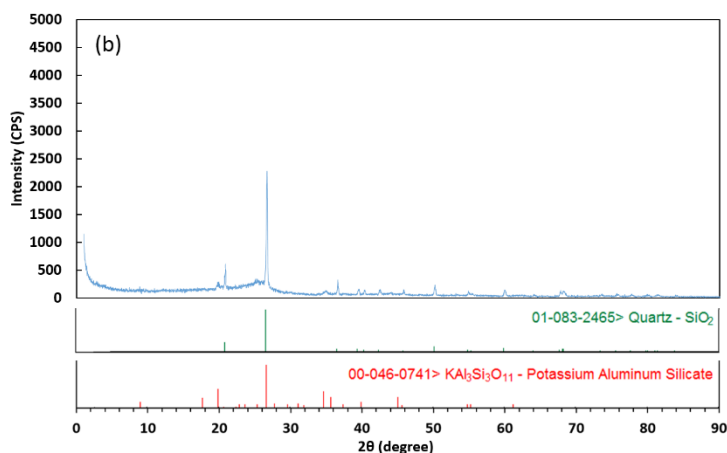
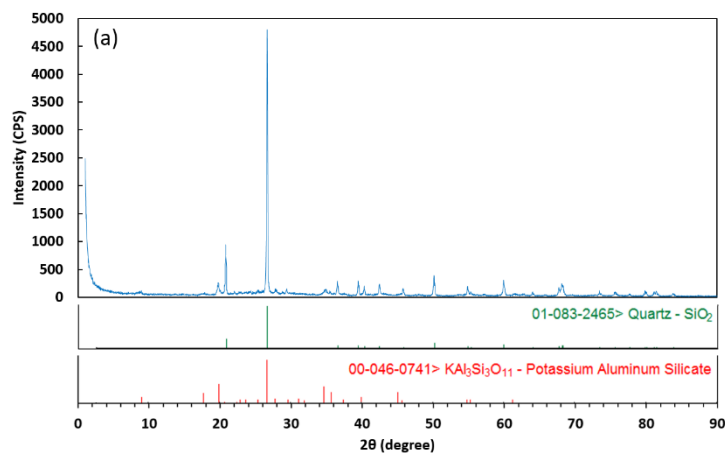


**Figure 4.4:** (a) XRD pattern, (b) EDX pattern, (c) SEM image and (d) the particle size distribution histogram of TI following thermal cracking of AVR in presence of *in situ* prepared Al<sub>2</sub>O<sub>3</sub> NPs; (e) EDX pattern, (f) SEM image and (g) the particle size histogram of leftover material from STA analysis of the TI.

#### 4.4.1.2 DC characterization

The surface area and pore volume of the as received DC measured by Tristar surface area analyzer were 5 (m<sup>2</sup>/g) and 0.02 (cm<sup>3</sup>/g), respectively. XRD pattern of the as received DC in Figure 4.5(a) shows mostly quartz (a SiO<sub>2</sub> polymorph) mineral with some traces of mica. XRD pattern, SEM image and particle size distribution histogram of TI collected from the upgraded AVR at 420°C in presence of 10 wt% DC are depicted in Figure 4.5(b-d). XRD pattern of Figure 4.5(b) confirms the existence of all peaks in Figure 4.5(a) in addition to an amorphous phase, probably belonging to hydrocarbons and carbonaceous species, appearing as a hump in the range of  $2\theta=1-34^\circ$ , i.e. low end of the spectrum. A representative SEM photograph and its corresponding DC particle size distribution histogram are given in Figure 4.5(e,f). In order to get better understanding of the composition throughout the sample, the full EDX mapping of Figure 4.5(e) is presented in Figure 4.5(c,d) and Figure s4.6(a-d). Results confirm the presence of Si trace, which is attributed to DC particles and/or fines originated from AVR. In addition, carbonaceous material mainly in spherical or slightly ellipsoidal aggregates can be seen when overlapping Figures 4.5(e) and (c). The carbonaceous material was not uniformly dispersed throughout, but rather consisted of a combination of coke domains and a region of deposition of what appears to be coke precursors adsorbed/deposited onto DC particles (Bi *et al.* 2007). The deposition of the coke precursor can be inferred from the less vivid carbon color in regions where Si color is pronounced in Figure 5(c) and (d), and also bearing in mind the XRD pattern of Figure 4.5(b). While Figures 4.5(c) and (e) show separate regions of coke aggregates, literature findings suggest that at low concentration of coke precursors, the coke precursors are expected to only form on catalyst particles (Bi *et al.* 2007). These observations are very helpful when interpreting the mechanism of thermal cracking in presence of DC.

The presence of the carbonaceous, and other impurities, on the surface of DC makes particle size analysis less reliable. Therefore, the EDX pattern, the corresponding SEM image and the particle size distribution of the above sample following STA analysis are depicted in Figure 4.5(g-i). EDX pattern shows major peaks for Si and O and some other elements leftover from combusted hydrocarbons or fines, e.g. Al. It should be noted that, contrary to the *in situ* prepared  $\text{Al}_2\text{O}_3$ , the aluminium rich regions were not spherical, which helped differentiating the NPs. Finally, the SEM photographs of the TI-containing DC following STA analysis depicted in Figures 4.5(h) and 4.6(e) shows some sharp DC edges, which could potentially be active sites for thermal cracking.



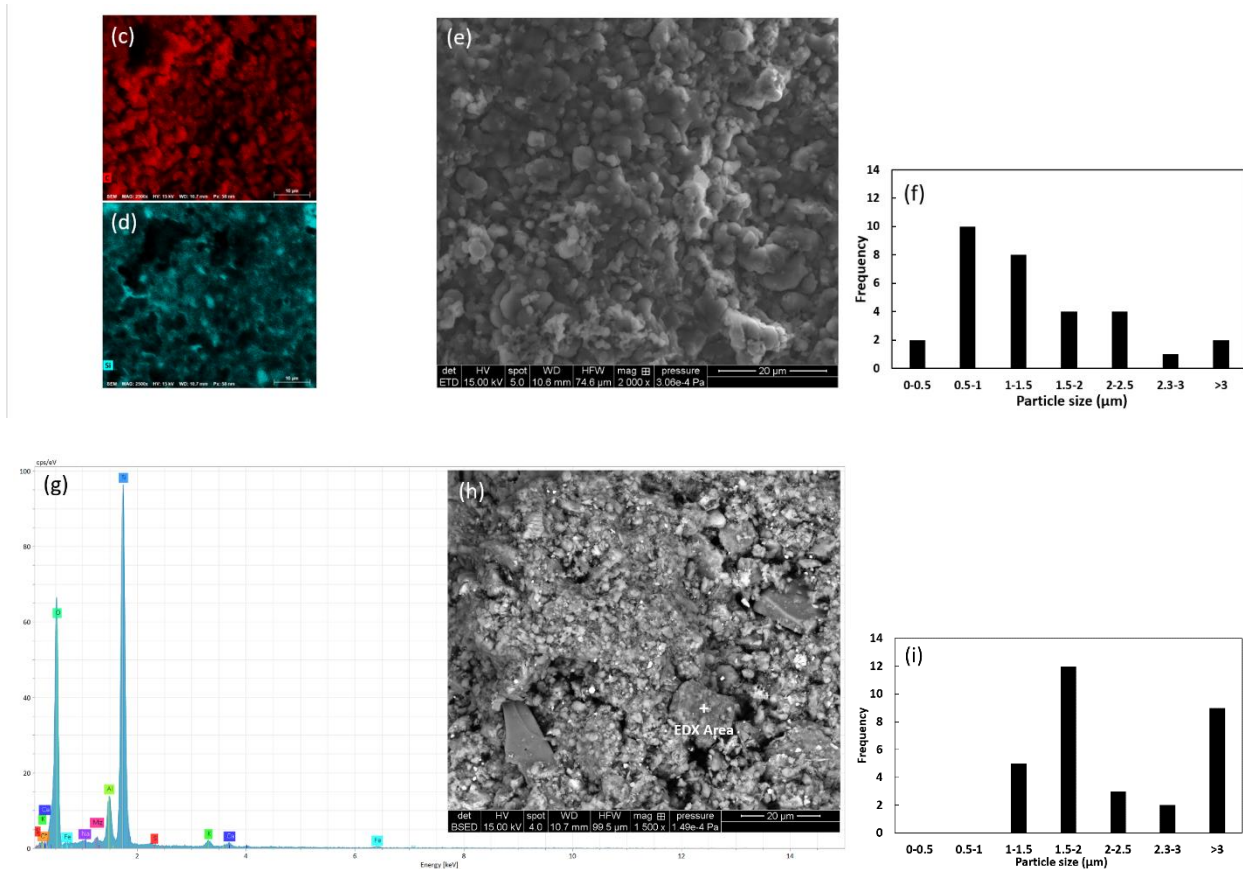


**Figure 4.5:** (a) XRD pattern of the as received DC; (b) XRD pattern, (c) SEM image with C EDX mapping, (d) SEM image with Si EDX mapping, (e) SEM photograph, (f) DC particle size distribution histogram of TI following thermal cracking of AVR in presence of 10 wt% DC at 420°C; (g) EDX pattern, (h) SEM photograph, (i) DC particle size distribution of leftover material of STA analysis of the TI.

#### 4.4.1.3 TI characterization from control sample

In order to further identify the impurities that attach to the catalyst during catalytic thermal cracking, SEM images and the corresponding EDX patterns for a control TI sample after thermal cracking of AVR at 420°C are shown in Figure 4.6(a-d). The EDX data suggests that inorganic materials, present in AVR as fines, were incorporated into the TI phase (Wang *et al.* 1998). SEM images and EDX pattern show two main regions, a smooth carbon and sulfur rich region, area (1), and another rich with heteroatoms and fines, area (2), probably originated from fines leftover in

the AVR feedstock. From a morphological stand point, the carbon rich region could be classified as shot-type coke due to the smooth surface with no evidence of hole (Al-Marshed *et al.* 2015), similar to the carbon obtained in presence of *in situ* NPs in Figures 4.4(c) and s4.4. On the other hand, the morphology of the TI produced in presence of DC, Figure 4.5(e), suggests more porous structure. It is worth noting that the shot-type coke has lower economic value compare to the sponge-type coke (Siskin *et al.* 2006). A decrease in the size of the TI particles and their lower coalescence in presence of DC, as can be seen when comparing Figures 4.5(e) and 4.6(d), suggest that DC suppressed the growth of the TI particles (Rahmani *et al.* 2003; Wang *et al.* 1998). On the other hand, in presence of the *in situ* NPs, the higher surface area coupled with the higher catalytic activity toward TI formation and the much smaller size of the NPs led to engulfing the NPs within the TI rendering them ineffective in controlling TI morphology, as can be seen in Figures 4.4(c) and s4.5(a). Contrary to this finding, *commercial* NPs had an impact on TI morphology, as can be seen in Figure 4.3(d), but resulted in a much less porous structure relative to DC, probably due to the much smaller particle size and lower concentration. The occurrence of less coalescence of TI in presence of DC signals appreciable dispersion sites for coke nucleation (Rahmani *et al.* 2003) at the concentration of DC employed. In addition, in the regions where *commercial* NPs and DC exist, there is no separate region as heteroatoms rich.

In order to understand the origin of the leftover material after STA analysis of TI from the control sample, which could be carbonaceous material or fines, leftover material from STA analysis of AVR *asphaltenes* was analyzed under SEM in Figure 4.6(e,f). The EDX elemental analysis in Figure 4.6(e) shows the very same elements leftover from TI after STA analysis per Figure s4.8. Consequently, the leftover material after STA analysis of TI most probably originates

from carbonaceous material. Lastly, Al and O rich regions of Figure 4.6(c) do not display the spherical morphology reported for the *in situ* Al<sub>2</sub>O<sub>3</sub> NPs in Figures 4.4(c) and (f).

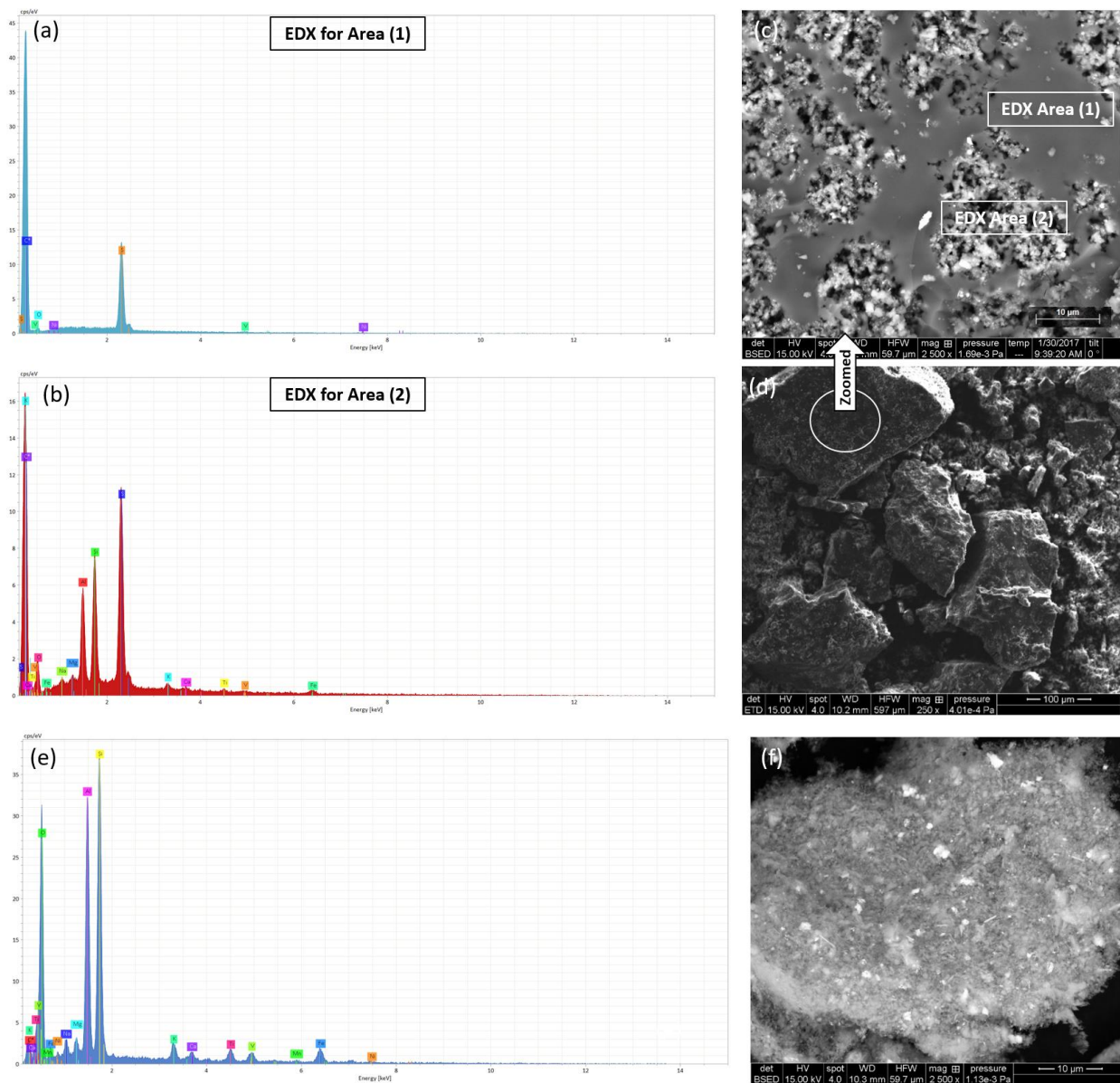
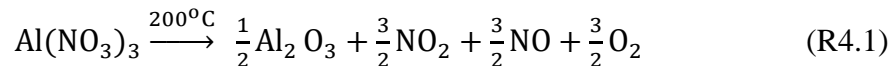


**Figure 4.6:** (a) EDX of area 1 (b) EDX of area 2 corresponding to (c) zoomed in SEM image, (d) zoomed out SEM image of control TI following thermal cracking of AVR at 420°C; (e) EDX pattern and (f) SEM image of leftover materials from STA analysis of *asphaltenes* from AVR.

#### 4.4.2 Effect of Al<sub>2</sub>O<sub>3</sub> NPs on the yield and product quality

Table 4.2 lists values for the total energy consumption and the final pressure, after cooling, for the runs involving *in situ* prepared and *commercial* NPs as well as a control run. While the total energy consumption was almost the same for all the runs, higher pressure buildup is observed for the samples containing alumina NPs. Real-time data reported in Figure 4.7 also show that thermal cracking in presence of the NPs resulted in higher pressure buildup, which was much more pronounced for the experiments involving *in situ* prepared NPs, especially in the time interval 20-30 min. It is constructive to note that this time interval corresponds to a temperature interval of 330°C to 400°C, which is appropriate for the thermal decomposition of the Al(NO<sub>3</sub>)<sub>3</sub> precursor (Husein & Alkhalidi 2014; Zeng *et al.* 1998; Yao *et al.* 2001a). The control experiments and those involving *commercial* Al<sub>2</sub>O<sub>3</sub> NPs contributed to just below 420 psi, while in the presence of *in situ* prepared NPs the pressure in the reactor was 1.7 times higher. This result could be attributed to evolution of gases per Al(NO<sub>3</sub>)<sub>3</sub> thermal decomposition reaction (R4.1) (El-Shereafy *et al.* 1998), a higher extent of thermal cracking in presence of the *in situ* prepared NPs and/or aquathermolysis products due to the water associated with the aluminium precursor (Hongfu *et al.* 2002).



Even though pressure calculations based on the compressibility factor and the stoichiometric amount of gases evolved from (R4.1) revealed ~60% of the pressure buildup can be attributed to (R1) gaseous products, Husein & Alkhalidi (2014) observed a concentration-independent pressure buildup when prepared 2,000, 3,000 and 4,000 ppm *in situ* Al<sub>2</sub>O<sub>3</sub> employing the same precursor. They also reported that aquathermolysis contributed to < 50% of the pressure buildup. Consequently, and bearing in mind the increase in TI content in presence of *in situ* NPs, we

conclude that the pressure buildup in presence of *in situ* NPs can be attributed to the three factors suggested above.

**Table 4.2:** The total energy input to the reactor and the final pressure after cooling for thermal cracking of AVR at 400°C with and without alumina NPs.

Nanoparticles	Cumulative energy (kWh)	Final pressure after cooling (psi)
Control	0.45±0.01	162±8
10,000 ppm <i>commercial</i> NP	0.46±0.01	169±6
6,000 ppm <i>in situ</i> NP	0.46±0.01	235

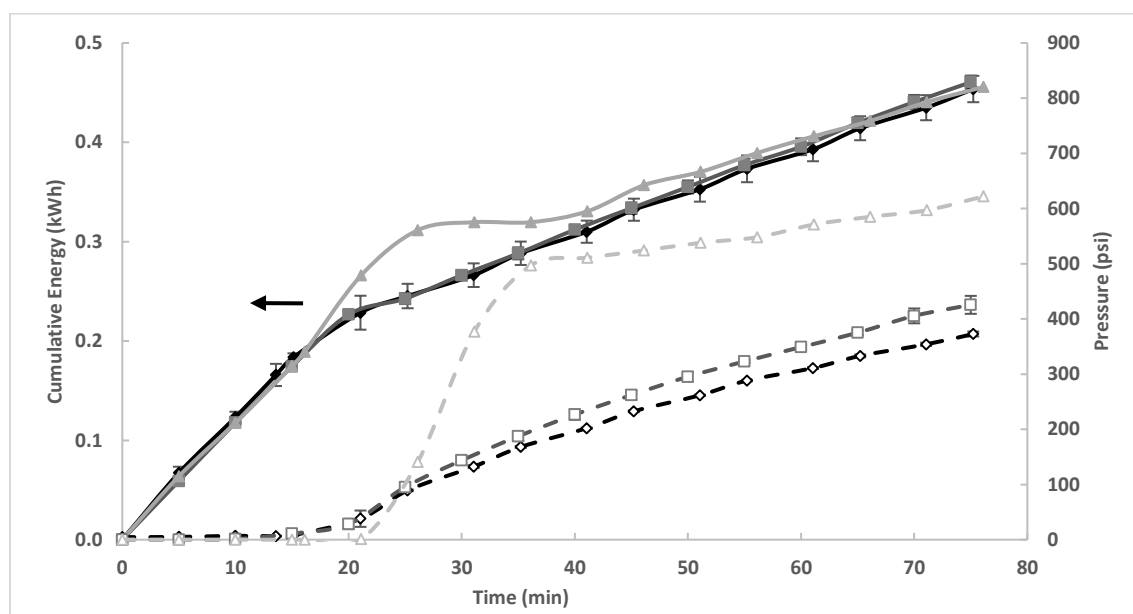


**Figure 4.7:** Energy consumption and pressure buildup inside the batch reactor during thermal cracking at 400°C for: (◆,◇) AVR, (■,□) AVR with 10,000 ppm *commercial* Al<sub>2</sub>O<sub>3</sub> NP, (▲,△) AVR with 6,000 ppm *in situ* Al<sub>2</sub>O<sub>3</sub> NP.

Figure 4.8(A) depicts a general increase in the production of gas and TI and a reduction in the maltene and asphaltene fractions for the experiments involving NPs. Again, those results were more pronounced for the *in situ* prepared NPs. Gas production during thermal cracking is typically associated with subjecting asphaltene to scission reactions, which also lead to coke precursors

(Gray 2015), or cracking of aliphatic groups in the oil (Tanabe & Gray 1997), while asphaltenes may form from polymerization reactions associated with radicals from the maltene fraction (Hauser *et al.* 2014). In turn, coke precursors may undergo polymerization ultimately leading to coke formation (Gonçalves *et al.* 2007). Hence, there is a strong link between coke and gaseous product formation during thermal cracking, which explains the increase in TI and gas fractions in our results at the expense of asphaltenes in presence of the NPs. Contrary to these observations, Safiri *et al.* (2015) reported an increase in the liquid fraction and decrease in the coke fraction upon thermal cracking of VR from Abadan refinery at 480°C in presence of 1,000 ppm *commercial* Al<sub>2</sub>O<sub>3</sub> NPs. They attributed this trend to effective acid sites onto the NPs. While acid sites promote C-C bond breakage (Husein & Alkhalidi 2014), which typically leads to coke formation especially at the higher temperature, the difference in these trends could be attributed to the different feedstock and its asphaltenes content. A closer look at the chemical nature of the TI using elemental analysis and STA will follow. Figure 4.8(A) shows no major difference in the total loss due to solvent evaporation between the samples containing *commercial* NPs and the control sample, while slightly lower loss for the *in situ* NPs. The difference in losses can be attributed to higher extent of cracking in presence of *in situ* NPs, which contributed to more non-condensables. Loss due to solvent evaporation should be added to the maltene product, as shown in the dotted rectangles.

In terms of °API gravity and viscosity, Figure 4.8(B,C) shows a depreciation of the °API gravity of the product oil in presence of the NPs and an improvement in the °API gravity and the viscosity of the maltene fraction. Again this improvement was most significant in presence of the *in situ* prepared NPs. The depreciation of the °API gravity of the product oil may be attributed to the existence of higher amounts of TI and NPs in the product oil even after centrifugation, which

over shadowed improvements in °API gravity resulting from lower asphaltenes content (Joshi *et al.* 2008) and/or higher extend of thermal cracking. This conclusion finds support in the viscosity value of the product oil, which was highest in presence of *in situ* NPs, >200,000 cP, relative to the very low viscosity of its maltene, 70 cP, which corresponds to the removal of NPs, coke and asphaltenes. Similarly, the viscosity of the maltene for the *commercial* NPs decreased to 255±50 cP relative to its product oil,  $4.2 \times 10^3 \pm 0.5 \times 10^3$  cP, despite the accompanied evaporation of the lighter ends. The lower viscosity and the higher lighter fractions, as evident from SimDist result in Figure s4.11, suggest higher extend of thermal cracking (Wang *et al.* 2009) in presence of the NPs.

In summary, in presence of *commercial* and *in situ* Al<sub>2</sub>O<sub>3</sub> NPs an improvement in the °API gravity and the viscosity of the maltene at the expense of lower maltene yield and higher TI yield is observed. In light of these results and considering the similarity in the energy consumption between the control and the samples containing NPs, it is concluded that Al<sub>2</sub>O<sub>3</sub> NPs promoted the thermal cracking reactions.

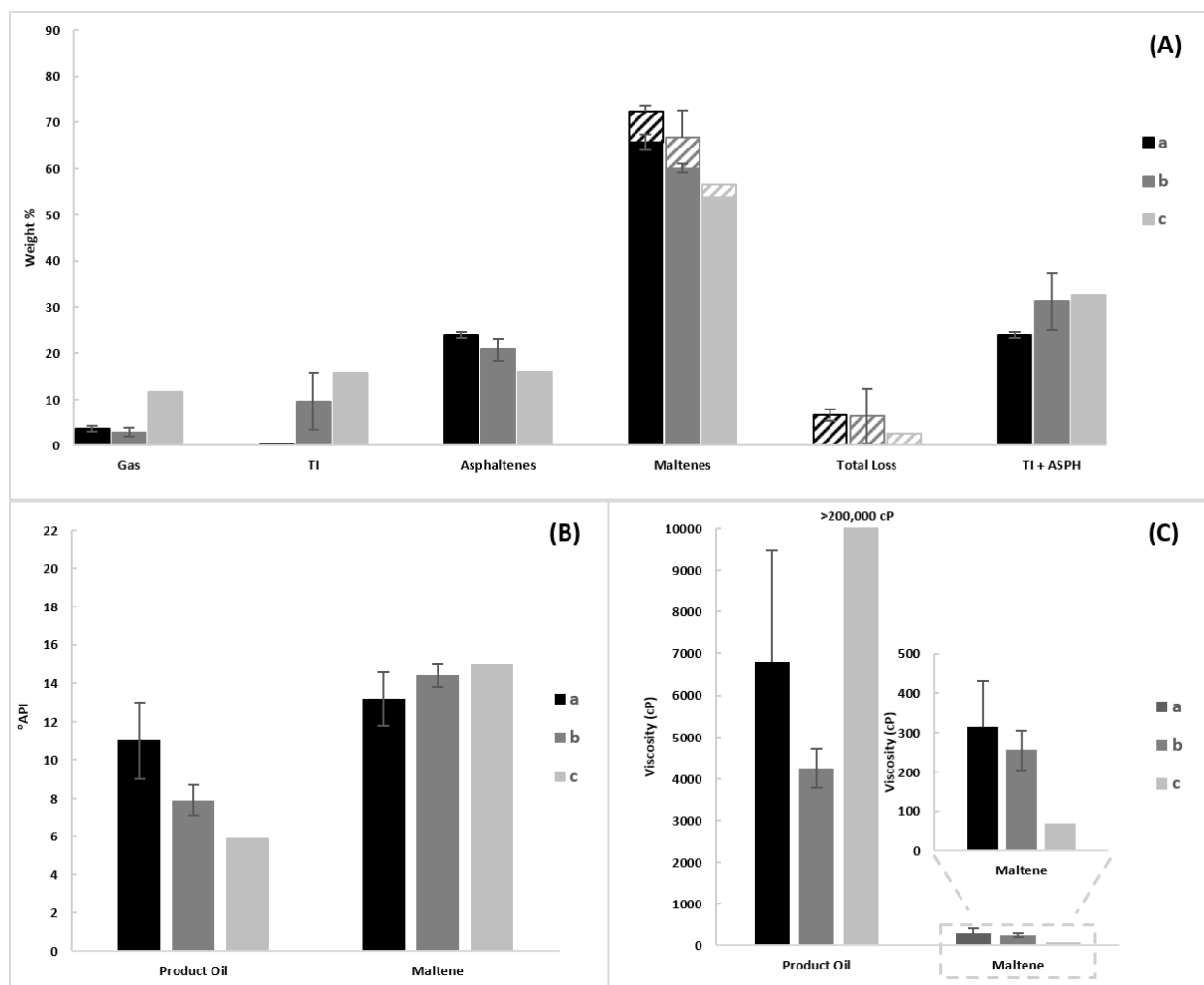


**Figure 4.8:** Product yield (A) °API gravity of the product oil and maltene (B), Viscosity at 37°C of the product oil and the maltene product (C) for thermal cracking at 400°C of (a) AVR, (b) AVR with 10,000 ppm *commercial* NP, and (c) AVR with 6,000 ppm *in situ* NPs.

#### 4.4.3 Effect of Drill Cuttings (DC) on the yield and product quality

Previous studies reported that the presence of fine solids in oil inhibits coke formation (Sanaie *et al.* 2001; Tanabe & Gray 1997; Nhieu *et al.* 2016). In principle, the presence of DC can suppress TI formation by stabilizing the coke precursors either by adsorbing at the coke precursors or through being encapsulated with the coke precursors and asphaltenes (Tanabe & Gray 1997; Sanaie *et al.* 2001). DC encapsulation provides more dispersion for the coke precursors throughout the oil phase allowing for more contact with hydrogen donor compounds, which ultimately

decreases the rate of dehydrogenation and polymerization of coke precursors. On the other hand, if DC adsorb at the interface between the liquid phase and the coke precursor, the aggregation and growth of the coke precursors, which is responsible for TI formation, would be inhibited (Sanaie *et al.* 2001; Tanabe & Gray 1997). Contrary to the above role of suppressing coke formation, DC may promote coke formation through providing higher surface area to increase the probability of the bimolecular reaction. Similar role has been reported for reservoir sand on the pyrolysis of Athabasca bitumen (Murugan *et al.* 2012).

In order to explore the effect of DC on the thermal cracking of AVR, cracking reactions at 400°C using 10 wt%, 20 wt% and 30 wt% DC were performed under 500 rpm of mixing. Cracking reactions at 420°C and 500 rpm mixing using 10 wt% DC were also explored.

The energy consumption and pressure variation during the reaction are given in Figure s4.9 of the supporting material. There is a general increase in the pressure buildup in presence of DC, which was more pronounced for the 30 wt% DC. This could be attributed to a higher surface area in presence of more DC, which in turn, contributed to a higher extent of cracking reactions and evolution of gaseous product. The total energy consumption and the final pressure inside the reactor after cooling are given in Table s4.2. Approximately, 9% lower energy consumption was encountered in presence of DC, and a lower final pressure after cooling was recorded for the samples containing 10 wt% and 20 wt% DC. It appears that DC provided a different reaction path that contributed to more volatiles. Since Figure 4.9(A) shows lower total losses during solvent evaporation for the samples containing 10 wt% and 20 wt% DC, it is concluded that these volatiles possessed longer chain than what may evaporate with toluene and *n*-heptane. On the other hand, the final pressure inside the reactor after cooling is much higher for the 30 wt% DC, which suggests more non-condensables and coke formation (Martínez-Escandell *et al.* 1999). Figure 4.9(A)

confirms that increasing DC concentration to 30 wt% leads to less maltene fraction and more total loss during solvent evaporation, suggesting shorter chain volatiles. Inline with this observation, TI increased at the expense of asphaltenes for the same sample, where  $7\pm 6$  wt% reduction in the asphaltenes and a  $10\pm 2$  wt% increase in the TI, relative to the control run, was encountered. These observations suggest a catalytic role for DC, which appears to accelerate the formation of mesophase in the immediate contact of the catalyst (Marsh *et al.* 1999).

In presence of 10 wt% DC,  $3.2\pm 0.2$  wt% lower TI and  $6.7\pm 0.7$  wt% more asphaltenes were produced relative to control run. This observation is inline with literature observations that suggest an increase in asphaltenes fraction is associated with suppression of coke production (Tanabe & Gray 1997). At this concentration, DC appear to have inhibited the transformation of asphaltenes into TI (Tanabe & Gray 1997). Decreases in TI product during thermal cracking can be achieved through hydrogenating the free radicals ( Del Bianco, Panariti, Anelli, *et al.* 1993) by exposing the TI precursors in contact with potential hydrogen donors within the oil or through preventing radical polymerization via adsorption (Tanabe & Gray 1997). Figure 4.5 and related discussion suggest that DC encapsulation by the coke precursors was likely the major mechanism here. Nevertheless, analysis of H/C ratio of TI samples in presence and absence of DC, discussed later, suggests no major hydrogenation took place.

There is no discernible difference between the °API gravity of the product oil in presence of 0, 10, and 20 wt% DC as shown in Figure 4.9(B), whereas, for the sample containing 30 wt% DC the °API gravity doubled. In addition to a higher extent of thermal cracking, the °API gravity measurement for the sample having 30 wt% DC is most likely influenced by the removal of most of the heavy fractions along with the centrifuged solids. This conclusion is supported by the fact that the °API gravity of the product maltene for experiments in presence of 10 wt% DC improved

by  $53\pm 7\%$  compared to the control experiment and was higher than in presence of 30 wt% DC. For experiments having 20 wt% and 30 wt% DC, higher amount of volatiles formed relative to the samples containing 10 wt% DC, which were lost during solvent evaporation. This in turn, depreciated the °API gravity of the maltene product for the experiments containing 20 wt% and 30 wt% DC relative to the 10 wt% DC sample. The viscosity of the maltene fraction decreased in presence of DC to  $110\pm 20$  cP, 210 cP, and  $70\pm 40$  cP for thermal cracking with 10, 20, and 30 wt% DC, respectively, as per Figure 4.9(C). As explained above, the removal of the heavy fractions along with the centrifuged solids could have also resulted in lower viscosity of product oil in presence of 30 wt% DC.

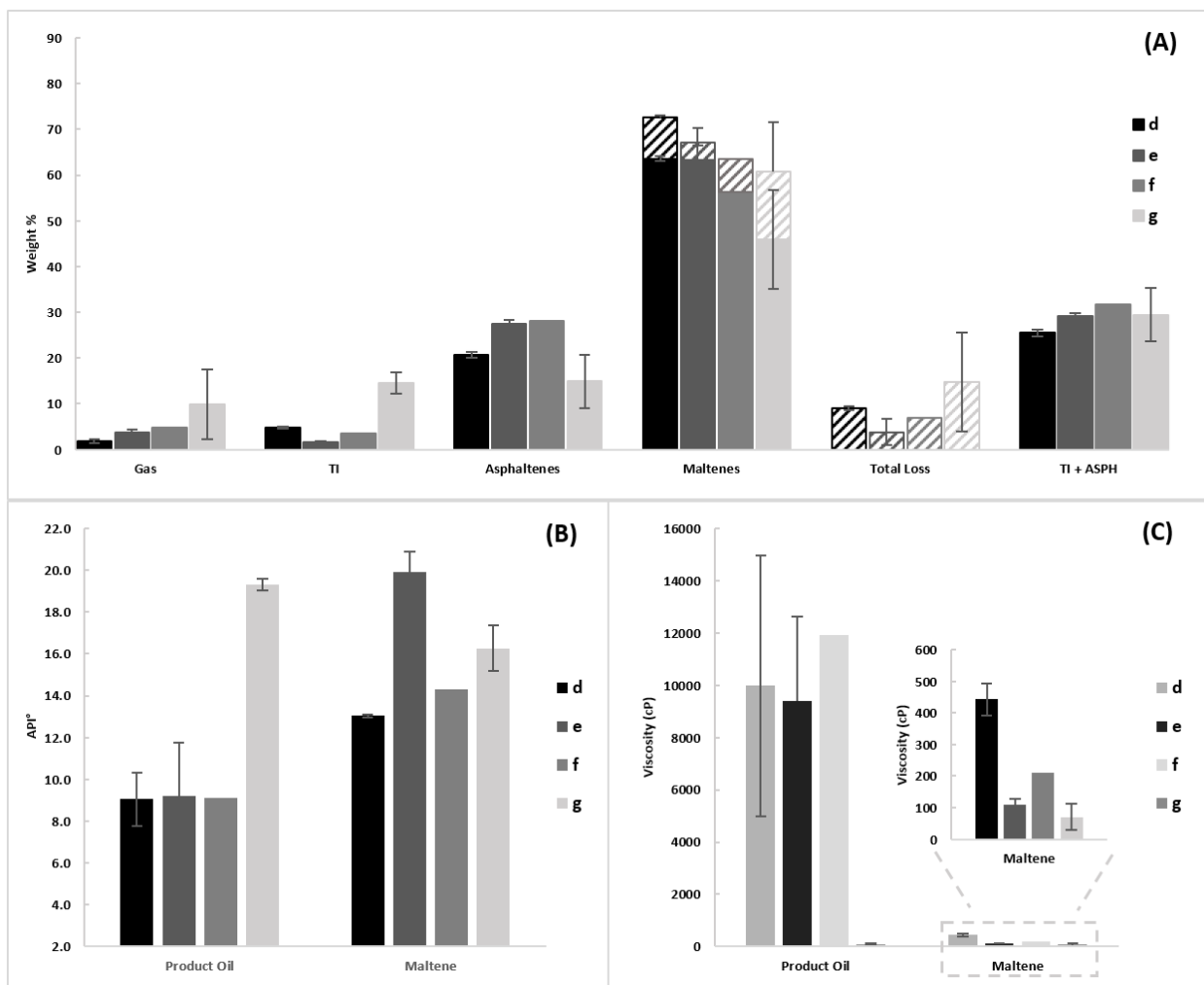


**Figure 4.9:** Product yield (A), °API gravity of the product oil and maltene (B), viscosity at 37°C of the product oil and the maltene product (C) for thermal cracking at 400°C of (d) AVR, (e) AVR with 10 wt% DC, (f) AVR with 20 wt% DC, and (g) AVR with 30 wt% DC.

The results from thermal cracking in presence of DC at 400°C revealed highest product quality at 10 wt% DC amongst the concentrations tested. Therefore, a higher thermal cracking temperature; namely 420°C, was explored in presence of 10 wt% DC.

The pressure and the total energy input to the reactor are given in Figure s4.10. In presence of 10 wt% DC gases were produced more rapidly coupled with  $6.1 \pm 0.8\%$  reduction in the total energy input to the reactor compared with the control experiment. This, again, confirms a catalytic role for DC manifested by selecting a reaction path which accelerates gas formation. On the other

hand, Table s4.1 shows 8% lower final pressure after cooling in presence of DC relative to the control sample. The trend in the pressure during reaction and after cooling suggests more volatile products, but less non-condensables. Unlike upgrading at 400°C, these volatiles evaporated during solvent removal, leading to  $11.7 \pm 2.7$  wt% higher total loss as reported in Figure 4.10(A), compared to control run. In presence of DC,  $3 \pm 0.3$  wt% less asphaltenes and  $3 \pm 2$  wt% more maltene were obtained, which suggests an inhibiting effect toward maltene conversion reactions to asphaltenes and/or increasing effect toward conversion of asphaltenes to maltene (Yasar *et al.* 2001; Trauth *et al.* 1986) as shown in Figure 4.10(A). In general, an increase in the maltene product during upgrading results from inhibiting the condensation and polymerization reaction of the radicals (Liu *et al.* 1994; Tian *et al.* 1998). The quality of the liquid product is depicted in Figure 4.10(B,C). Lower rate of polymerization reactions resulted in a decrease in the viscosity of product oil relative to the control sample in presence of DC. In addition, increase in the °API gravity of product oil is consistent with the shift in the SimDist result of the product oil in presence of DC to a lower boiling point, as shown in Figure s4.11, which is also consistent with the formation of more volatiles as in Figure 4.10(A). At 420°C, the presence of DC did not introduce notable changes in °API gravity and viscosity of the product maltene relative to the control sample, probably due to the loss of most of the volatile components during solvent evaporation.

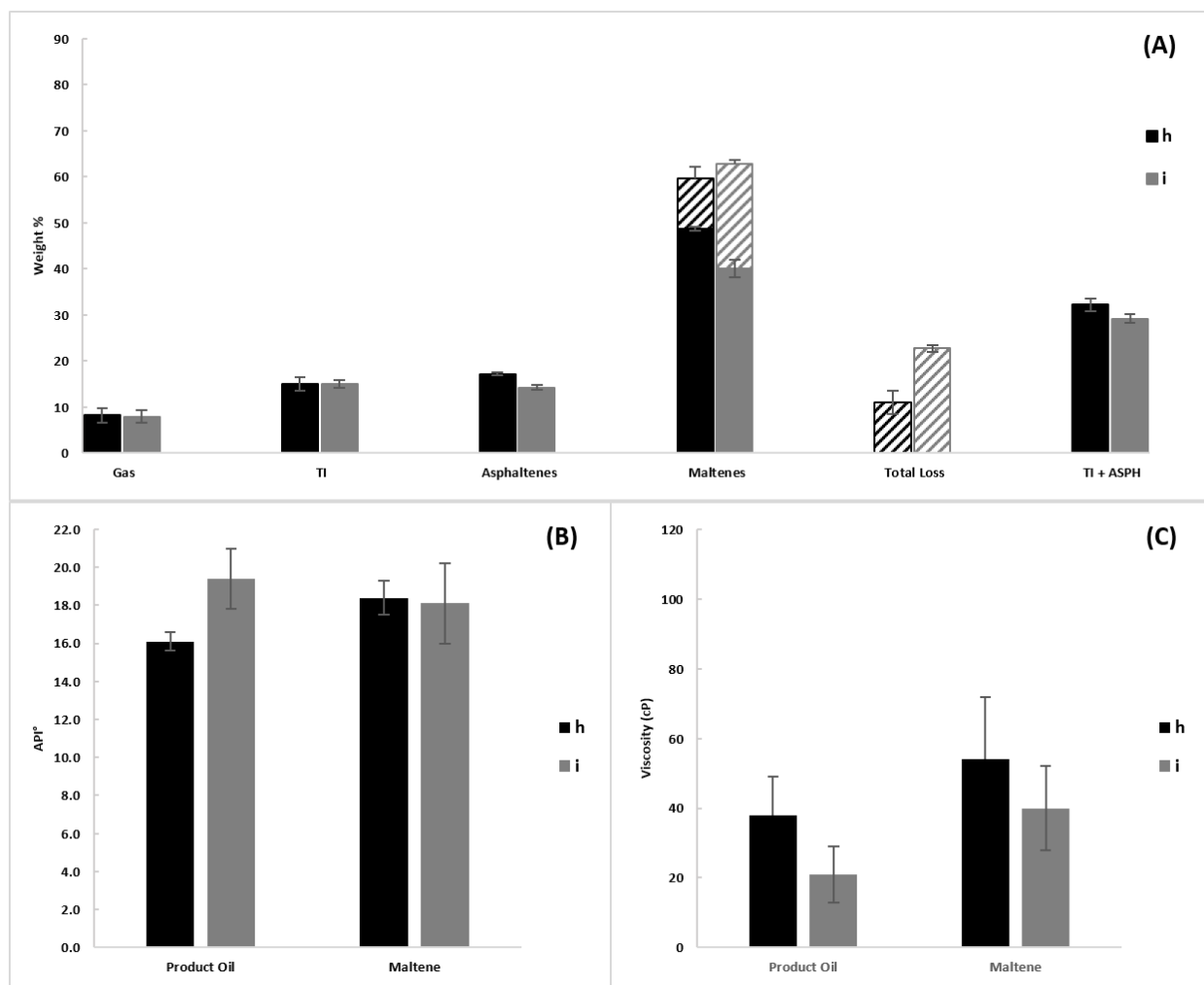


**Figure 4.10:** Product yield (A), °API gravity of the product oil and maltene (B), Viscosity at 37°C of the product oil and the maltene product (C) for thermal cracking at 420°C of: (h) AVR, (i) AVR with 10 wt% DC.

In general, increasing the temperature of thermal cracking, increases the rate of coke formation (Al-Marshed *et al.* 2015). A comparison between thermal cracking at 400°C and 420°C in presence of 10 wt% DC reveals higher amounts of TI at 420 °C, which formed at the expense of asphaltenes. This could be due to precipitation of asphaltenes at higher thermal cracking temperatures leading to ineffective hydrogen transfer (Al-Marshed *et al.* 2015). The °API gravity of the product oil was higher for thermal cracking at 420°C compared to 400°C. This is probably due to higher extent upgrading coupled with elimination of the heavier liquid product which most

likely separates as part of the centrifuge bottom while separating the solids. On the other hand, higher temperature improved cracking reactions and produced more volatiles, which evaporated during solvent removal and resulted in decreasing the °API gravity of the maltene product at 420°C relative to 400°C.

To summarize the role of the additives, the effect of NP appears similar to the effect of DC at its highest concentration, 30 wt%, by virtue of the huge surface area available in both cases. This conclusion finds support in the following facts. There is 80±50 psi increase in the final pressure of the reactor in present of 30 wt% drill cuttings and 73±8 psi increase in presence of *in situ* NPs compared to their control samples. TI increased by 9.7±2.3 wt%, 9.5±6.2 wt% and 15.8±0.1 wt% for thermal cracking in presence of 30 wt% DC, *commercial* NPs and *in situ* NPs, respectively. It is worth noting that energy consumption for thermal cracking in presence of 30 wt% DC is even 11% lower compared with alumina NPs.

In order to quantify the role of the different additives toward thermal cracking of AVR, even roughly, reaction rate constants were compared between control and samples containing the additives following reaction (R4.2) for the conversion of feedstock to TI and gaseous products.



where, *HO* is the heavy oil feedstock consisting of maltene and asphaltenes, *TI* is the toluene insoluble product, and *G* is the gas product. This reaction was assumed to consume the highest energy among the many other reactions taking place (Schobert 1990). As detailed in the supporting material, the linear variation in the energy consumption w.r.t. time suggests zero order reaction for (R4.2). Table 4.3 reveals that mixing and higher temperature increased the rate of conversion to *TI* and gas, which is consistent with our previous work (Eshraghian & Husein 2017) as well as literature finding (Ebrahimi *et al.* 2008; Yue *et al.* 2004). *In situ* prepared NPs displayed the highest

impact on (R4.2) rate of reaction at 400°C, as confirmed by the experimental findings. Nevertheless, one should keep in mind that the value of  $k$  for the *in situ* NPs might be amplified by the endothermic reaction of precursor decomposition, (R4.1). Contrary to the higher concentrations, 10 wt% DC displayed similar value of  $k$  as the control sample for the two temperatures. Figures 4.9(A) and 4.10(A) display similar liquid yield to the control sample in presence of 10 wt% DC, but with much higher quality maltene compared. Overall, NPs had higher impact on (R4.2) rate of reaction which could only be matched at 30 wt% DC.

**Table 4.3:** Reaction rate constants per reaction (R2) for control samples at different operating conditions and their ratios in presence of different additives.

$k_{ctr}(\text{Kg m}^3\text{s}^{-1}) \times 10^2$	1.3 (400°C; 0 rpm)		1.6 (400°C; 500 rpm)			6.4 (420°C; 500 rpm)
Additive	<i>Commercial</i> NPs	<i>In situ</i> NPs	10 wt% DC	20 wt% DC	30 wt% DC	10 wt% DC
$k/k_{ctr}$	2.7	5.9	0.9	1.2	2.9	0.9

#### 4.4.4 H/C and STA analysis of TI and asphaltenes

In order to understand the chemical nature of the different products, H/C ratio of selected thermal cracking products in presence and absence of DC is provided in Figure 4.11. Generally, higher H/C ratio signals lighter hydrocarbon and lower aromaticity (Leyva *et al.* 2013). The higher value of H/C for asphaltenes compared to TI suggests heavier TI hydrocarbon with more aromaticity. TI formed from thermal cracking in presence and absence of DC have almost the same H/C atomic ratio, which suggests that DC affected the rate of TI formation, but probably not so much its chemical nature. Lower H/C ratio of the asphaltenes product compared to the asphaltenes from

feedstock reflects higher aromaticity (Gonçalves *et al.* 2001), which is consistent with thermal cracking products. This reveals that indeed the chemical nature of the products from the thermal cracking reactions are heavy fractions and closer to coke.

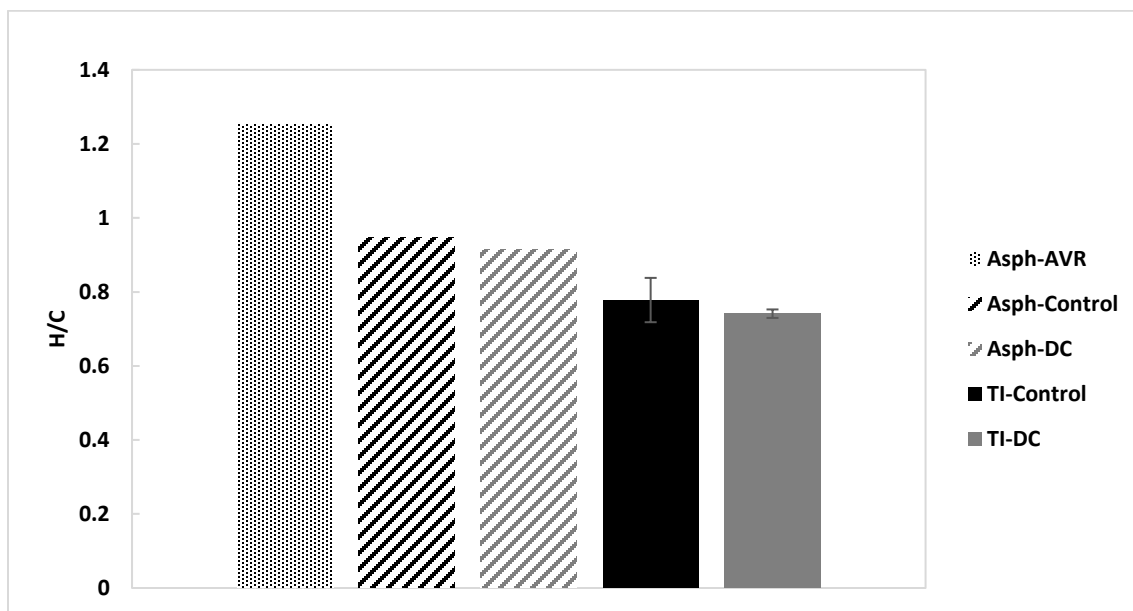


**Figure 4.11:** H/C ratio of TI and asphaltenes product for thermal cracking of control AVR and AVR with 10 wt% DC at 420°C and H/C ratio of original asphaltenes from AVR.

Figure 4.12 portrays the TG and heat flow profiles under air atmosphere of the TI fractions of the control experiment and in presence of 10 wt% DC from thermal cracking at 420°C. While the onset temperature from the heat flow curves appears the same, the reaction was completed at lower temperature for TI in presence of DC. This seemingly faster reaction in presence of DC may arise from a lower reactant mass introduced to the STA in presence of cutting, since the STA sample mass was fixed at 10 mg in both cases. Accordingly, and as indicated in a previous work by our group, fractional conversion,  $\alpha$ , alone may not be the best parameter to employ to identify reaction kinetics using thermogravimetry analysis (Abu Tarboush & Husein 2012b). In addition to smaller reactant mass, in presence of DC the reactants are more exposed to the air stream, as a

result of the larger surface area and more porous structure, which leads to an overall more effective mass and heat transfer and hence more rapid reactions. This explanation finds a root in the narrower heat flow profile for oxidation of TI in presence of DC (Drici & Vossoughi 2013; Mani *et al.* 2010).

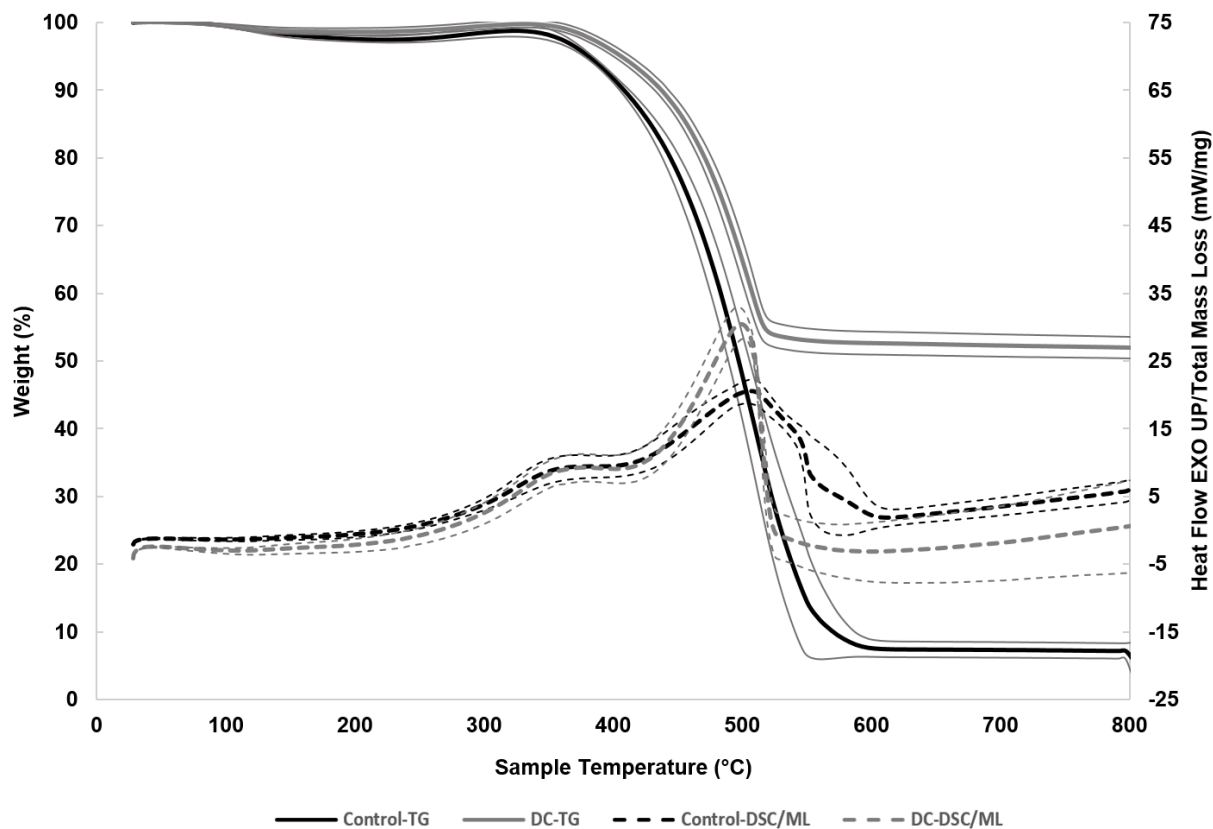


**Figure 4.12:** %Mass loss and heat flow profiles of the TI product for the thermal cracking of control AVR (black) and AVR with 10 wt% DC (grey) at 420°C. Thin lines represent the standard deviation for three replicates.

In order to better understand the roles of the initial mass and heat and mass transfer on the oxidation of STA samples, three different samples of the product asphaltenes from AVR thermal cracking at 420°C with 5, 10, and 15 mg initial mass were run through the STA. Figure 4.13 shows that the %mass loss and the heat flow profiles are indeed affected by the initial mass used and a shift to higher completion temperatures was observed. This observation is inline with previous

work by Abu Tarboush & Husein (Abu Tarboush & Husein 2012b) and Aqsha *et al.* (Aqsha *et al.* 2011).

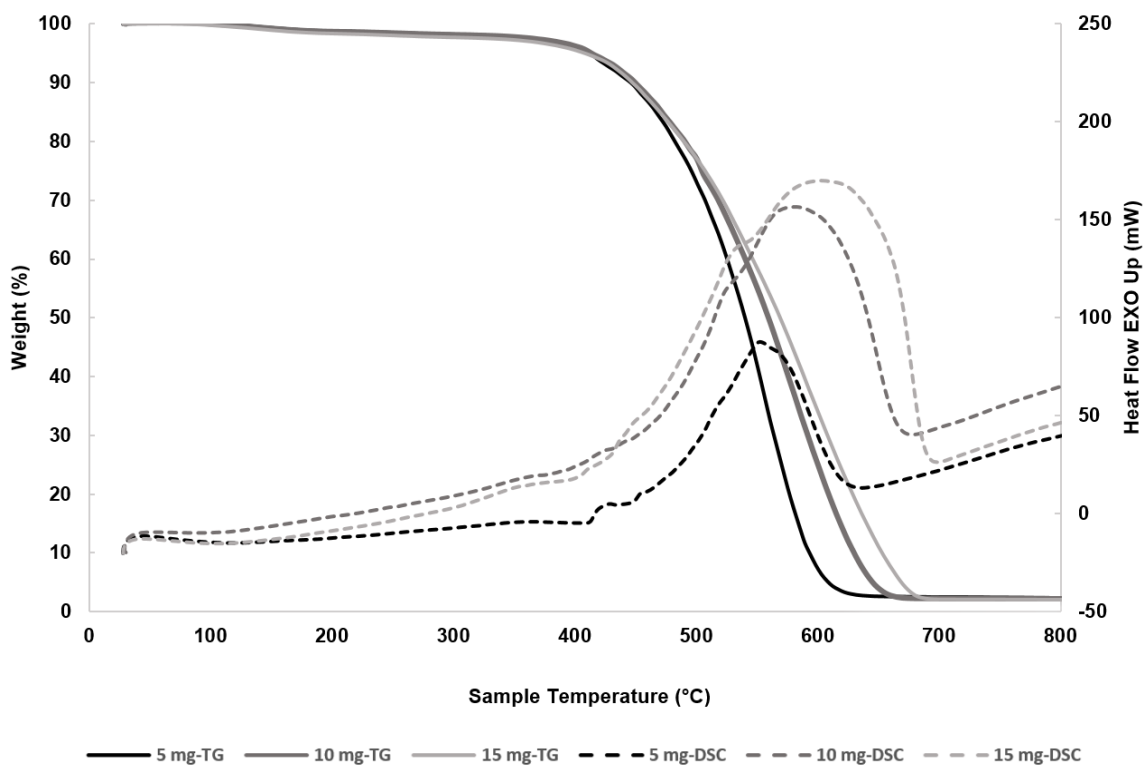


**Figure 4.13:** % Mass loss and heat flow profiles of different initial masses of the asphaltenes fraction from thermal cracking of AVR at 420°C.

#### 4.4.5 HTSD and GC Test Result

The SimDist results of the liquid product and the analysis of the gaseous product in presence and absence of NPs and DC are given in Figure s4.11 and Table s4.3, respectively. The difference between the boiling points between the AVR feed stock and the upgraded sample suggests a good extend upgrading took place. The boiling point of n-C44 (545°C) is considered as the dividing line between the light distillate and the residual components. The conversion of the 545<sup>+0</sup>°C, the residue, for each upgraded sample of thermal cracking was obtained using E4.1 below.

$$Conv_{545^{\circ}C} = \frac{Mass\ of\ 545^{\circ}C_{feed} - Mass\ of\ 545^{\circ}C_{Product}}{Mass\ of\ 545^{\circ}C_{feed}} \times 100\% \quad (E4.1)$$

The calculation, of course, is based on the product of the upgraded sample and ignores the mass of the catalyst additive. The conversion of the residue, 545<sup>°</sup>C, for different samples is presented in Figure 4.14. The upgraded sample at 400<sup>°</sup>C in absence and presence of *in situ* NPs and the upgraded sample at 420<sup>°</sup>C in absence and presence of DC display 34 wt%, 45 wt%, 52 wt%, and 54 wt% conversion of the residue, respectively, compared to the feed stock. The radical cracking, main possible explanation for the conversion of the residue to lighter fractions (Carbognani *et al.* 2007; Ebrahimi *et al.* 2008), became pronounced in presence of the catalysts. This conversion relative to control samples is more pronounced for NPs compared to DC.

After cooling the reactor, C4<sup>+</sup> in the gaseous product is anticipated to condense at the final pressure of the reactor vessel. The weight fraction of the condensable gaseous product based on the gas analysis of Table s4.2 is included in Figure 4.14. Higher percent of condensable gases was obtained in presence of the *in situ* NPs. If one couples the trend in the percent condensable gas with that of total losses due to solvent evaporation, it becomes clear that in presence of the catalyst additives different reactions paths were selected.

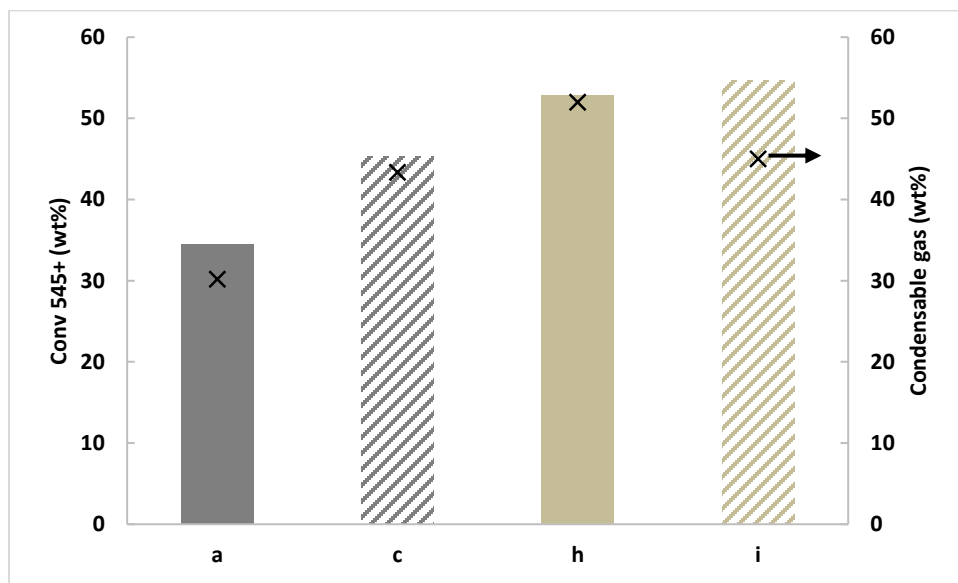


**Figure 4.14:** Conv 545<sup>+</sup> and condensable gas wt% of products from thermal cracking of AVR (a) at 400°C and 0 rpm control (c) at 400°C and 0 rpm containing *in situ* NPs; (h) at 420°C control and 500 rpm, (i) at 420°C and 500 rpm containing 10 wt% DC. Condensable gas wt% is based on the gas sample.

#### 4.5 Conclusions

The catalytic thermal cracking of Athabasca vacuum residue (AVR) in presence of *in situ* prepared and *commercial* Al<sub>2</sub>O<sub>3</sub> nanoparticles (NPs) as well as drill cuttings (DC) within a closed reactor arrangement was investigated. Spherical *in situ* Al<sub>2</sub>O<sub>3</sub> NPs were obtained with a mean particle diameter of 90±80 nm. There is evidence of higher extent upgrading in presence of the NPs, especially *in situ*, e.g. higher gas fraction, lower viscosity and higher °API gravity of the maltene product and higher conversion of the residue. Nevertheless, NPs could not inhibit the formation of toluene insolubles (TI) to the same extent as an optimized dose of drill cuttings (DC), i.e. 10 wt%. NPs, especially *in situ* Al<sub>2</sub>O<sub>3</sub>, were rather engulfed into the TI fraction by virtue of their very small particle size. In contrast, DC inhibited coke formation by dispersing coke precursors, which led to an overall more porous TI structure. A higher temperature run at 420°C was tested in presence of 10 wt% DC, which revealed higher TI formation relative to the sample at 400°C. There is higher

amount of maltene formation in presence of DC at 420°C, however at the expense of asphaltenes, while similar TI yield was obtained suggesting inhibition of maltene conversion to asphaltenes in presence of DC. Moreover, presence of DC contributed to 11% and 6% reduction in total energy consumption for the runs at 400°C and 420°C, respectively, which suggests a catalytic role and selectivity of a different reaction path in light of the product yield and quality. At the highest concentration of DC, 30 wt%, trends similar to those recorded for the NPs in terms of lower maltene product and more TI were reported. Elemental analysis showed that there is no significant difference between the H/C ratio of the TI produced in presence and absence of DC.

#### **4.6 Acknowledgment**

The authors would like to thank the Natural Sciences and Engineering Research Council of Canada (NSERC) for the financial support, Ms. Tong Xu and Mr. Thomas Albert Kaminski for helping in running part of the experiments, Dr. Mohsen Zirrahi for helping in gas chromatography analysis, and Executive Mat Service (Calgary, AB) for donating the drill cuttings.

## 4.7 Supporting material

### 4.7.1 Scherrer's equation

The Scherrer's equation (Mirzayi & Shayan 2014) to estimate the mean Al<sub>2</sub>O<sub>3</sub> crystal size from the XRD peak:

$$D = \frac{k \lambda}{\beta \cos \theta} \quad (\text{E s4.1})$$

where  $k= 0.9$  is the shape factor and Scherrer's constant,  $\lambda=0.154$  nm is the X-ray wavelength,  $\theta$  is the diffraction angle in degree ( $\theta= 67.08/2$ ) and  $\beta$  is the peak width at half the maximum intensity of the selected peak (Mirzayi & Shayan 2014).

### 4.7.2 Catalyst Characterization

**Table s4.1:** particle size and geometric surface area calculated from TEM and SEM images of different samples

	Particle size (XRD) <sup>a</sup> (nm)	Surface area (XRD) (m <sup>2</sup> /g)	Particle size (SEM) (nm)	Surface area (SEM) (m <sup>2</sup> /g)	Particle size (TEM) (nm)	Surface area (TEM) (m <sup>2</sup> /g)
As received <i>Commercial</i> NPs	4.5	336.7	–	–	13±8 Fig. s1(b) <sup>b</sup> 33 <sup>c</sup>	109
TI with <i>Commercial</i> Nps	5	303	720±490 Fig. 1(e) <sup>b</sup> 57 <sup>**</sup>	1.1	–	–
Leftover TI with <i>Commercial</i> NPs of STA	–	–	390±280 Fig. 1(h) <sup>b</sup> 30 <sup>c</sup>	2	–	–
TI with <i>in situ</i> NPs	–	–	1400±4200 Fig. 2(d) <sup>b</sup> 47 <sup>c</sup>	0.08	850	1.8
Leftover TI with <i>in situ</i> NPs of STA	–	–	90±80 Fig. 2(g) <sup>b</sup> 83 <sup>c</sup>	3.23	–	–

<sup>a</sup> Calculated from Scherrer's equation

<sup>b</sup> Corresponding particle size distribution histogram is presented in mentioned figure

<sup>c</sup> Number of analyzed particles in sample

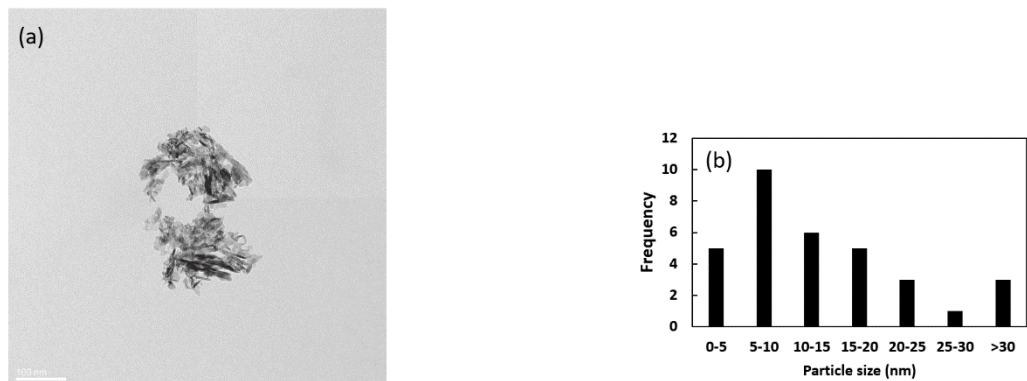


**Figure s4.1:** (a) TEM image and (b) corresponding particle size distribution histogram of as received *commercial*  $Al_2O_3$  NPs employed in this study.

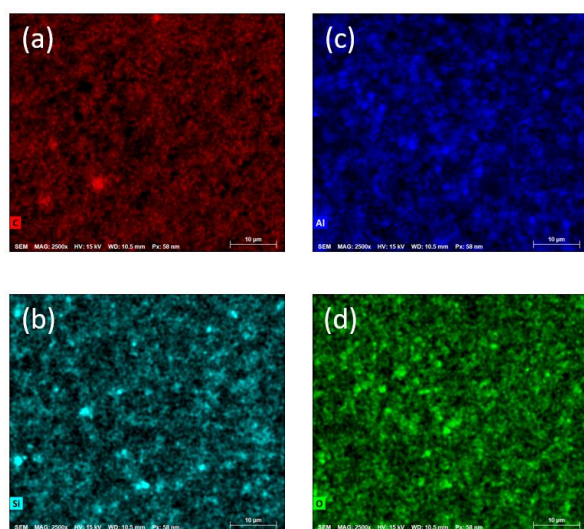


**Figure s4.2:** (a) SEM image with C EDX mapping, (b) SEM image with Si EDX mapping, (c) SEM image with Al EDX mapping, and (d) SEM image with O EDX mapping of TI following thermal cracking of AVR in *commercial*  $Al_2O_3$  NPs employed in this study.

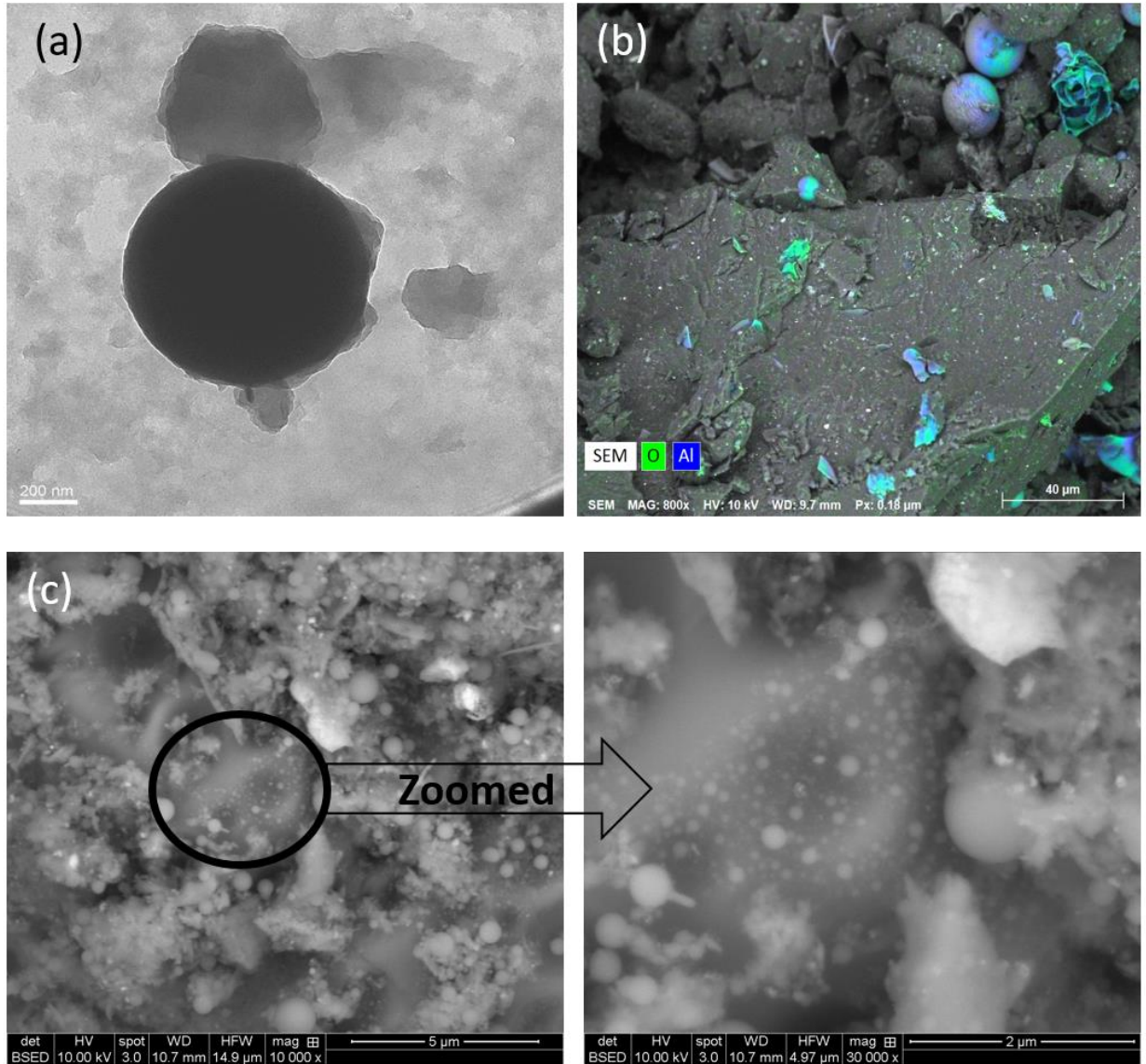


**Figure s4.3:** (a) TEM, (b) SEM photograph with EDX mapping of Al and O of TI following thermal cracking of AVR in presence of *in situ* Al<sub>2</sub>O<sub>3</sub> particles and (c) SEM image of left over material from STA heat treating of TI following thermal cracking of AVR in presence of *in situ* prepared Al<sub>2</sub>O<sub>3</sub> NPs at 400°C.

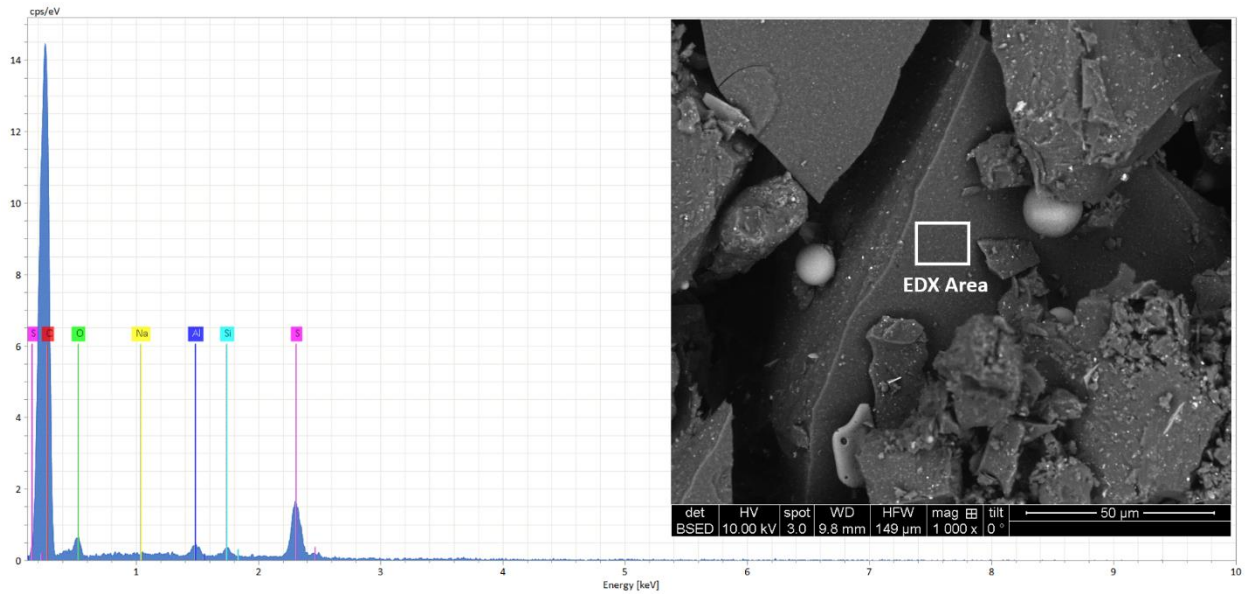


**Figure s4.4:** EDX pattern and corresponding SEM photograph, TI following thermal cracking of AVR in presence of *in situ* Al<sub>2</sub>O<sub>3</sub> particles at 400°C

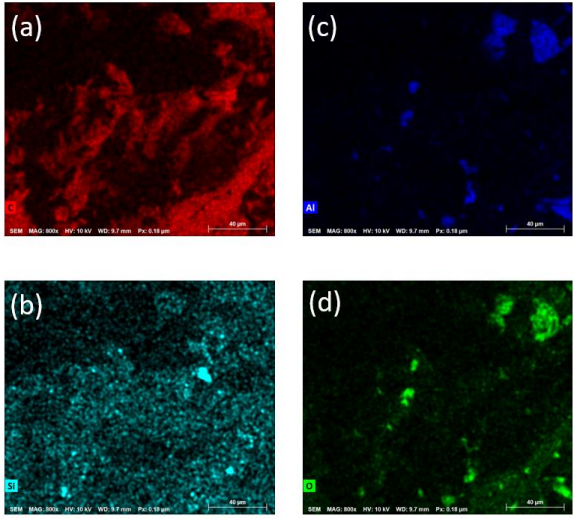


**Figure s4.5:** (a) SEM image with C EDX mapping, (b) SEM image with Si EDX mapping, (c) SEM image with Al EDX mapping, and (d) SEM image with O EDX mapping of TI following thermal cracking of AVR in presence of *in situ* Al<sub>2</sub>O<sub>3</sub> particles at 400°C

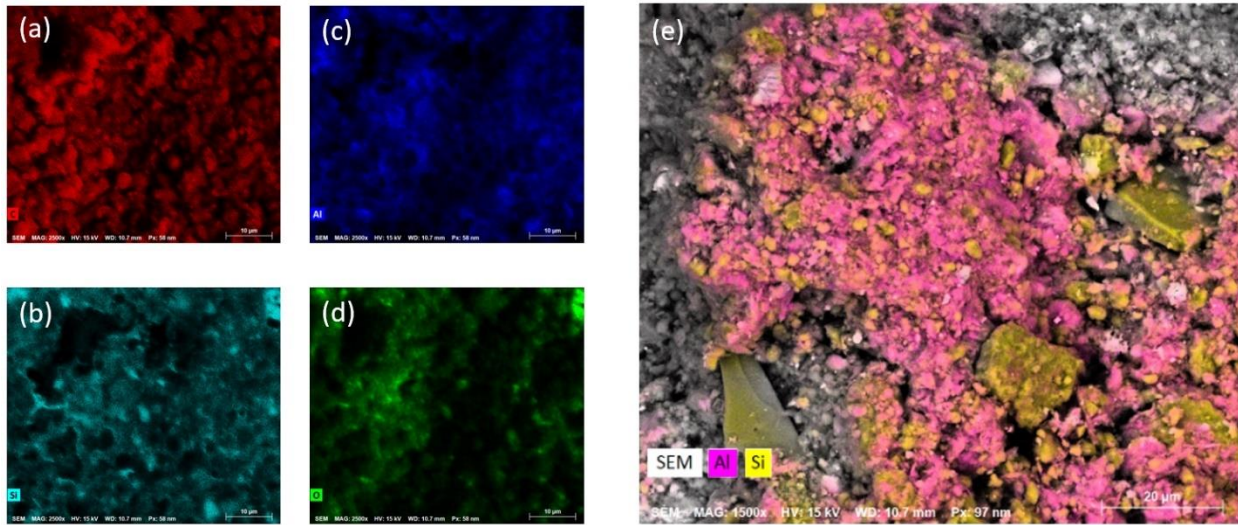


**Figure s4.6:** (a) SEM image with C EDX mapping, (b) SEM image with Si EDX mapping, (c) SEM image with Al EDX mapping, and (d) SEM image with O EDX mapping of TI following thermal cracking of AVR 420°C in presence of 10 wt% DC, (b) SEM photograph with Al and Si EDX mapping of left over material of STA analysis of TI following thermal cracking of AVR in presence of 10 wt% DC at 420°C

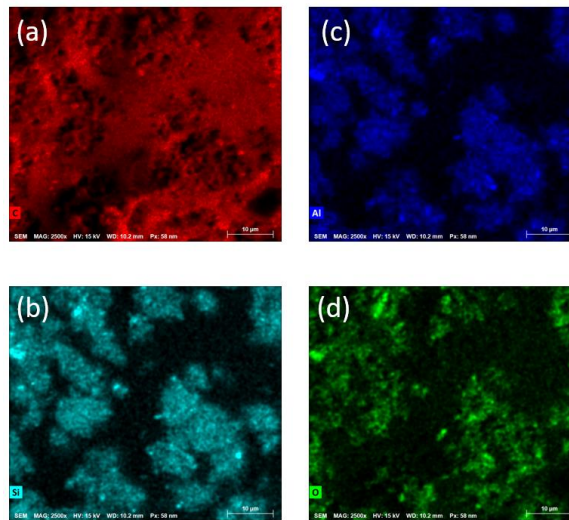


**Figure s4.7:** (a) SEM image with C EDX mapping, (b) SEM image with Si EDX mapping, (c) SEM image with Al EDX mapping, and (d) SEM image with O EDX mapping of TI following thermal cracking of AVR in presence at 420°C.



$$Z_{O_2} = 1 \text{ (assumed)}$$

$$y_{NO_2} = y_{NO} = y_{O_2} = 1/3$$

$$Z_{\text{total}} = y_{NO_2} \times Z_{NO_2} + y_{NO} \times Z_{NO} + y_{O_2} \times Z_{O_2} = 0.997$$

$$Z = \frac{pV}{nRT} \implies P = \frac{ZnRT}{V}$$

$$Z = 0.997$$

$$n = 0.026$$

$$R = 8.314 \frac{\text{L KPa}}{\text{K mol}}$$

$$T = 400 \text{ }^\circ\text{C} + 273.15 = 673.15 \text{ K}$$

$$V = 0.05 \text{ L}$$

$$P = \frac{0.997 \times 0.026 \text{ mol} \times 8.314 \frac{\text{L KPa}}{\text{K mol}} \times 673.15 \text{ K}}{0.05 \text{ L}} \times \frac{0.145038 \text{ psi}}{1 \text{ KPa}} = 425 \text{ psi}$$

#### 4.7.4 Energy consumption and pressure build up

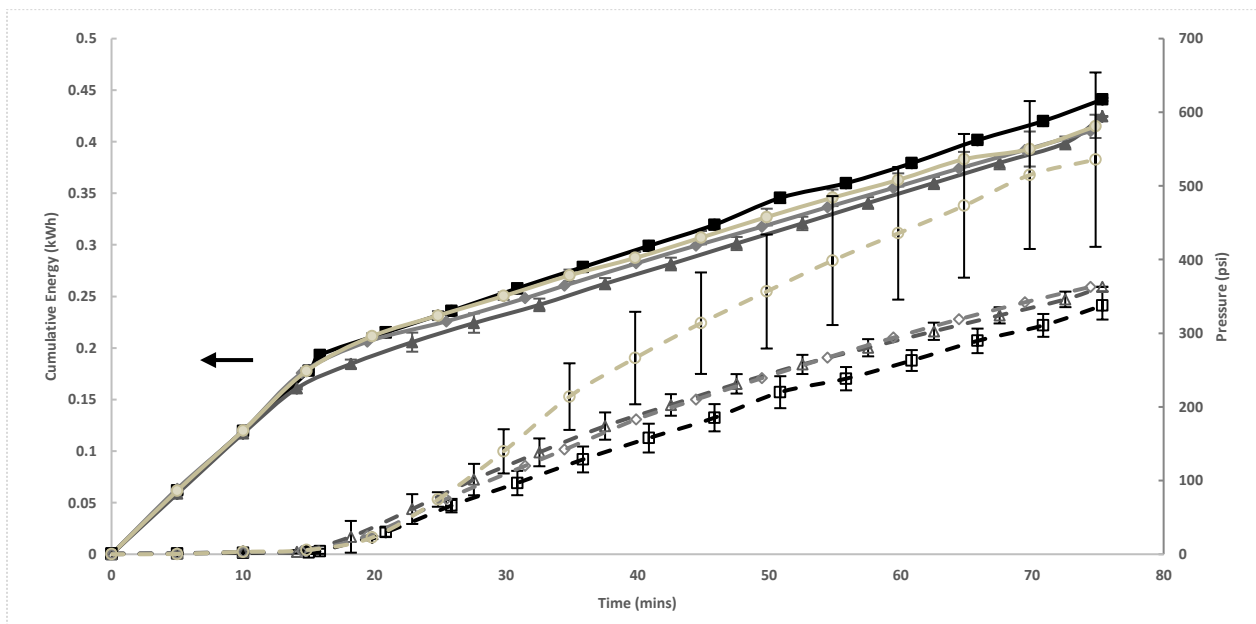


**Figure s4.9:** Energy consumption and pressure buildup inside the batch reactor during the thermal cracking at 400°C of: (■, □) AVR, (▲, △) AVR with 10 wt% DC, (◆, ◇) AVR with 20 wt% DC, (●, ○) AVR with 30 wt% DC.

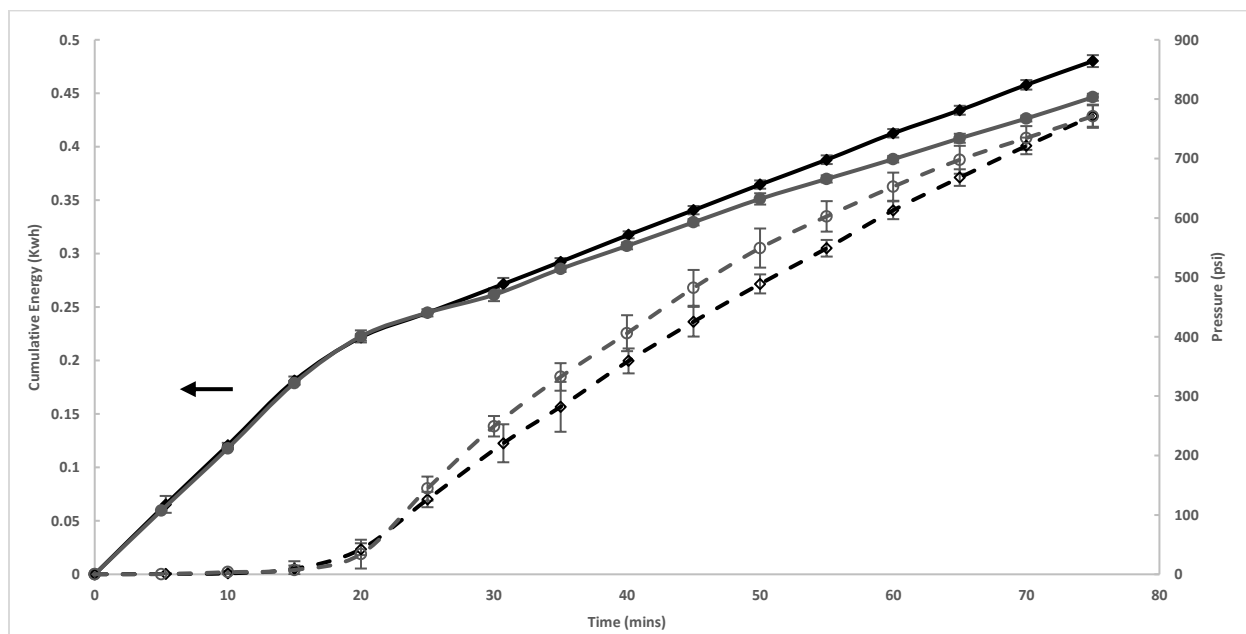


**Figure s4.10:** Energy consumption and pressure buildup inside the batch reactor during the thermal cracking at 420°C of: (♦,◇) AVR and (●,○) AVR with 10 wt% DC.

**Table s4.2:** The overall energy input to the reactor and the final pressure after cooling for thermal cracking of AVR at different reaction temperature and DC content.

DC wt%	Cumulative Energy (kWh)	Final Pressure after cooling (psi)
1) At 400°C		
0	0.44±0.01	149±10
10	0.41±0.01	126±13
20	0.41	118
30	0.41±0.01	227±46
2) At 420°C		
0	0.475±0.004	346±17
10	0.446±0.003	318±16

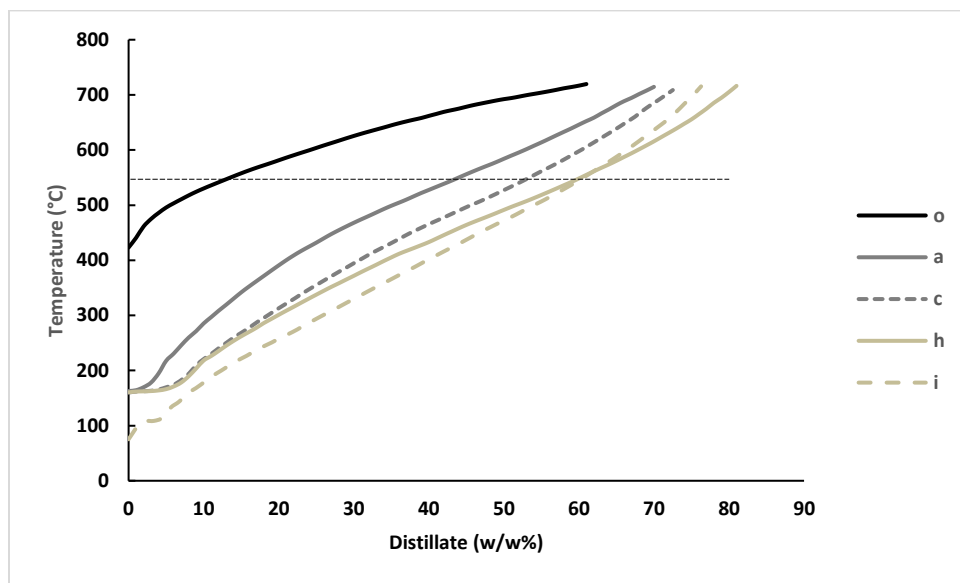


**Figure s4.11:** High-temperature simulated distillation curves of (o) AVR, (a) product oil from thermal cracking of AVR at 400°C and 0 rpm (c) product oil from thermal cracking of AVR at 400°C and 0 rpm containing in situ NPs, (h) product oil from thermal cracking of AVR at 420°C and 500 rpm, (i) product oil from thermal cracking of AVR at 420°C and 500 rpm containing 10 wt% DC.

**Table s4.3:** Analysis of gaseous product from thermal cracking of AVR at (a) 400°C control; (c) 400°C containing in situ NPs; (h) 420°C control; (i) 420°C containing 10 wt% DC.

Gas	a		c		h		i	
	Wt%	Mol%	Wt%	Mol%	Wt%	Mol%	Wt%	Mol%
C1	15.6	37.0	11.6	31.3	3.2	11.1	9.7	27.6
C2	18.8	23.7	12.6	18.2	8.0	14.8	11.5	17.4
C3	18.4	15.8	17.0	16.7	16.7	20.9	16.5	17.0
C4	17.0	11.1	15.5	11.5	20.1	19.1	17.3	13.5
C5	11.2	5.9	15.0	9.0	18.2	13.9	15.6	9.9
C6	9.3	4.1	14.6	7.3	18.1	11.6	16.4	8.6
C7	6.2	2.4	13.7	5.9	15.7	8.7	13.0	5.9

#### 4.7.5 Reaction rate constant calculations

Nomenclature:

HO: heavy oil (maltene and asphaltenes)

TI: toluene insoluble

G: gas

t= reaction time (s)

$r_{HO}$  = rate of HO conversion ( $\frac{kg}{m^3 s}$ )

k: reaction rate constant ( $\frac{kg}{m^3 s}$ )

$C_{HO}$ : HO concentration ( $\frac{kg}{m^3}$ )

$C_{HOi}$ : initial concentration of HO ( $\frac{kg}{m^3}$ )

$C_{HOt}$ : concentration of HO at time t ( $\frac{kg}{m^3}$ )

$m_{HO}$ : HO mass (kg)

$m_{HOi}$ : initial mass of the HO (kg)

$m_{HOt}$ : mass of HO at time t (kg)

$\dot{E}_{rxn}$ : rate of reaction energy consumption ( $\frac{kJ}{s}$ )

$E_{rxn}$  = reaction energy (kJ)

$\Delta E_{in}$  : total energy consumption (kWh)

$\dot{Q}_{Loss}$ : rate of energy loss ( $\frac{kWh}{min}$ )

$\Delta H_{rxn}$  = enthalpy of reaction ( $\frac{kJ}{kg}$ )

Starting from the following reaction of conversion of maltene and asphaltenes (HO) to gas (G) and toluene insoluble (TI):



∴ Cumulative energy supplied to the reactor varies linearly with time. Also, since  $\dot{E}_{rxn}$  can be written from Es1,

$$\dot{E}_{rxn} = r_{HO} \times \Delta H_{rxn} \times V \quad (\text{Es4.1})$$

Finally, assuming constant volume of reaction mixture, then the rate of reaction,  $r_{HO}$ , must be constant, i.e.

$$-r_{HO} = k = \frac{m_{HO\ i} - m_{HO\ t}}{V \times \Delta t}$$

Since batch reactor is used, the above equation also applies as the reactor design formula.

Subsequently, the energy per time needed to carryout the endothermic reactions:

$$\dot{E}_{rxn} = r_{HO} \times \Delta H_{rxn} \times V = k \times \Delta H_{rxn} \times V$$

$$\therefore E_{rxn} = E_{in, Zone\ II} - Q_{loss, Zone\ II} = \int_0^t (k \times \Delta H_{rxn} \times V) dt = k \times \Delta H_{rxn} \times V \times t \quad (\text{Es4.2})$$

$$\Delta H_{rxn} = \frac{E_{rxn}}{k \times V \times t} = \frac{E_{rxn}}{m_{HO\ i} - m_{HO\ t}}$$

Equation (Es4.2) assumed all energy supplied during thermal cracking, i.e. Zone II, all goes toward reaction (Rs4.1) and heat losses as well as constant volume of the reaction mixture. Assuming  $Q_{loss, Zone\ II}$  can be modelled as natural convection from the surface of the mantle, see supporting material of Eshraghian and Husein [2].  $\dot{Q}_{Loss}$  from the surface of the mantle at 400 °C is  $0.003 \frac{kWh}{min}$ .

Similarly,  $\dot{Q}_{Loss}$  at 420 °C was calculated  $0.0037 \frac{kWh}{min}$ .

Sample calculations for *commercial* NPs run:

$$m_{HO\ i} = 50\text{ g}, m_{HO\ t} = 43.7\text{ g}, V = 50\text{ ml} = 5 \times 10^{-5}\text{ m}^3, t = 60\text{ min}$$

$$m_{HO\ i} - m_{HO\ t} = 50\text{ g} - 43.7\text{ g} = 6.3\text{ g} = 0.0063\text{ kg}$$

$$k = \frac{m_{HO\ i} - m_{HO\ t}}{V \times \Delta t} = \frac{0.0063\text{ kg}}{5 \times 10^{-5}\text{ m}^3 \times 60\text{ min} \times \frac{60\text{ s}}{1\text{ min}}} = 3.5 \times 10^{-2} \frac{\text{kg}}{\text{m}^3\text{ s}}$$

$$E_{rxn} = E_{in, Zone\ II} - Q_{loss, Zone\ II} = 0.2861\text{ kWh} - 0.0037 \frac{\text{kWh}}{\text{min}} \times 60\text{ min} = 0.1061\text{ kWh}$$

$$\Delta H_{rxn} = \frac{E_{rxn}}{m_{HO\ i} - m_{HO\ t}} = \frac{0.1061\ kWh \times \frac{3600\ kJ}{1\ kWh}}{0.0063\ kg} = 6.1 \times 10^4 \frac{kJ}{kg}$$

It should be noted that the difference in the value for  $\Delta H_{rxn}$  suggests different products formed in each run.

**Table s4.4:** Reaction rate constants ( $k$ ) and heat of reaction ( $\Delta H_{rxn}$ ) per reaction (R4.2) for control samples in presence of different additives at different operating conditions.

	400°C; 0 rpm		400°C; 500 rpm			420°C; 500 rpm
$k_{ctr} (\frac{Kg}{m^3 s}) \times 10^2$	1.3		1.6			6.4
$\Delta H_{rxn.ctr} (kJ/Kg) \times 10^{-5}$	1.4		1.1			0.24
	<i>Commercial NPs</i>	<i>In situ NPs</i>	10 wt% DC	20 wt% DC	30 wt% DC	10 wt% DC
$k (\frac{Kg}{m^3 s}) \times 10^2$	3.5	7.7	1.5	2	4.7	5.8
$\Delta H_{rxn} (kJ/Kg) \times 10^{-5}$	0.6	0.2	1	0.5	0.2	0.16

## Chapter Five: Conclusions and recommendations

In this chapter the main conclusions made from this work are summarized. In addition, some recommendations for future work and original contributions to knowledge are presented.

### 5.1 Conclusions

This work reports on thermal and catalytic thermal cracking of heavy oil in a closed reactor arrangement. Athabasca vacuum residue and Athabasca bitumen were used as examples of heavy oil. The effect of temperature, reaction time, mixing, asphaltenes content of the feedstock and presence of alumina nanoparticles (NP) and drill cuttings (DC) were investigated. Major results revealed the following:

1. Presence of the asphaltenes in the feedstock increased the reactivity of the coke precursors which led to form higher amount of TI. Asphaltenes convert to TI at higher residence time, mixing and higher pressure. Consequently, the effect of given variable depended on asphaltenes content of the feedstock. Yet, removing asphaltenes from the feedstock shifts the reactions to produce more overall asphaltenes.
2. Presence of asphaltenes in the feed stock did not contribute to more endothermicity and no major changes in the total energy consumption could be detected.
3. Free radical polymerization reactions of the cracking products are limited by mass transfer. Mixing and providing higher catalytic surface area toward cracking reactions by introducing NP or high content of DC, resulted in an increase in TI yield.
4. Spherical *in situ* Al<sub>2</sub>O<sub>3</sub> NPs were obtained with a mean particle diameter of 90±80 nm. *in situ* prepared Al<sub>2</sub>O<sub>3</sub> were engulfed into the TI fraction by virtue of their very small particle size. In contrast, DC dispersed coke precursors, which led to an overall more porous TI structure. On the

other hand, Elemental analysis showed that there is no significant difference between the H/C ratio of the TI produced in presence and absence of DC.

5. The effect of NP and DC contributed to produce more TI at the expense of asphaltenes, while improving the viscosity of the maltene product. This trend is more pronounced for in situ prepared NP and higher concentration of DC.

6. There is an optimum DC content in the feedstock which led to minimum TI yield by suppressing the coalescence of coke precursors to produce coke.

7. The presence of NP did not introduce significant changes in total energy input to the reactor, while the presence of DC contributed to reduction in energy consumption by 11 and 6 % at 400°C and 420°C. It appears that DC have provided a different path for the reactions with lesser activation energy requirement. which suggests a catalytic role and selectivity of a different reaction path in light of the product yield and quality

8. Thermogravimetry analysis of the TI and product asphaltenes shows more reactive produced TI at higher thermal cracking temperature. In addition, the presence of DC in TI, provides higher surface area and decreases mass transfer barriers during oxidation of TI materials which results in narrower heat flow profile. Mass transfer limitations have impact on that oxidation reactions, even within the STA environment, so that by increasing the initial mass of the introduced sample, the heat flow profile shifts toward higher temperature.

## **5.2 Original contributions to knowledge**

This work contributed the following items to our current state of knowledge of thermal cracking of heavy crudes.

1. The endothermicity of the thermal cracking reactions is independent of the amount of asphaltenes in the feedstock.

2. Deasphalting the feedstock prior to thermal cracking leads on an overall increase in the asphaltic product.

3. The catalytic role of in situ prepared and commercial alumina nanoparticles (NP) as well as drill cuttings (DC) during thermal cracking of Athabasca vacuum residue has been identified.

### **5.3 Recommendations for future works**

1. Investigating the nature of the produced TI and asphaltenes at different thermal cracking operating conditions in order to have more insight on thermal cracking mechanism. Thermogravimetry and elemental analysis could be used to achieve this goal.

2. Investigating the effect of DC size on the yield and properties of products toward thermal cracking of heavy oil. Also, study the produced TI in presence of different particle size DC using thermogravimetry analysis to confirm the role of mass transfer during oxidation of TI and the interaction of DC with the coke precursors.

3. Using DC as catalyst in hydrocracking of heavy oil to investigate their effects on product yield and properties under hydrogen atmosphere.

3. Enhancing the surface of DC activity by thermal treatment or chemical modification. Some nanoparticles could be formulated on the surface of DC in order to promote their performance and prevent them from agglomeration.

5. Conducting a reaction mechanism model for thermal cracking based on the nature of produced TI and asphaltenes coupled with product yields at different reaction conditions.

## References

- Abu Tarboush, B.J. & Husein, M.M., 2012a. Adsorption of asphaltenes from heavy oil onto in situ prepared NiO nanoparticles. *Journal of Colloid and Interface Science*, 378(1), pp.64–69.
- Abu Tarboush, B.J. & Husein, M.M., 2015. Dispersed Fe<sub>2</sub>O<sub>3</sub> nanoparticles preparation in heavy oil and their uptake of asphaltenes. *Fuel Processing Technology*, 133, pp.120–127.
- Abu Tarboush, B.J. & Husein, M.M., 2012b. Oxidation of asphaltenes adsorbed onto NiO nanoparticles. *Applied Catalysis A: General*, 445, pp.166–171.
- Agroskin, A.A. et al., 1978. Thermochemical characteristics of petroleum residuum coking. *Chemistry and Technology of Fuels and Oils*, 14(6), pp.412–415.
- Aimin Li, S.C., Li, A. & Yoshikawa, K., 2015. High Quality Oil Recovery from Oil Sludge Employing a Pyrolysis Process with Oil Sludge Ash Catalyst. *International Journal of Waste Resources*, 5(2).
- Al-Marshed, A. et al., 2015. Effectiveness of Different Transition Metal Dispersed Catalysts for In Situ Heavy Oil Upgrading. *Industrial and Engineering Chemistry Research*, 54(43), pp.10645–10655.
- Al-Soufi, H.H. et al., 1988. Thermal conversion (visbreaking) of heavy Iraqi residue. *Fuel*, 67(12), pp.1714–1715.
- AlHumaidan, F., Lababidi, H.M.S. & Al-Rabiah, H., 2013. Thermal cracking kinetics of Kuwaiti vacuum residues in Eureka process. *Fuel*, 103, pp.923–931.
- Alkhaldi, S.J. & Jarallah, S., 2013. *Nanoparticle-mediated Heavy Oil Hydro and Thermal Cracking*. University of Calgary.
- Alvarez, E. et al., 2011. Pyrolysis kinetics of atmospheric residue and its SARA fractions. *Fuel*,

- 90(12), pp.3602–3607.
- Ancheyta, J. et al., 2005. Asphaltene characterization as function of time on-stream during hydroprocessing of Maya crude. *Catalysis Today*, 109(1), pp.162–166.
- Angeles, M.J. et al., 2014. A review of experimental procedures for heavy oil hydrocracking with dispersed catalyst. *Catalysis Today*, 220, pp.274–294.
- Aqsha, A. et al., 2011. Study of sawdust pyrolysis and its devolatilisation kinetics. *Canadian Journal of Chemical Engineering*, 89(6), pp.1451–1457.
- Asgharzadeh Shishavan, R., Ghashghaee, M. & Karimzadeh, R., 2011. Investigation of kinetics and cracked oil structural changes in thermal cracking of Iranian vacuum residues. *Fuel Processing Technology*, 92(12), pp.2226–2234.
- Avid, B. et al., 2004. Characterization of asphaltenes from Brazilian vacuum residue using heptane-Toluene mixtures. , 18(6), pp.1792–1797.
- Banerjee, D.K., 2012. *Oil Sands, Heavy Oil & Bitumen : From Recovery to Refinery*, PennWell Corp.
- Bello, O.O. et al., 2006. Effects of operating conditions on compositional characteristics and reaction kinetics of liquid derived by delayed coking of nigerian petroleum residue. *Brazilian Journal of Chemical Engineering*, 23(3), pp.331–339.
- Bellussi, G. et al., 2013. Hydroconversion of heavy residues in slurry reactors: Developments and perspectives. *Journal of Catalysis*, 308, pp.189–200.
- Bi, W., McCaffrey, W.C. & Gray, M.R., 2007. Agglomeration and Deposition of Coke during Cracking of Petroleum Vacuum Residue. *Energy & Fuels*, 21(3), pp.1205–1211.
- Bian, J. et al., 2008. Chabazite-Clay Composite for Bitumen Upgrading. *Chinese Journal of Catalysis*, 29(11), pp.1084–1088.

- Del Bianco, A., Panariti, N., Anelli, M., et al., 1993. Thermal cracking of petroleum residues. *Fuel*, 72(1), pp.75–80.
- Del Bianco, A., Panariti, N., Prandini, B., et al., 1993. Thermal cracking of petroleum residues. 2. Hydrogen-donor solvent addition. *Fuel*, 72(1), pp.81–85.
- Del Bianco, A. et al., 1993. Thermocatalytic hydroconversion of heavy petroleum cuts with dispersed catalyst. *Applied Catalysis A, General*, 94(1), pp.1–16.
- Carbognani, L., Gonzalez, M.F. & Pereira-Almao, P., 2007. Characterization of Athabasca Vacuum Residue and Its Visbroken Products. Stability and Fast Hydrocarbon Group-Type Distributions. *Energy & Fuels*, 21(3), pp.1631–1639.
- Di Carlo, S. & Janis, B., 1992. Composition and visbreakability of petroleum residues. *Chemical Engineering Science*, 47(9–11), pp.2695–2700.
- Castañeda, L.C., Muñoz, J.A.D. & Ancheyta, J., 2012. Combined process schemes for upgrading of heavy petroleum. *Fuel*, 100, pp.110–127.
- Castañeda, L.C., Muñoz, J.A.D. & Ancheyta, J., 2014. Current situation of emerging technologies for upgrading of heavy oils. *Catalysis Today*, 220, pp.248–273.
- Cheng, S. et al., 2017. Effect of steam and oil sludge ash additive on the products of oil sludge pyrolysis. *Applied Energy*, 185, pp.146–157.
- Cheng, S. et al., 2016. Pyrolysis of oil sludge with oil sludge ash additive employing a stirred tank reactor. *Journal of Analytical and Applied Pyrolysis*, 120, pp.511–520.
- Cheraghian, G. & Hendraningrat, L., 2015. A review on applications of nanotechnology in the enhanced oil recovery part B: effects of nanoparticles on flooding. *International Nano Letters*, 6(1), pp.1–10.
- Corma, A. & Orchillés, A. V., 2000. Current views on the mechanism of catalytic cracking.

- Microporous and Mesoporous Materials*, 35–36, pp.21–30.
- Al Darouich, T., Behar, F. & Largeau, C., 2006. Pressure effect on the thermal cracking of the light aromatic fraction of Safaniya crude oil – Implications for deep prospects. *Organic Geochemistry*, 37(9), pp.1155–1169.
- Dixon, J.C., 2007. Appendix B: Properties of Air. In *The Shock Absorber Handbook*. John Wiley & Sons, Ltd, pp. 375–378.
- Drici, O. & Vossoughi, S., 2013. Study of the Surface Area Effect on Crude Oil Combustion by Thermal Analysis Techniques. *Journal of Petroleum Technology*, 37(4), pp.731–735.
- Ebrahimi, S., Moghaddas, J.S. & Aghjeh, M.K.R., 2008. Study on thermal cracking behavior of petroleum residue. *Fuel*, 87(8–9), pp.1623–1627.
- El-Shereafy, E. et al., 1998. Mechanism of thermal decomposition and  $\gamma$ -pyrolysis of aluminum nitrate nonahydrate [Al(NO<sub>3</sub>)<sub>3</sub>·9H<sub>2</sub>O]. *Journal of Radioanalytical and Nuclear Chemistry*, 237(1–2), pp.183–186.
- Eshraghian, A. & Husein, M.M., 2017. Thermal cracking of Athabasca VR and bitumen and their maltene fraction in a closed reactor system. *Fuel*, 190, pp.396–408.
- Gao, H. et al., 2012. A conceptual catalytic cracking process to treat vacuum residue and vacuum gas oil in different reactors. *Energy and Fuels*, 26(3), pp.1870–1879.
- Gentzis, T. et al., 2001. Effect of carbon additives on the mesophase induction period of Athabasca bitumen. *Fuel processing technology*, 69(3), pp.191–203.
- Gonçalves, M.L.A. et al., 2001. Contribution of Thermal Analysis For Characterization of Asphaltenes From Brazilian Crude Oil. *Journal of Thermal Analysis and Calorimetry*, 64(2), pp.697–706.
- Gonçalves, M.L.A. et al., 2007. Influence of asphaltenes on coke formation during the thermal

- cracking of different Brazilian distillation residues. *Fuel*, 86(4), pp.619–623.
- Gong, J., Long, J. & Xu, Y., 2008. Protolytic cracking in Daqing VGO catalytic cracking process. *Journal of Fuel Chemistry and Technology*, 36(6), pp.691–695.
- Gray, M.R. et al., 2004. Kinetics of Cracking and Devolatilization during Coking of Athabasca Residues. *Industrial & Engineering Chemistry Research*, 43(18), pp.5438–5445.
- Gray, M.R., 2015. *Upgrading of Oil Sands Bitumen and Heavy Oil*, The University of Alberta Press.
- Gray, M.R., Le, T. & Wu, X.A., 2008. Role of Pressure in Coking of Thin Films of Bitumen. *The Canadian Journal of Chemical Engineering*, 85(5), pp.773–780.
- Gray, M.R. & McCaffrey, W.C., 2002. Role of Chain Reactions and Olefin Formation in Cracking, Hydroconversion, and Coking of Petroleum and Bitumen Fractions. *Energy & Fuels*, 16(3), pp.756–766.
- Gray, R.M., 1994. *Upgrading Petroleum Residues and Heavy Oils*, CRC Press.
- Gruia, A., 2006. Recent Advances in Hydrocracking. In *Practical Advances in Petroleum Processing*. New York, NY: Springer New York, pp. 219–255.
- Hashemi, R., Nassar, N.N. & Pereira Almaso, P., 2014. Nanoparticle technology for heavy oil in-situ upgrading and recovery enhancement: Opportunities and challenges. *Applied Energy*, 133, pp.374–387.
- Hauser, A. et al., 2014. Study on Thermal Cracking of Kuwaiti Heavy Oil (Vacuum Residue) and Its SARA Fractions by NMR Spectroscopy. *Energy & Fuels*, 28(7), pp.4321–4332.
- Henderson, J.H. & Weber, L., 1965. Physical Upgrading of Heavy Crude Oils by the Application of Heat. *Journal of Canadian Petroleum Technology*, 4(4), pp.206–212.
- Hill, R.J. et al., 1996. The Influence of Pressure on the Thermal Cracking of Oil. *Energy &*

- Fuels*, 10(4), pp.873–882.
- Hongfu, F. et al., 2002. The study on composition changes of heavy oils during steam stimulation processes. *Fuel*, 81(13), pp.1733–1738.
- Hosokawa, M., 2012. *Nanoparticle technology handbook*, Elsevier.
- Husein, M. & Nassar, N., 2008. Nanoparticle Preparation Using the Single Microemulsions Scheme. *Current Nanoscience*, 4(4), pp.370–380.
- Husein, M.M. & Alkhaldi, S.J., 2014. In Situ Preparation of Alumina Nanoparticles in Heavy Oil and Their Thermal Cracking Performance. *Energy & Fuels*, 28(10), pp.6563–6569.
- International Energy Agency, 2016. Key World Energy Statistics 2016. , p.80. Available at: <https://www.iea.org/publications/freepublications/publication/key-world-energy-statistics.html>.
- International Energy Agency, 2014. World Energy Outlook 2014 Factsheet.
- James G. Speight, 1982. *The chemistry and technology of petroleum*, CRC Press, Taylor and Francis.
- Joshi, J.B. et al., 2008. Petroleum residue upgradation via visbreaking: A review. *Industrial and Engineering Chemistry Research*, 47(23), pp.8960–8988.
- Khorasheh, F. & Gray, M.R., 1993. High-pressure thermal cracking of n-hexadecane. *Industrial & Engineering Chemistry Research*, 32(9), pp.1853–1863.
- Kim, S.-H., Kim, K.-D. & Lee, Y.-K., 2017. Effects of dispersed MoS<sub>2</sub> catalysts and reaction conditions on slurry phase hydrocracking of vacuum residue. *Journal of Catalysis*, 347, pp.127–137.
- Kraemer, D. et al., 2009. Solar assisted method for recovery of bitumen from oil sand. *Applied Energy*, 86(9), pp.1437–1441.

- Krishna, R. et al., 1988. Visbreaking studies on Aghajari long residue. *Fuel*, 67(3), pp.379–383.
- Lababidi, H.M.S., Sabti, H.M. & AlHumaidan, F.S., 2014. Changes in asphaltenes during thermal cracking of residual oils. *Fuel*, 117, pp.59–67.
- Leyva, C. et al., 2013. Chemical characterization of asphaltenes from various crude oils. *Fuel Processing Technology*, 106, pp.734–738.
- Liu, C. et al., 1994. Hydrocracking of Gudao residue with dispersed-phase Mo catalyst. *Fuel*, 73(9), pp.1544–1550.
- Liu, D. et al., 2009. Study on a Water-Soluble Catalyst for Slurry-Phase Hydrocracking of an Atmospheric Residue. *Energy & Fuels*, 23(2), pp.958–961.
- Mallinson, R.G. et al., 1992. Detailed chemical kinetics study of the role of pressure in butane pyrolysis. *Industrial & Engineering Chemistry Research*, 31(1), pp.37–45.
- Mani, T. et al., 2010. Pyrolysis of wheat straw in a thermogravimetric analyzer: Effect of particle size and heating rate on devolatilization and estimation of global kinetics. *Chemical Engineering Research and Design*, 88(8), pp.952–958.
- Marriott, T. et al., 2013. Visbreaking Based Integrated Process for Bitumen Upgrading and Hydrogen Production. In *Canadian International Petroleum Conference*. Petroleum Society of Canada.
- Marsh, H., Martínez-Escandell, M. & Rodríguez-Reinoso, F., 1999. Semicokes from pitch pyrolysis: mechanisms and kinetics. *Carbon*, 37(3), pp.363–390.
- Martínez-Escandell, M. et al., 1999. Pyrolysis of petroleum residues: I. Yields and product analyses. *Carbon*, 37(10), pp.1567–1582.
- Meng, X. et al., 2005. Studies on catalytic pyrolysis of heavy oils: Reaction behaviors and mechanistic pathways. *Applied Catalysis A: General*, 294(2), pp.168–176.

- Meng, X., Xu, C. & Gao, J., 2007. Coking behavior and catalyst deactivation for catalytic pyrolysis of heavy oil. *Fuel*, 86(12–13), pp.1720–1726.
- Mirzayi, B. & Shayan, N.N., 2014. Adsorption kinetics and catalytic oxidation of asphaltene on synthesized maghemite nanoparticles. *Journal of Petroleum Science and Engineering*, 121, pp.134–141.
- Mostavi, E., Asadi, S. & Ugochukwu, E., 2015. Feasibility Study of the Potential Use of Drill Cuttings in Concrete. *Procedia Engineering*, 118(2), pp.1015–1023.
- Murugan, P. et al., 2012. Pyrolysis kinetics of Athabasca bitumen using a TGA under the influence of reservoir sand. *Canadian Journal of Chemical Engineering*, 90(2), pp.315–319.
- Nassar, N.N., Hassan, A. & Pereira-Almao, P., 2011a. Application of Nanotechnology for Heavy Oil Upgrading: Catalytic Steam Gasification/Cracking of Asphaltenes. *Energy & Fuels*, 25(4), pp.1566–1570.
- Nassar, N.N., Hassan, A. & Pereira-Almao, P., 2011b. Effect of surface acidity and basicity of aluminas on asphaltene adsorption and oxidation. *Journal of Colloid and Interface Science*, 360(1), pp.233–238.
- Nassar, N.N. & Husein, M.M., 2007. Study and Modeling of Iron Hydroxide Nanoparticle Uptake by AOT (w/o) Microemulsions. *Langmuir*, 23(26), pp.13093–13103.
- Nhieu, P., Liu, Q. & Gray, M.R., 2016. Role of water and fine solids in onset of coke formation during bitumen cracking. *Fuel*, 166, pp.152–156.
- Oballa, M.C. & Shih, S.S., 1994. *Catalytic hydroprocessing of petroleum and distillates : based on the proceedings of the AIChE Spring National Meeting, Houston, Texas, March 28-April 1, 1993*, M. Dekker.
- Oil and Energy Trends, 2006. Bitumen and heavy crudes: the energy security problem solved?

- Oil and Energy Trends*, 31(6), pp.3–6. Available at: <http://doi.wiley.com/10.1111/j.1744-7992.2006.310603.x> [Accessed November 15, 2016].
- Ortiz-Moreno, H. et al., 2012. Heavy oil upgrading at moderate pressure using dispersed catalysts: Effects of temperature, pressure and catalytic precursor. *Fuel*, 100, pp.186–192.
- Le Page, J.-F., Chatila, S.G. & Davidson, M., 1992. Resid and heavy oil processing.
- Pilviol, O. & Vilhunen, J.J., 1998. Optimization of thermal cracking unit with automatic heavy fuel oil stability analyzer. *ACS Division of Fuel Chemistry, Preprints*.
- Quitian, A. & Ancheyta, J., 2016. Partial upgrading of heavy crude oil by slurry-phase hydrocracking with analytical grade and ore catalysts. *Energy & Fuels*, p.acs.energyfuels.6b01648.
- Radial Drilling, 2014. Unconventional resources. Available at: [http://www.radialdrilling.com/?page\\_id=17130](http://www.radialdrilling.com/?page_id=17130) [Accessed January 1, 2014].
- Rahimi, P., Gentzis, T. & Fairbridge, C., 1999. Interaction of Clay Additives with Mesophase Formed during Thermal Treatment of Solid-Free Athabasca Bitumen Fraction. *Energy & Fuels*, 13, pp.817–825. Available at: <http://pubs.acs.org/doi/abs/10.1021/ef980219n>.
- Rahimi, P.M. & Gentzis, T., 2006. The Chemistry of Bitumen and Heavy Oil Processing. In *Practical Advances in Petroleum Processing*. New York, NY: Springer New York, pp. 597–634.
- Rahmani, S. et al., 2003. Liquid-Phase Behavior during the Cracking of Asphaltenes. *Industrial & Engineering Chemistry Research*, 42(2), pp.4101–4108.
- Rahmani, S., McCaffrey, W. & Gray, M.R., 2002. Kinetics of Solvent Interactions with Asphaltenes during Coke Formation. *Energy & Fuels*, 16(1), pp.148–154.
- Rana, M.S., Sámano, V. & Diaz, J.A.I., 2007. A review of recent advances on process

- technologies for upgrading of heavy oils and residua. *Fuel*, 86(9), pp.1216–1231.
- Raseev, S., 2003. *Thermal and Catalytic Processes in petroleum refining*, CRC Press.
- Redmond, R.. & Lones, J., 1952. *Enthalpies and heat capacities of stainless steel (316), zirconium, and lithium at elevated temperatures*,
- Robinson, P.R., 2006. Petroleum Processing Overview. In *Practical Advances in Petroleum Processing*. New York, NY: Springer New York, pp. 1–78.
- Safiri, A., Ivakpour, J. & Khorasheh, F., 2015. Effect of Operating Conditions and Additives on the Product Yield and Sulfur Content in Thermal Cracking of a Vacuum Residue from the Abadan Refinery. *Energy and Fuels*, 29(8), pp.5452–5457.
- Sakatani, N. et al., 2012. Thermal Conductivity of Glass Beads as a Model Material of Regolith. *43rd Lunar and Planetary Science Conference, held March 19-23, 2012 at The Woodlands, Texas. LPI Contribution No. 1659, id.2000*, 43.
- Sanaie, N. et al., 2001. Effect of minerals on coke precursor formation. *Fuel*, 80(8), pp.1111–1119.
- Sawarkar, A.N., Pandit, A.B. & Joshi, J.B., 2007. Studies in Coking of Arabian Mix Vacuum Residue. *Chemical Engineering Research and Design*, 85(4), pp.481–491.
- Schobert, H.H., 1990. *The Chemistry of Hydrocarbon Fuels*,
- Shaw, J.M., Satyro, M.A. & Yarranton, H.W., 2015. The Phase Behaviour and Properties of Heavy Oils. *Practical Advances in Petroleum Production and Processing*, pp.1–54.
- Shen, Z. et al., 2008. Visbreaking of Chinese Oil Sand Bitumen. *Petroleum Science and Technology*, 26(14), pp.1676–1683.
- Shie, J.L. et al., 2004. Pyrolysis of oil sludge with additives of catalytic solid wastes. *Journal of Analytical and Applied Pyrolysis*, 71(2), pp.695–707.

- Shu, W.R. & Venkatesan, V.N., 2013. Kinetics Of Thermal Visbreaking Of A Cold Lake Bitumen. *Journal of Canadian Petroleum Technology*, 23(2).
- Singh, J. et al., 2004. Studies on thermal cracking behavior of residual feedstocks in a batch reactor. *Chemical Engineering Science*, 59(21), pp.4505–4515.
- Siskin, M. et al., 2006. Chemical approach to control morphology of coke produced in delayed coking. *Energy and Fuels*, 20(5), pp.2117–2124.
- Speight, J.G., 2011. *Handbook of industrial hydrocarbon processes*, Gulf Professional.
- Speight, J.G., 2013. *Heavy and Extra-heavy Oil Upgrading Technologies*, Elsevier.
- Speight, J.G., 2004. New approaches to hydroprocessing. *Catalysis Today*, 98(1–2), pp.55–60.
- Speight, J.G., 2014. *The chemistry and technology of petroleum*, CRC Press, Taylor and Francis.
- Speight, J.G., 2012. Visbreaking: A technology of the past and the future. *Scientia Iranica*, 19(3), pp.569–573.
- Speight, J.G. & Özüm, B., 2002. *Petroleum refining processes*, Marcel Dekker.
- Tanabe, K. & Gray, M.R., 1997. Role of Fine Solids in the Coking of Vacuum Residues. *Energy and Fuel*, 11, pp.1040–1043.
- Tian, K.P., Mohamed, A.R. & Bhatia, S., 1998. Catalytic upgrading of petroleum residual oil by hydrotreating catalysts: a comparison between dispersed and supported catalysts. *Fuel*, 77(11), pp.1221–1227.
- Torregrosa-Rodríguez, P. et al., 2000. Pyrolysis of petroleum residues: II. Chemistry of pyrolysis. *Carbon*, 38(4), pp.535–546.
- Totala, N.B. et al., 2013. Natural Convection Characteristics in Vertical Cylinder. *International Journal Of Engineering And Science Issn*, 3(8p), pp.27–31.
- Trauth, D.M. et al., 1986. *Asphaltene and resid pyrolysis. Effect of reaction environment*, Marcel

Dekker.

- Trejo, F. et al., 2005. Effect of hydrotreating conditions on Maya asphaltenes composition and structural parameters. *Catalysis Today*, 109(1), pp.178–184.
- Trejo, F., 2005. Kinetics of asphaltenes conversion during hydrotreating of Maya crude. *Catalysis Today*, 109(1), pp.99–103.
- Trejo, F. & Rana, M.S., 2010. Thermogravimetric determination of coke from asphaltenes, resins and sediments and coking kinetics of heavy crude asphaltenes. *Catalysis Today*, 150(3), pp.272–278.
- U.S. Energy Information Administration, 2016. *International Energy Outlook 2016*, Washington D.C. Available at: [http://www.eia.gov/forecasts/ieo/pdf/0484\(2016\).pdf](http://www.eia.gov/forecasts/ieo/pdf/0484(2016).pdf) [Accessed November 15, 2016].
- Vafi, K., McCaffrey, W.C. & Gray, M.R., 2012a. Minimization of coke in thermal cracking of athabasca vacuum residue in a high-temperature short-residence time continuous flow aerosol reactor. *Energy and Fuels*, 26(10), pp.6292–6299.
- Vafi, K., McCaffrey, W.C. & Gray, M.R., 2012b. Minimization of Coke in Thermal Cracking of Athabasca Vacuum Residue in a High-Temperature Short-Residence Time Continuous Flow Aerosol Reactor. *Energy & Fuels*, 26(10), pp.6292–6299.
- Vaillancourt, K. et al., 2014. A Canadian 2050 energy outlook: Analysis with the multi-regional model TIMES-Canada. *Applied Energy*, 132, pp.56–65.
- Wang, B. & Manos, G., 2007. A novel thermogravimetric method for coke precursor characterisation. *Journal of Catalysis*, 250(1), pp.121–127.
- Wang, J. et al., 2009. Phase separation and colloidal stability change of karamay residue oil during thermal reaction. *Energy and Fuels*, 23(6), pp.3002–3007.

- Wang, L. et al., 2014. Visbreaking Oilsands-Derived Bitumen in the Temperature Range of 340–400 °C. *Energy & Fuels*, 28(8), pp.5014–5022.
- Wang, S. et al., 1998. Toluene-insoluble fraction from thermal cracking of Athabasca gas oil: formation of a liquid-in-oil emulsion that wets hydrophobic dispersed solids. *Fuel*, 77(14), pp.1647–1653.
- Wang, W. et al., 2016a. Different Mechanisms of Coke Precursor Formation in Thermal Conversion and Deep Hydroprocessing of Vacuum Residue. *Energy & Fuels*, 30(10), pp.8171–8176.
- Wang, W. et al., 2016b. Different Mechanisms of Coke Precursor Formation in Thermal Conversion and Deep Hydroprocessing of Vacuum Residue. *Energy and Fuels*, 30(10), pp.8171–8176.
- Wiehe, I.A., 1993. A phase-separation kinetic model for coke formation. *Industrial & Engineering Chemistry Research*, 32(11), pp.2447–2454.
- Yang, M.-G., Nakamura, I. & Fujimoto, K., 1998. Hydro-thermal cracking of heavy oils and its model compound. *Catalysis Today*, 43(3–4), pp.273–280.
- Yao, N. et al., 2001a. Preparation of novel uniform mesoporous alumina catalysts by the sol-gel method. *Catalysis Today*, 68(1–3), pp.97–109.
- Yao, N. et al., 2001b. Preparation of novel uniform mesoporous alumina catalysts by the sol-gel method. *Catalysis Today*, 68(1–3), pp.97–109.
- Yasar, M., Trauth, D.M. & Klein, M.T., 2001. Asphaltene and resid pyrolysis. 2. The effect of reaction environment on pathways and selectivities. *Energy and Fuels*, 15(3), pp.504–509.
- Yue, C. et al., 2004. Incipient coke formation during heating of heavy hydrocarbons. *Fuel*, 83(11–12), pp.1651–1658.

Zachariah, A. et al., 2013. Suppression of Coke Formation during Bitumen Pyrolysis. *Energy & Fuels*, 27(6), pp.3061–3070.

Zeng, W.M., Gao, L. & Guo, J.K., 1998. New sol-gel route using inorganic salt for synthesizing Al<sub>2</sub>O<sub>3</sub> nanopowders. *Nanostructured Materials*, 10(4), pp.543–550.

Zhao, Y., Gray, M.R. & Chung, K.H., 2001. Molar Kinetics and Selectivity in Cracking of Athabasca Asphaltenes. *Energy & Fuels*, 15(3), pp.751–755.

## Appendix

### ELSEVIER LICENSE TERMS AND CONDITIONS

Apr 24, 2017

---

This Agreement between Afroz Eshraghian ("You") and Elsevier ("Elsevier") consists of your license details and the terms and conditions provided by Elsevier and Copyright Clearance Center.

License Number	4095590870903
License date	Apr 24, 2017
Licensed Content Publisher	Elsevier
Licensed Content Publication	Fuel
Licensed Content Title	Thermal cracking of Athabasca VR and bitumen and their maltene fraction in a closed reactor system
Licensed Content Author	Afroz Eshraghian, Maen M. Husein
Licensed Content Date	15 February 2017
Licensed Content Volume	190
Licensed Content Issue	n/a
Licensed Content Pages	13
Start Page	396
End Page	408
Type of Use	reuse in a thesis/dissertation
Portion	full article
Format	both print and electronic
Are you the author of this Elsevier article?	Yes
Will you be translating?	No
Order reference number	
Title of your thesis/dissertation	Thermal and Catalytic Cracking of Athabasca VR and Bitumen
Expected completion date	Apr 2017
Estimated size (number of pages)	98
Elsevier VAT number	GB 494 6272 12
Requestor Location	Afroz Eshraghian #303 6315 ranchview dr NW  Calgary, AB T3G1B5 Canada Attn: Afroz Eshraghian
Total	0.00 CAD
Terms and Conditions	